

Doctoral Dissertation

博士論文

Quantum Thermalization and Quantum Metrology
in Quantum Ising Systems

(量子イジング系における量子熱化と量子計測)

A Dissertation Submitted for the Degree of Doctor of Philosophy

December 2022

令和4年12月博士（理学）申請

Department of Physics, Graduate School of Science,

The University of Tokyo

東京大学大学院理学系研究科物理学専攻

Yoshinaga Atsuki

吉永 敦紀

Abstract

In this Thesis, we study problems in quantum thermalization and quantum metrology in interacting spin systems, using the quantum Ising model as a prototypical spin model. Both the research areas have been rapidly growing due to the experimental progress in observing and engineering non-equilibrium dynamics in highly isolated quantum systems. The phenomenon of thermalization has been ubiquitously demonstrated in unitary quantum dynamics, leading to developments in the theoretical investigation of the underlying mechanism as well as non-trivial exceptions. Quantum metrology offers ways to improve the sensitivity of measurements by exploiting many-body entanglement, which is generated but also disturbed by internal interactions in the probe system. Exploring the systems that avoid thermalization will deepen our understanding of quantum thermalization as well as will give us hints to design new approaches for realizing entanglement-enhanced sensing with interacting spin systems.

First, we show the emergence of non-ergodicity in Ising models in a weak transverse field. While quantum thermalization of the transverse-field Ising models (TFIMs) is a fundamental problem of statistical physics, it remains unsolved in higher than one dimension because of the models' non-integrability. Here, we adopt an effective model describing the dynamics and rigorously demonstrate the emergence of a nontrivial fragmented structure of the Hilbert space that prohibits thermalization. We show that this mechanism, which is called the Hilbert-space fragmentation (HSF), is due to a kinetic constraint arising from the conservation of the domain wall emerging in the TFIM in a prethermal regime.

Second, we propose a novel entanglement-enhanced sensing scheme for magnetic field sensing in a strongly interacting inhomogeneous Ising model in two dimensions. Although interactions between qubits are crucial for creating entanglement in quantum metrology, they can also destroy relevant entanglement due to thermalization. Our strategy here is to tailor coherent dynamics employing the HSF by constructing a quantum state that is useful for sensing a weak transverse magnetic field but is stable against strong Ising interactions. Our method is robust against various perturbations, such as changes in the lattice structure and inhomogeneity of the couplings, and realized without any active control. From analytical calculations, we show that the Heisenberg-limited sensitivity can be achieved by using our state.

Third and finally, we propose another entanglement-enhanced sensing scheme for magnetometry. Existing sensing schemes so far have often required accurate control of the probe system, which can be challenging in practical applications. We here utilize a propagation dynamics of spin flips in an Ising chain with homogeneous interactions for generation and readout of the GHZ-type entangled states. Our scheme does not require long-range interactions, entangling gate operations, or switching on/off the interactions among qubits. It only requires fast thermalization of the probe, two projective measurements on a single qubit, and switching on/off uniform magnetic fields. We also numerically show that the sensitivity of our scheme beats the standard quantum limit even under the effect of realistic decoherence.

Contents

1	Introduction	5
1.1	Introduction	5
1.1.1	Quantum Thermalization	6
1.1.2	Quantum Metrology	7
1.1.3	Quantum Ising model	8
1.2	Organization of the thesis	9
1.3	Preliminaries	10
1.3.1	Thermalization in isolated quantum systems	10
1.3.2	Quantum thermalization and equilibration	10
1.3.3	Eigenstate thermalization hypothesis	12
1.3.4	Integrable systems	12
1.3.5	Hilbert space fragmentation	13
1.3.6	Ramsey measurement	14
1.3.7	The GHZ state in quantum metrology	16
1.3.8	Effect of decoherence	17
1.3.9	Dynamics in quantum Ising models	17
2	Emergence of Hilbert space fragmentation in Ising models with a weak transverse field	19
2.1	Introduction	19
2.2	Model	20
2.3	Hilbert space fragmentation	23
2.3.1	HSF due to appearance of frozen regions	23
2.3.2	Numerical demonstration of the absence of thermalization	23
2.3.3	Remarks	26
2.4	Subspace properties	27
2.4.1	Non-integrable subspace	27
2.4.2	Subspaces with Integrability and quantum many-body scar states	27
2.5	Conclusion and outlook	28
2.A	Appendix: Expression of the projector \hat{Q}_i	29
2.B	Appendix: Time evolution in the Ising model in a weak transverse field	29
2.C	Appendix: Frozen regions and percolation	30
2.D	Appendix: Exponentially many frozen states	32
2.E	Appendix: Atypical states in the subspace without frozen regions	35

3	Quantum Metrology Protected by Hilbert Space Fragmentation	37
3.1	Introduction	37
3.2	Quantum sensing in an interacting system	38
3.2.1	Model and the Ramsey sensing scheme	38
3.2.2	Sensitivity in a conventional sensing scheme in the presence of the interaction	41
3.3	HSF-protected quantum metrology	42
3.3.1	Description of our sensing scheme	42
3.3.2	Stability for finite ω_x/\bar{J}	43
3.4	Discussion	44
3.5	Conclusion	45
3.A	Appendix: Derivation of the Zeno scaling	45
3.B	Appendix: Derivation of the uncertainty Eq. (3.9)	46
3.C	Appendix: Derivation of the error bound Eq. (3.10)	47
4	Entanglement-enhanced sensing with the one-dimensional Ising model using quantum domino dynamics	50
4.1	Introduction	50
4.2	Setting	51
4.2.1	Ramsey measurement scheme with separable states	51
4.2.2	Quantum sensing with the GHZ state	52
4.2.3	Transverse-field Ising chain	54
4.2.4	Quantum domino dynamics	55
4.3	Our quantum sensing scheme with always-on interaction	57
4.3.1	Description of our sensing scheme	57
4.3.2	Analytical evaluation of the sensitivity	59
4.3.3	Comparison with the conventional scheme using entangling gates	60
4.3.4	Numerical results for the case without environmental noise	60
4.4	Quantum Sensing under time-inhomogeneous dephasing	61
4.4.1	Description of the noise model	62
4.4.2	Numerical results for the case with environmental noise	63
4.5	Discussion: Application to a large system	63
4.6	Conclusion and outlook	65
5	Conclusion	67
A	Proof of the theorem in Appendix 3.C	70

List of publications

The present Thesis is based on the following publications.

- *Emergence of Hilbert Space Fragmentation in Ising Models with a Weak Transverse Field*, **Atsuki Yoshinaga**, Hideaki Hakoshima, Takashi Imoto, Yuichiro Matsuzaki, and Ryusuke Hamazaki, Physical Review Letters **129**, 090602 (2022).
- *Quantum Metrology Protected by Hilbert Space Fragmentation*, **Atsuki Yoshinaga**, Yuichiro Matsuzaki, and Ryusuke Hamazaki, arXiv:2211.09567 (2022).
- *Entanglement-enhanced sensing using a chain of qubits with always-on nearest-neighbor interactions*, **Atsuki Yoshinaga**, Mamiko Tatsuta, and Yuichiro Matsuzaki, Physical Review A, **103** 062602 (2021).

The followings are related but beyond the scope of this Thesis.

- *Quantum metrology based on symmetry-protected adiabatic transformation: imperfection, finite time duration, and dephasing*, Takuya Hatomura, **Atsuki Yoshinaga**, Yuichiro Matsuzaki, and Mamiko Tatsuta. New Journal of Physics, **24**, 033005 (2022).
- *Ballistic propagation of a local impact in the one-dimensional XY model*, **Atsuki Yoshinaga**, Journal of Statistical Mechanics: Theory and Experiment, 2021, 013103 (2021).

Chapter 1

Introduction

1.1 Introduction

Last decades have witnessed remarkable progress in experimental techniques for observing and controlling quantum many-body systems. Ultracold atoms and trapped ions provide good platforms for simulating physics in a variety of models [1]. Thermalization is one of the commonly observed phenomena even in isolated quantum systems. Advances in theoretical studies of quantum thermalization have attracted attentions not only from condensed-matter physicists, but also from high-energy physicists and researchers in other fields [2, 3]. There are also significant progress in quantum-based technologies due to continuing efforts in controlling quantum systems including superconducting qubits, nitrogen-vacancy (NV) centers in diamonds, and photonic systems. Quantum metrology is one of the technologies, which were only theoretical proposals a several decades ago but are now beginning to be used in real-world applications [4]. Further developments in the technology to create and manipulate quantum entanglement in many-body systems would provide, for example, quantum magnetic-field sensors with dramatically high sensitivity [5]. These two areas of active studies, namely quantum thermalization and quantum metrology, will be advanced by expanding our knowledge of non-equilibrium dynamics of quantum many-body systems.

In this Thesis, we theoretically study quantum thermalization and quantum metrology using the quantum Ising model, which is one of the paradigmatic models of quantum many-body systems. By focusing on dynamical features which arise specifically for strong Ising couplings in the model, we give analytical results that offer some new insights into the two fields of research. Specifically, we will reveal the emergence of novel physics in the quantum Ising model called the Hilbert space fragmentation (HSF), which serves as a mechanism for the absence of thermalization. The study of such non-equilibrium physics in quantum many-body systems is also relevant for quantum technologies that make use of a large collection of interacting particles. In this regard, in the latter part of this Thesis, we focus on the application of knowledge found in quantum Ising models to the area of quantum metrology. We will propose new schemes for entanglement-enhanced sensing of weak magnetic fields by utilizing the HSF or so-called quantum domino dynamics that emerges in Ising models in a weak transverse field.

In this Chapter, we provide an overview of the two areas of quantum thermalization and quantum metrology to describe the motivation behind our research in each area, followed by a brief introduction of the the quantum Ising model. We then present the organization of the Thesis. In addition, using the remainder of this Chapter, we review important concepts underlying our studies.

1.1.1 Quantum Thermalization

Thermalization in isolated quantum systems has been studied for a century mainly in the context of deriving statistical mechanics from quantum mechanics. It is widely observed that a macroscopic system evolves towards an equilibrium if left alone, regardless of the details of its initial state. In general, the final equilibrium state is described within the framework of statistical mechanics using thermal equilibrium states. The goal of this field is to understand how this final equilibrium states manifest themselves in non-equilibrium quantum many-body systems. Important questions include the followings: which systems do thermalize?; how do the systems thermalize?; more specifically, in what way does thermalization take place under the unitary evolution? One of the most important achievements on the last question is the eigenstate thermalization hypothesis (ETH) [6, 7, 8]. This is a conjecture that all energy eigenstates are locally “thermal” in generic many-body systems in the sense that each of them is locally indistinguishable from the thermal state with the same energy. ETH provides a sufficient condition for thermalization in isolated quantum systems and its validity has been examined and supported numerically in a wide range of systems [8, 9, 10, 11, 12, 13, 14, 15]. While several analytical arguments imply that thermal eigenstates are indeed ubiquitous [16, 17, 18, 19, 20, 21, 22], it is in general not yet clear that for what systems the ETH is validated as there are obvious exceptions, e.g., models with integrability and localization.

Recently, there has been increasing interest in models that fail to thermalize, which is a promising direction in investigating conditions for quantum thermalization. Well-known classes of such models include integrable systems [23, 24], which possess an extensive number of local conserved quantities, and systems with many-body localization (MBL) [25, 26], which possesses localized eigenstates due typically to disorders in the system. Systems with so-called quantum many-body scar (QMBS) states [27, 28] are another class of models. They are actively studied after the recent discovery in the cold-atom experiment [29, 30]. In systems with QMBS states, the ETH is violated despite being non-integrable and translationally invariant, and certain initial states fail to thermalize. The QMBS states appear as exceptional nonthermal eigenstates in the high-energy spectrum of systems that typically thermalize and seemingly satisfy the ETH. Numerous mechanisms have been proposed and advanced our understanding, including those in which algebraic relationships play an important role [31, 32], but unified understanding of QMBS states is rather missing.

The Hilbert space fragmentation (HSF) [33, 34, 35, 36] is another new type of mechanism that prohibits thermalization even in non-integrable systems, without relying on the translation invariance and fine-tuning of the Hamiltonian, in stark contrast to typical models hosting QMBS states. In fractonic systems [37, 38], for example, kinetic constraints impose restrictions on the dynamics, leading to a fragmented structure of the Hilbert space with exponentially many invariant subspaces. Consequently, the equilibration dynamics strongly depends on the choice of the initial state, even among the states having the same conserved quantities, which is an indication that the ETH is violated. For many previous models showing the HSF, relevant kinetic constraints were attributed to the presence of at least two conserved quantities and the locality of the interaction [27, 28, 39]. To gain better understanding as to what mechanism suppresses thermalization, it may be helpful to investigate other models that allow us to study the HSF analytically. In the present Thesis, we will explore a novel example of quantum systems in which the HSF emerges.

1.1.2 Quantum Metrology

Improving the sensitivity of measuring observables in physical systems is of fundamental importance in both science and engineering. Quantum metrology, which investigates the ultimate precision for sensing that can be achieved given a finite resource, such as the number of probe particles, has been shown to be beneficial in many areas including magnetometry [40, 41], atomic spectroscopy [42, 43], and gravitational wave detection [44, 45]. One important goal in this field is to materialize sensors that exploits quantum nature and achieve the sensitivity beyond classical limits. In this Thesis, we focus on quantum metrology in measuring strength of magnetic fields using an ensemble of probe qubits.

A key observation in quantum metrology is that entangled states can give a better sensitivity. Typically, quantum sensing schemes for external fields consist of preparing the probe spins in a specific quantum state, exposing the state to the target field, and performing measurements on the probe system [46]. It has been shown that the estimation error scales maximally in $N^{-1/2}$ when we use separable states as the initial state, where N denotes the number of probe spins. This type of scaling is called the standard quantum limit (SQL). On the other hand, the scaling can be improved to N^{-1} when we use entangled states. This scaling is called the Heisenberg limit (HL), which shows an $N^{-1/2}$ enhancement over the SQL [47]. The Greenberger-Horne-Zeilinger (GHZ) is known to be a promising probe state for achieving the HL [48], and the Heisenberg-limited sensitivity is demonstrated experimentally using such non-classical states [42].

There are various obstacles in realizing highly sensitive quantum sensors on a large scale. The major challenges include precise generation of useful entangled states, accurate measurements and controls on the probe system, and the suppression of noises arising from interactions between the probe and environments or interactions among probe spins. For example, the environmental noise, or the decoherence effect, generally deteriorates the scaling of the sensitivity from the HL to the SQL as N goes to infinity [49, 50], while some improved scalings survive for certain types of the environmental noise [51, 52, 53, 54]. In practice, probe systems consists of finite number of probe spins in experiments and the dominant noise depends on the settings. If a quantum sensing is performed in a time that is much shorter than the timescale of decoherence, the environmental noise can be made negligible. Therefore, the sensitivity in the quantum strategies can beat that in classical strategies in some cases even when the probe system is not isolated from the environments completely.

However, preparation and readout of entangled probe state and suppression of the noises from internal interactions remain as challenges for interacting probe systems, especially when the controllability of internal interactions is limited. Importantly, the probe states that achieve the HL should possess appropriate entanglement [55, 56], which are usually generated employing internal interactions. However, these interactions, if exist during the interrogation step, can cause unwanted dynamics, such as quantum thermalization, and would spoil the sensitivity [57]. In some experimental settings, such as when a dense ensemble of solid state qubits are used as the probe system, dynamical control of interactions or precise tuning of the coupling strengths should be difficult. In this case, one would have to suppress the interactions by, e.g., implementing a large number of pulses [58]. In the latter part of this Thesis, we consider quantum sensing schemes in the presence of always-on internal interactions among probe spins. In particular, we discuss entanglement-enhanced sensing schemes using the probe system with Ising interactions.

1.1.3 Quantum Ising model

In this Thesis, we consider systems of interacting qubits, i.e., interacting spin-1/2 particles, arranged mainly on hypercubic lattices with Ising-type couplings under a homogeneous transverse field. Such systems are described by the quantum Ising model, or the transverse-field Ising model (TFIM), whose Hamiltonian is given by

$$\hat{H}_{\text{TFIM}} = \hat{H}_{\text{int}} + \hat{H}_x, \quad (1.1)$$

$$\hat{H}_{\text{int}} = - \sum_{\langle i,j \rangle} J_{ij} \hat{\sigma}_i^z \hat{\sigma}_j^z, \quad (1.2)$$

$$\hat{H}_x = h_x \sum_i \hat{\sigma}_i^x, \quad (1.3)$$

where $\hat{\sigma}_i^\mu$ ($\mu = x, y, z$) denotes the Pauli spin operators at site i and $\langle i, j \rangle$ indicates that the sites i and j are neighboring. In Eq. (1.2), J_{ij} denotes the Ising coupling strength between spins and in Eq. (1.3), h_x denotes the strength of the transverse field. We will change the notation of the transverse field strength in some chapters according to the physical meaning. Throughout the Thesis, we set $\hbar = 1$. In Chapters 2 and 3, we consider lattice systems in $d \geq 2$, while in Chapter 4 we consider the case in $d = 1$, where d denotes the spatial dimension of the system.

Despite that solving it is challenging in general, the quantum Ising model allows for analytical treatment under certain conditions and is widely used as a textbook example of quantum many-body systems in condensed-matter physics and statistical mechanics. For $d = 1$, the model becomes exactly solvable [59, 60, 61] and serves as good a example of quantum phase transition as it undergoes a phase transition at zero temperature at a certain value of h_x [62]. However, it is highly non-trivial to solve the model in $d \geq 2$. If h_x is set to zero, the model is reduced to the Ising model, and all the energy eigenstates can be obtained as computational basis states with macroscopic degeneracy. Statistical properties of the classical Ising model including a finite-temperature phase transition are also well investigated [63]. On the other hand, quantum tunneling takes place due to the transverse field for a finite h_x , and analytically exact calculations on individual eigenstates or thermal equilibrium states become difficult. Since numerical simulations are often limited to systems with a few dozen sites, it is generally challenging to investigate the dynamics of the quantum Ising model in $d \geq 2$.

The study of the quantum Ising model is motivated not only by theoretical interests, but also from its experimental relevance. To begin with, it is said that this model began to be widely studied after the introduction by de Gennes to consider dynamics in chemical substances [64]. This model is also important for examining magnetism and ferroelectrics [65, 66]. Ising-type interactions are realized for example in cold atoms [67], trapped ions [68] and super-conducting qubits [69], and the quantum Ising model is also used as a fundamental model for experimental devices in adiabatic quantum computations [70, 71, 72, 73]. Advancing our understanding of this model has a potential to impact a wide range of research areas.

The present Thesis focuses on this model (1.1). In particular, we consider the parameter regime of $|h_x| \ll |J_{ij}|$ in studying quantum thermalization and quantum metrology. As will be reviewed in Sec. 1.3 and illustrated through the Thesis, the model shows notable features in this regime, although exactly solving its dynamics remains difficult for finite values of h_x in $d \geq 2$. For quantum thermalization, we reveal the emergence of non-thermalizing behavior in this model. For quantum metrology, we consider using the Ising model as a probe system. In the latter case, the transverse field serves as a target field to be estimated in Chap. 3 while it acts

as an external control field in Chap.4.

1.2 Organization of the thesis

Motivated by the problems in quantum thermalization and quantum metrology, which we overviewed in the previous sections, we investigate the following three issues in this Thesis: relaxation dynamics in the quantum Ising model in higher than one dimension (Chapter 2), protecting metrologically useful states for estimating magnetic fields in the presence of internal interactions (Chapter 3), and preparing and reading-out entangled states for quantum sensing with low controllability on the interacting probe spins (Chapter 4). Interactions among spins generally cause chaotic dynamics that often leads the system to eventual thermalization. Nonetheless, when certain types of interactions become dominant in the quantum system, new physics can emerge. In this Thesis, we particularly focus on exploring and employing dynamical properties of the quantum Ising models under weak transverse fields, where Ising interactions dominate the system.

Chapter 2 is based on Ref. [74]. Here, we investigate equilibration properties of the d -dimensional quantum Ising models (transverse-field Ising model, TFIM) with $d \geq 2$. Specifically, we study the effective model which describes dynamics of the TFIM in a weak transverse field in an intermediate timescale. We demonstrate that the Hilbert-space fragmentation (HSF) occurs in this effective non-integrable model due to a kinetic constraint arising from the domain-wall conservation. The model serves as a novel analytical example of the appearance of the HSF with only one conserved quantity. We will present results that imply the existence of nontrivial initial-state dependence of non-equilibrium dynamics of the TFIM in a weak transverse field.

Chapters 3 and 4 are devoted to discussions on entanglement-enhanced sensing schemes using systems with always-on nearest-neighbor Ising interactions. Chapter 3 is based on Ref. [75]. In this Chapter, we construct a quantum state that is useful for sensing a weak transverse magnetic field but is stable against strong Ising interactions with a spatial inhomogeneity. Here, we utilize our finding on the HSF in Chapter 2 and mainly consider the two-dimensional TFIM that possesses modest non-uniformity in the Ising couplings. From analytical calculations, we show that the Heisenberg-limited sensitivity can be achieved by using our state. The sensing scheme that we illustrate here provides a new approach to entanglement-enhanced sensor with interacting probe systems without requiring dynamical controls during the interrogation step.

Chapter 4 is based on Ref. [76]. Here, we propose another quantum sensing scheme which uses a homogeneous Ising interaction for generation and readout of the GHZ-type entangled states. Unlike in Chapter 3, we consider using a *one-dimensional* Ising model as the probe system to estimate a weak *longitudinal* field. A propagation dynamics called “quantum domino” dynamics, which occurs in the Ising chain under a weak transverse field, plays an important role in our scheme. This enables us to design our sensing scheme, which only requires initialization of the system, projective measurements on a single spin, and control of global magnetic fields. We also consider the effect of an environmental noise in this Chapter and numerically demonstrate that an improved sensitivity beyond the standard quantum limit can be achieved even in the noisy case.

Finally, in Chapter 5, we give a conclusion of this Thesis and future perspectives of our studies. We also have Appendix A, which provides a full proof for the theorem about the timescale on the effective description of the model in Chapter 3.

1.3 Preliminaries

In the remainder of this Chapter, we review important concepts on underlying this Thesis.

1.3.1 Thermalization in isolated quantum systems

In the following two subsections, we briefly review basics of quantum thermalization in isolated quantum systems and introduce the eigenstate thermalization hypothesis (ETH) [11, 77]. Throughout the Thesis, we consider finite-dimensional quantum systems on discrete lattices. We use N to refer to the number of the sites in the system.

In isolated quantum systems, the time-evolving state of an initial pure state at time t is described as

$$|\psi(t)\rangle = \sum_n c_n e^{-iE_n t} |E_n\rangle, \quad (1.4)$$

where $|E_n\rangle$ denotes the eigenstate of the system Hamiltonian \hat{H} with its eigenvalue E_n and c_n denotes the expansion coefficient of the initial state with respect to $|E_n\rangle$, i.e., $|\psi(0)\rangle = \sum_n c_n |E_n\rangle$ with $\sum_n |c_n|^2 = 1$. Typically, we are interested in measuring local observables or their spatial correlations in experiments. Below, we restrict observables of interest to a set of local observables, which either have a strictly finite support on the lattice or are extensive summations of them.

Intuitively, thermalization describes a process in which, after a certain relaxation time, the expectation values of such observables attain those obtained by microcanonical ensemble average, i.e.,

$$O(t) := \langle \psi(t) | \hat{O} | \psi(t) \rangle \rightarrow O_{\text{mc},E} := \text{Tr} [\hat{\rho}_{\text{mc},E} \hat{O}] \quad (1.5)$$

with

$$\hat{\rho}_{\text{mc},E} := \frac{1}{\mathcal{N}_{E,\delta E}} \sum_{E \leq E_n \leq E + \delta E} |E_n\rangle \langle E_n|, \quad (1.6)$$

where $E = \langle \psi(0) | \hat{H} | \psi(0) \rangle$ denotes the energy which defines the microcanonical energy shell $\mathcal{H}_{\text{mc},E}$, the state $\hat{\rho}_{\text{mc},E}$ denotes the microcanonical ensemble in $\mathcal{H}_{\text{mc},E}$, and $\mathcal{N}_{E,\delta E}$ denotes the number of the energy eigenstates in $\mathcal{H}_{\text{mc},E}$. The width of the energy shell δE is taken appropriately so that it may become subextensive, i.e., $\delta E = o(N)$, while keeping the number of states in $\mathcal{H}_{\text{mc},E}$ large, i.e., $\mathcal{N}_{E,\delta E} \gg 1$. In fact, thermalization in isolated quantum systems have been observed in various experiments [78].

1.3.2 Quantum thermalization and equilibration

Generally, quantum thermalization is formulated using combination of the following two conditions.

- (A) The temporal expectation value $O(t)$ coincides with its long-time average for almost all

the time t , i.e.,

$$O(t) \simeq \overline{O(t)} := \lim_{T \rightarrow \infty} \frac{1}{T} \int_0^T dt O(t). \quad (1.7)$$

(B) The long-time average $\overline{O(t)}$ coincides with the microcanonical expectation value for the same energy E when we ignore the subextensive deviations, i.e.,

$$\overline{O(t)} \simeq O_{\text{mc},E}. \quad (1.8)$$

If both conditions are satisfied for arbitrary local observables, a system is said to be quantum thermalized.

The condition (A) of quantum thermalization, namely equilibration, can be assured to be satisfied under some assumptions [79, 80, 81, 82, 83, 84]. For example, when the system Hamiltonian satisfies a non-resonant condition, that is, $E_n - E_m = E_k - E_l$ if and only if $n = k$ and $m = l$ or $n = m$ and $k = l$, one can show that the temporal fluctuation of $O(t)$ is bounded as [79]

$$\overline{\Delta O(t)} := \left[\overline{\left(O(t) - \overline{O(t)} \right)^2} \right]^{1/2} \leq \frac{\|\hat{O}\|^2}{D_{\text{eff}}}, \quad (1.9)$$

where $\|\cdot\|$ denotes the operator norm. Here, the effective dimension D_{eff} is defined as $D_{\text{eff}} := 1/\sum_n |c_n|^4$, which evaluates the effective number of the energy eigenstates involved in the initial state. Therefore, when D_{eff} is large, which is expected since the number of energy levels grows exponentially in N [85], the temporal value $O(t)$ becomes almost always close to $\overline{O(t)}$.

On the other hand, the condition (B), which is a crucial part of quantum thermalization, is in fact not trivial compared to the condition (A). (When the second condition is satisfied for any initial states, quantum systems are called ergodic or thermal.) One can easily see that the long-time average $\overline{O(t)}$ described in Eq. (1.7) can be written as

$$\overline{O(t)} = \sum_n |c_n|^2 \langle E_n | \hat{O} | E_n \rangle \quad (1.10)$$

from Eq. (1.4), assuming no degeneracy in the Hamiltonian of the system. Equation (1.10) shows that $\overline{O(t)}$ always keeps its initial state information through $|c_n|^2$, which seemingly contradicts with the expectation that thermalization is not sensitive to the detail of the initial state.

Before introducing a possible explanation of this contradiction in the next section, we briefly remark on prethermalization phenomena [77]. Even if the equilibration is guaranteed for a system, the time scale that is required to reach the final equilibrium can become longer than the experimentally reachable time in some cases [86, 87]. In such systems, we can observe prethermalization, which indicates the appearance of a quasi-stationary non-equilibrium state before reaching the final equilibrium. In Chapter 2, we will consider and discuss thermalization properties of the effective model that describes dynamics of the quantum Ising systems in the prethermal timescales.

1.3.3 Eigenstate thermalization hypothesis

The idea of eigenstate thermalization is said to be initiated by von Neumann [88, 89], then established by J. M. Deustch [6] and M. Srednicki [7] independently while there are other notable studies [90, 91, 92], and started to gain significant attentions following studies by M. Rigol [93, 8]. Roughly, it states that all the energy eigenstates are already thermal and locally indistinguishable from the thermal ensemble in the corresponding energy expectation value. Here, we introduce the eigenstate thermalization hypothesis (ETH) in the following form: for all the energy eigenstates $|E_n\rangle$,

$$\langle E_n | \hat{O} | E_n \rangle \simeq O_{\text{mc},E} \quad (1.11)$$

holds, when we ignore the subextensive deviations for any local observables \hat{O} , where $E \simeq E_n$. The ETH is believed to hold for generic non-integrable systems, especially if we focus on the energy eigenstates away from the edge of the spectrum. Specifically, the above notion of the ETH is called the strong ETH, while there are weaker version of the ETH, so called the weak ETH. The weak ETH relaxes the condition of “all” to “almost all” and allows vanishingly small fraction of the eigenstates to break Eq. (1.11) [19, 20, 21].

The strong ETH serves as a sufficient condition for thermalization, in particular the condition (B). This can be seen from combining Eqs. (1.10) and (1.11) as follows. We consider initial states that have subextensive energy fluctuations. This is a reasonable assumption since for most of the states prepared in quench experiments have at most $\mathcal{O}(N^{1/2})$ energy fluctuations [11]. Then, the dominant contribution of the summation in Eq. (1.10) is given by eigenstates with energies close to the energy expectation value E , and we have

$$\sum_n |c_n|^2 \langle E_n | \hat{O} | E_n \rangle \simeq \sum_n |c_n|^2 O_{\text{mc},E_n} \quad (1.12)$$

$$\simeq O_{\text{mc},E} \sum_n |c_n|^2 \quad (1.13)$$

$$= O_{\text{mc},E}, \quad (1.14)$$

where we used $\sum_n |c_n|^2 = 1$. This shows that the long-time average $\overline{O(t)}$ is reduced to the microcanonical average for any initial state with sufficiently small energy fluctuation. We note here that the weak ETH does not guarantee thermalization since Eq. (1.14) is invalidated if we choose an initial state that has a large overlap $|c_n|^2$ with exceptional non-thermal energy eigenstates. This explains why, despite the weak ETH being demonstrated under general conditions independent of the integrability, many integrable systems fail to thermalize [94, 93, 24].

1.3.4 Integrable systems

We briefly explain the integrability of quantum systems at this point. For classical systems, the integrability is defined by the existence of many integrals of motion whose number coincides with the number of degrees of freedom. On the other hand, the definition of quantum integrability is somewhat ambiguous. Generally, a quantum system is called integrable when there are an extensive number of local conserved quantities and all energy eigenstates can be specified using those conserved observables [95, 96, 97]. Systems that are solved using the Bethe ansatz or that can be mapped to non-interacting systems are commonly seen as prototypical examples of integrable systems, the latter of which includes the models that will appear in this Thesis.

One important diagnostics of integrability or non-integrability that is widely used is the statistics of the energy-level spacings [11]. For integrable systems, the statistics is expected to be given by the Poisson distribution, while for non-integrable systems, the distribution is expected to follow the results from random matrix theories [98]. In particular, when the system does not have certain types of symmetries, the distribution is given by the so-called Gaussian orthogonal ensemble (GOE) [99].

We note here that the GOE distribution is obtained typically only after resolving apparent symmetries, whereas the Poisson-like distribution often appears when symmetries such as inversion are unresolved [100, 101, 11, 102]. For example, when a model has the particle-number conservation, the energy-level statistics is calculated after specifying the particle number and then considered to be non-integrable if the GOE distribution is observed [103, 104]. This is also the case when the ETH is numerically checked in non-integrable models, i.e., the validity of Eq. (1.11) is usually examined for energy eigenstates after resolving symmetries [11, 105, 106].

1.3.5 Hilbert space fragmentation

The Hilbert space fragmentation (HSF), or Hilbert space shattering, refers to a phenomenon in which the Hilbert space of a non-integrable system is divided into a large number of invariant subspaces [27, 28, 39]. In general, this can be characterized as the appearance of exponentially many Krylov subspaces. A Krylov subspace is defined by

$$\mathcal{H}_{|\phi\rangle} := \text{span}\{|\phi\rangle, \hat{H}|\phi\rangle, \hat{H}^2|\phi\rangle, \dots\}, \quad (1.15)$$

where \hat{H} denotes the system Hamiltonian and $|\phi\rangle$ is called the root state of this subspace. Typically, the dimension of $\mathcal{H}_{|\phi\rangle}$ becomes comparable to that of the entire Hilbert space of \hat{H} when we take $|\phi\rangle$ as a product state. However, in some systems [34, 107, 35, 36, 108, 109, 110, 111, 112, 113, 114, 115, 116], the dimension of exponentially many Krylov subspaces can become small, or even one, for simple root states. In other words, the Hamiltonian matrix of \hat{H} is diagonalized into many blocks by taking appropriate product states as the basis states. Since each block is disconnected, the initial state that is taken from one of the subspaces is confined into each subspace and fails to thermalize.

We note here that a similar structure of the Hilbert space can be also found in integrable systems with mutually commuting conserved quantities. In this case, each subspace, or energy eigenstate, is characterized by the local conserved quantities. On the other hand, most of the models showing the HSF exhibit many subspaces despite having only a few number of apparent local conserved quantities and thus considered to be non-integrable. In these models, each sector that is characterized by the conventional symmetries further fractures into many nontrivial subspaces, which is in stark contrast to generic non-integrable models that possess a few conventional symmetries.

An important example of the HSF is found in the spin models with conservations of the charge and associated dipole moment [35, 36, 113], which can be mapped from fermionic systems with conservations of the particle number and the center of mass [117, 34]. It has been shown that the interplay between the two conservation laws and the locality of the interaction leads to the HSF [36]. More concretely, there appear many configurations of spins which cannot transition to each other via dynamics of the Hamiltonian due to constraints that are induced by the conservations of the charge and the dipole moment. In many of the models showing the HSF, the presence of dynamically frozen regions of spins leads to appearance of dynamically

disconnected subspaces [34, 36, 35, 112, 113].

Another interesting characteristic that is often found in models of the HSF is the appearance of subspaces with different equilibration properties. For example, models with conservations of the charge and dipole moment [35, 36] exhibit subspaces that are non-integrable, integrable, and those that can be mapped to the PXP model, the last of which is a prototypical non-integrable model of the system with QMBS states [30]. Notably, it has been numerically observed that some non-integrable subspaces obey the ETH, albeit that the thermal states here are defined within the restricted Krylov subspaces [34]. Such appearance of non-integrable and integrable subspaces in a single Hamiltonian is also found in some other models [33, 108], and can be regarded as an important characteristic that often emerges in models with the HSF. This suggests that, even if the model is non-integrable, dynamics specific to systems with integrability or QMBS states can be observed, and thermalization does not always occur depending on the initial states.

Although the HSF is a nontrivial phenomenon, it has actually been realized experimentally and seems not limited to very specific settings [118, 119]. Therefore, it is important to explore other examples that can be discussed analytically in order to build a unified understanding of when and how the HSF occurs. In Chapter 2 of the present Thesis, we will identify the existence of a previously unknown origin of this phenomenon, i.e., the emergence of the HSF in strong relation to the conservation of the domain-wall number. Notably, we reveal that this novel HSF emerges in one of the fundamental quantum models, namely the quantum Ising model, by considering the first-order approximation in the weak-field limit of this model.

1.3.6 Ramsey measurement

In the following three sections, we introduce basic concepts on quantum metrology that we use in this Thesis. Here, we review one of the standard sensing scheme, called the Ramsey measurement (or the Ramsey interferometry), which we use in Chapters 3 and 4. Our goal is to estimate the strength of an unknown static magnetic field ω . We will consider using ensemble of spins that are coupled with this target field as a probe system. The Hamiltonian of the coupling to the target field is described by

$$\hat{H}_\omega = \frac{\omega}{2} \sum_{n=1}^N \hat{\sigma}_n^z. \quad (1.16)$$

In this section and in Chapter 4, we consider the case in which the target is a longitudinal field, while in Chapter 3 we will consider the case for a transverse field.

Typically, quantum sensing schemes consist of the following four steps: (i) arrange the initial probe spins in a metrologically useful state; (ii) let them be exposed to the target field; (iii) perform a projective measurement on the system and obtain an measurement outcome; and (iv) estimate the value of ω from the outcomes after repeating these procedures. Figure 1.1 (a) illustrates these steps for estimating an external field using one spin.

In the standard Ramsey measurement using a single spin, the procedures (i)–(iv) are summarized as follows. In step (i), we initialize the probe spin 1 in the state $|\psi\rangle = (|0\rangle_1 + |1\rangle_1)/\sqrt{2}$, where $|0\rangle_1$ ($|1\rangle_1$) denotes the eigenstate of $\hat{\sigma}_{n=1}^z$ with the eigenvalue $+1$ (-1). In step (ii), let $|\psi\rangle$ evolve according to \hat{H}_ω for an interrogation time T_{int} and obtain $|\psi(T_{\text{int}})\rangle = e^{i\omega T_{\text{int}}/2}(|0\rangle_1 + e^{-i\omega T_{\text{int}}} |1\rangle_1)/\sqrt{2}$. In step (iii), we perform a projective measurement $\hat{P} = (1 + \hat{\sigma}^y)/2$ on

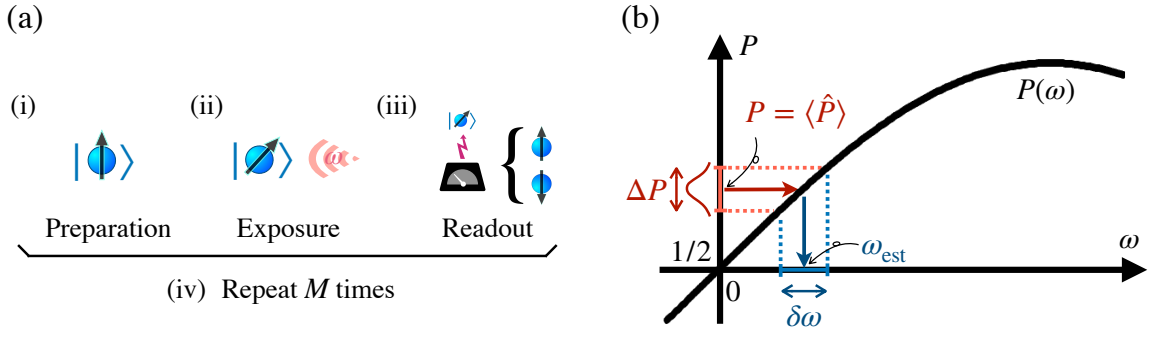


Figure 1.1: (a) Basic steps in a quantum sensing scheme. Repeating the sensing steps (i)–(iii) for M times, we obtain measurement outcomes, which is used to estimate the unknown target field ω . (b) Error propagation in the estimation of ω from outcomes of measurements \hat{P} . Since the expectation value P of \hat{P} is determined by the target field ω , we can estimate ω from P , as illustrated in the figure, when a one-to-one correspondence of ω and P is guaranteed. However, due to the quantum fluctuation in the measurement results, the estimated value of P has the uncertainty that decreases as $\Delta P/\sqrt{M}$, where M denotes the number of outcomes and the square root dependence comes from the central limit theorem. This uncertainty gives rise to the uncertainty of the estimated value ω_{est} , which is obtained by dividing $\Delta P/\sqrt{M}$ by $|\partial P/\partial\omega|$.

$|\psi(T_{\text{int}})\rangle$ and obtain a binary outcome. In step (iv), after M times of the repetition of (i)–(iii), we evaluate the expectation value of the measurements in the form

$$P = (1 + \sin \omega T_{\text{int}})/2, \quad (1.17)$$

from which we estimate ω . In particular, for small ω , the presence of the target field leads to a linear change in the average of outcomes as $\omega \simeq (2P - 1)/T_{\text{int}}$, and thus we can obtain the estimated value of ω from the average of the measurement outcomes.

We note here that the relative phase in Eq. (1.17) has an ambiguity, i.e., ω and $\omega \pm 2\pi m/T_{\text{int}}$ are indistinguishable in the above scheme with m being integers. When there is no information on the range of the target field strength, another phase estimation algorithm is usually employed to resolve this 2π -phase ambiguity in P [120, 121, 122, 123]. In contrast, when we *a priori* have an approximate value of ω , we can estimate ω using the Ramsey scheme. In this Thesis, we consider the latter case. In this case, the relative phase is usually tuned to be close to zero because the slope $|\partial P/\partial\omega|$ is maximized at $\omega T_{\text{int}} = 0$ and hence the presence of a finite but small value of ω with $0 < |\omega| \ll 1$ can be efficiently detected from P [48, 46].

The uncertainty of the estimate of ω is evaluated by considering an error propagation as in [124] as

$$\delta\omega = \frac{\Delta P}{|\frac{\partial P}{\partial\omega}| \sqrt{M}}, \quad (1.18)$$

where $\Delta P = \sqrt{P(1-P)}$ denotes the standard deviation of \hat{P} ; see Fig. 1.1. The square-root dependence on M can be regarded as a consequence of the central limit theorem. For a total available time T_{all} , the number M is calculated as $M = T_{\text{all}}/T_{\text{sensing}}$, where T_{sensing} denotes a combined time of the three procedures (i)–(iii), i.e., $T_{\text{sensing}} := T_{\text{prep}} + T_{\text{int}} + T_{\text{read}}$. Here, T_{prep} denotes the duration time for initializing the probe system and T_{read} denotes the time to perform the projection measurement. For simplicity, in this section, we take $T_{\text{sensing}} = T_{\text{int}}$ by assuming

that T_{int} is much longer than T_{prep} and T_{read} . We will use the expression Eq. (1.18) in Chapters 3 and 4.

If we perform the Ramsey measurement using N uncorrelated spins, the number of the measurement outcomes is enhanced from M to NM . Then, the uncertainty is estimated as $\delta\omega = N^{-1/2}(T_{\text{all}}T_{\text{int}})^{-1/2}$, which shows the scaling $N^{-1/2}$ in the number of probe spins. In fact, it is known that this scaling is the optimal if we use separable states, which is called the standard quantum limit (SQL).

1.3.7 The GHZ state in quantum metrology

Here we briefly review the use of the Greenberger-Horne-Zeilinger (GHZ) state [125] in quantum metrology. The GHZ state is expressed as

$$|\text{GHZ}_x\rangle := \left(\bigotimes_{n=1}^N |+\rangle_n + \bigotimes_{n=1}^N |-\rangle_n \right) / \sqrt{2}, \quad (1.19)$$

where $|\pm\rangle_n$ denotes the eigenstate of $\hat{\sigma}_n^x$ with the eigenvalue ± 1 , respectively, and the subscript x in $|\text{GHZ}_x\rangle$ here indicates that the state is specifically designed as the superposition of the two basis states of $\sum_n \hat{\sigma}_n^x$. This state is one of the prototypical states that have been used to realize entanglement-enhanced sensing in quantum metrology [46]. In this Thesis, we consider using the GHZ-type states in the Ramsey measurement.

The GHZ state can be employed to achieve a better scaling in N over the SQL for magnetometry without noise. Consider preparing the GHZ as our probe state in step (i) in the Ramsey measurement that we introduced in the previous section. In this case, the state after step (ii) is given by

$$|\psi(T_{\text{int}})\rangle := e^{i\omega NT_{\text{int}}/2} \left(\bigotimes_{n=1}^N |+\rangle_n + e^{-i\omega NT_{\text{int}}} \bigotimes_{n=1}^N |-\rangle_n \right) / \sqrt{2}. \quad (1.20)$$

In contrast to the case in which we use separable states, this state (1.20) acquires the phase difference that is enhanced with N . This phase can be read out by performing a projective measurement $\hat{P}' = |\text{GHZ}'_x\rangle\langle\text{GHZ}'_x|$ with

$$|\text{GHZ}'_x\rangle := \left(\bigotimes_{n=1}^N |+\rangle_n + i \bigotimes_{n=1}^N |-\rangle_n \right) / \sqrt{2} \quad (1.21)$$

in step (iii), where the expectation value of the measurements is evaluated as

$$P' = \langle\psi(T_{\text{int}})|\hat{P}'|\psi(T_{\text{int}})\rangle = (1 + \sin N\omega T_{\text{int}})/2. \quad (1.22)$$

Then, the slope $|\partial P'/\partial\omega|$ is enhanced with N in this case, leading to the improved uncertainty of $\delta\omega = N^{-1}(T_{\text{all}}T_{\text{int}})^{-1/2}$, which is $N^{-1/2}$ times better than the case of separable probe states. This scaling N^{-1} of the sensitivity is called the Heisenberg limit, which is the optimal sensitivity in the standard quantum metrology [48].

Here, we note that the projective measurement of \hat{P}' can be replaced with a parity measurement. Specifically, the expression (1.22) can also be obtained by replacing P' with a parity measurement $(1 + \prod_{n=1}^N \hat{\sigma}_n^y)/2$ and applying a single-spin rotation $\exp[i(l_N - 1)\pi\hat{\sigma}_m^y/4]$ on $|\psi(T_{\text{int}})\rangle$

before the measurement, where the integer l_n denotes the remainder obtained by dividing N by 4.

The preparation of the GHZ states has been studied in numerous works. Experimentally, creation of the GHZ states using tens of spins have been demonstrated [126, 127]. The Heisenberg-limited sensitivity using a GHZ state of a few spins is also demonstrated [42]. One simple example of the state preparations is to perform a sequence of entangling gates to a product state [128, 129]. This is usually feasible when the interactions among constituent spins are dynamically controllable. For systems in which the interactions are always present, other techniques can be employed, e.g., adiabatic transformations [130, 131, 132]. In Chapter 4 of the present Thesis, we propose a new approach to create a GHZ-type state using dynamics in the quantum Ising chain without dynamical control of the interactions between spins. We will also show that by utilizing the same dynamics, we can perform the measurement in a simple manner, which usually requires another gate operations or alternative methods.

1.3.8 Effect of decoherence

Entangled states including the GHZ state are generally vulnerable to various types of noises. So far, we have assumed that the probe systems do not experience any decoherence due to the noise from environments. In reality, any probe systems are affected by decoherence, although there has been intensive studies attempting to delay the decoherence both theoretically and experimentally. The GHZ state is fragile against noise such as dephasing, which is the most common type of decoherence in solid-state devices. Unfortunately, it has been found that no improvement of the scaling over the SQL is realized using the GHZ states in the presence of spatially uncorrelated Markovian noise [49, 50]. This suggests that infinitesimal noise is enough to degrade the scaling of the uncertainty from $\mathcal{O}(N^{-1})$ to $\mathcal{O}(N^{-1/2})$ in the asymptotic limit of a large N . (Note that the HL can still be observed for a finite N especially when the decoherence timescale is sufficiently long compared to the time required for sensing procedures.)

However, the situation changes when specific types of noise models are assumed. For example, if the probe spins are subjected to spatially correlated noise, the HL can be recovered in some cases by utilizing the so-called decoherence-free subspaces [53, 133]. Furthermore, when the noise is time-inhomogeneous, it has been found [51, 52, 134] and experimentally demonstrated [135] that the scaling of the uncertainty can be improved up to the Zeno scaling, which gives $\delta\omega = \mathcal{O}(N^{-3/4})$, even if the noise has no spatial correlation. These works suggest that we can still experimentally achieve the sensitivity that is beyond the reach in any classical schemes. In the Thesis, we will mainly focus on the unitary noise due to internal interactions, while Chapter 4 includes discussion of the effect of decoherence under time-inhomogeneous dephasing.

1.3.9 Dynamics in quantum Ising models

In this last section of the preliminaries, we review notable dynamical properties of the quantum Ising models that have been revealed in previous studies.

Dynamics of the quantum Ising models have been investigated typically by resorting to numerical calculations or effective descriptions, except for the case in which analytically exact calculations are available. First, in the case of $d = 1$, the model becomes solvable by mapping to a free fermionic system under the Jordan-Wigner transformation [136]. There are also studies which focus on a weak transverse-field regime of the quantum Ising chain

[137, 138, 139, 140, 141]. It has been found that so-called “quantum domino dynamics” occurs in the strong homogeneous coupling limit [137], where the Hamiltonian at the leading nontrivial contribution for small h_x/J_{ij} (see also Eqs. (1.1)–(1.3)) becomes solvable by using the Kramers-Wannier transformation [142]. Quantum domino dynamics refers to a sequence of spin flips which is induced by a spin flip in a chain of spins that is initially arranged in the same z direction. We will consider utilizing this dynamics to quantum sensing in Chapter 4. Finally, we note that adding a longitudinal field breaks the integrability of the quantum Ising chain. Interestingly, the appearance of the HSF has been found in this case when a large limit of the Ising interaction and the additional longitudinal field are taken [108].

In the case of $d \geq 2$, the quantum Ising models become non-integrable in general and numerical calculations are often used. For $d = 2$, in particular, the ETH is numerically checked [143, 100] especially away from the integrable point, i.e., $h_x = 0$, where finite-size effects become significant. However, it is also reported that the model fails to thermalize for a certain initial conditions from numerical calculations [144]. In addition, a recent study in Ref. [145] pointed out that QMBS states perturbatively appears in the TFIM on a two-dimensional ladder system in a weak field. In Chapter 2 of the present Thesis, we analytically show the absence of thermalization for $d \geq 2$ dimensional quantum Ising model in the prethermal timescale due to the emergent HSF in a weak transverse field.

Chapter 2

Emergence of Hilbert space fragmentation in Ising models with a weak transverse field

In this Chapter, we investigate a novel dynamical feature of the quantum Ising model in $d \geq 2$ spatial dimensions. In particular, we demonstrate for the first time that novel Hilbert space fragmentation (HSF) occurs in the effective non-integrable model for Ising models with a weak transverse field as a consequence of approximate global conservation law of the domain-wall number. Our results indicate the emergence of non-thermal behavior in Ising models with a weak transverse field in a prethermal regime.

This Chapter is organized as follows. After the introduction, we introduce the model of our interest in Sec. 2.2. We then show that our effective model exhibits the HSF in Sec. 2.3 due to the appearance of frozen regions. We also provide some numerical evidence of non-ergodicity, i.e., the breakdown of the strong ETH, in this model and present some remarks in Secs. 2.3.2 and 2.3.3. In Sec. 2.4, we investigate dynamical properties of some of the fragmented subspaces of the model in two dimension, and summarize our findings and outlook in Sec. 2.5. We also have appendices as Secs. 2.A–2.E to add details on our discussion in Secs. 2.2–2.4.

2.1 Introduction

The quantum Ising model, or the transverse-field Ising model (TFIM), serves as a minimal model among quantum many-body systems as we have reviewed in the previous Chapter. Despite its simplicity, the TFIM is quite difficult to investigate in higher-than-one dimensions because of its non-integrable nature. It is particularly important for foundation of quantum statistical mechanics to elucidate dynamical properties of the model, where little is understood due to the rapid growth of their Hilbert-space dimension against the system size. Indeed, its quantum thermalization has recently been investigated in relatively large systems [143, 100, 146, 147, 148]. It was found that the model does not always thermalize in some quenches with numerical experiments [144] and that non-thermal eigenstates appear in a two-dimensional ladder system for the first order perturbation in the weak transverse field[145].

The search for understanding quantum thermalization and the conditions behind it has been expanded substantially with the progress in experimental techniques [94, 23, 86, 149, 78, 150, 151, 152]. One of the most important achievements is the eigenstate thermalization hypoth-

esis (ETH) [6, 7, 8], which conjectures that all energy eigenstates are thermal and provides a sufficient condition for thermalization in isolated quantum systems. While the ETH has been confirmed numerically in various systems [8, 9, 10, 11, 12, 13, 14, 15], there is also growing interest in models violating the ETH. The emergence of non-thermal eigenstates has often been attributed to extensively many local conserved quantities due to, e.g., integrability [93, 153, 96, 154, 24] and localization [155, 25, 156, 157, 26].

The Hilbert space fragmentation (HSF) has recently attracted much attention as yet another mechanism of invalidating the ETH in non-integrable models [107, 34, 35, 36, 108, 109, 110, 27, 111, 112, 113, 114, 115, 116, 28]. In some models such as fractonic systems [37, 38], kinetic constraints impose restrictions on the dynamics [34, 36, 35] and create frozen regions which dynamically divide the systems. This generates a fragmented structure of the Hilbert space with exponentially many nontrivial subspaces. In these cases, initial states cannot access the entire Hilbert space and fail to thermalize. For many previous models showing the HSF, the presence of at least two conserved quantities and the locality of the interaction were the origin of relevant kinetic constraints.

In this Chapter, we show the emergence of non-ergodicity in a prethermal regime for Ising models with a weak transverse field on a hypercubic lattice in dimensions higher than one. In particular, by analytical calculations, we reveal for the first time that the effective model for the TFIM in limit of a weak transverse field exhibits the HSF for $d \geq 2$. Notably, this effective model has only one global conserved quantity namely, the domain-wall (DW) conservation. The locality of the Hamiltonian and the DW conservation law leads to a kinetic constraint in the model (Fig. 2.1 (a)), and to the appearance of frozen regions. Due to the frozen regions, the Hilbert space is separated into exponentially many subspaces (Fig. 2.1 (b)). Consequently, the ETH breaks down and the effective model shows non-thermalizing behavior depending on the initial state. The emergence of frozen regions in our model is distinct from the ones in the previously studied models which require several conserved charges for exhibiting such frozen regions [34, 36, 35, 112]. For $d = 2$, we further demonstrate that rich dynamical properties are found in subspaces inside the DW sectors, including those found in non-integrable, integrable, and quantum many-body scarred systems [30, 27, 39].

2.2 Model

In this Chapter, we consider the TFIM on a d -dimensional hypercubic lattice. The Hamiltonian is described as

$$\hat{H}_{\text{TFIM}} := \hat{H}_{\text{DW}} + h_x \sum_i \hat{\sigma}_i^x, \quad (2.1)$$

with

$$\hat{H}_{\text{DW}} := - \sum_{\langle i,j \rangle} \hat{\sigma}_i^z \hat{\sigma}_j^z, \quad (2.2)$$

where $\hat{\sigma}_i^\mu$ ($\mu = x, y, z$) denotes the Pauli spin operators at site i , $\langle i, j \rangle$ indicates that the sites i and j are neighboring, and h_x denotes the strength of the transverse field. While the DW number, i.e., the eigenvalues n_{DW} of $\hat{n}_{\text{DW}} := \sum_{\langle i,j \rangle} (1 - \hat{\sigma}_i^z \hat{\sigma}_j^z)/2$, is not conserved under the time evolution by \hat{H}_{TFIM} for finite h_x , it is approximately conserved for exponentially long time

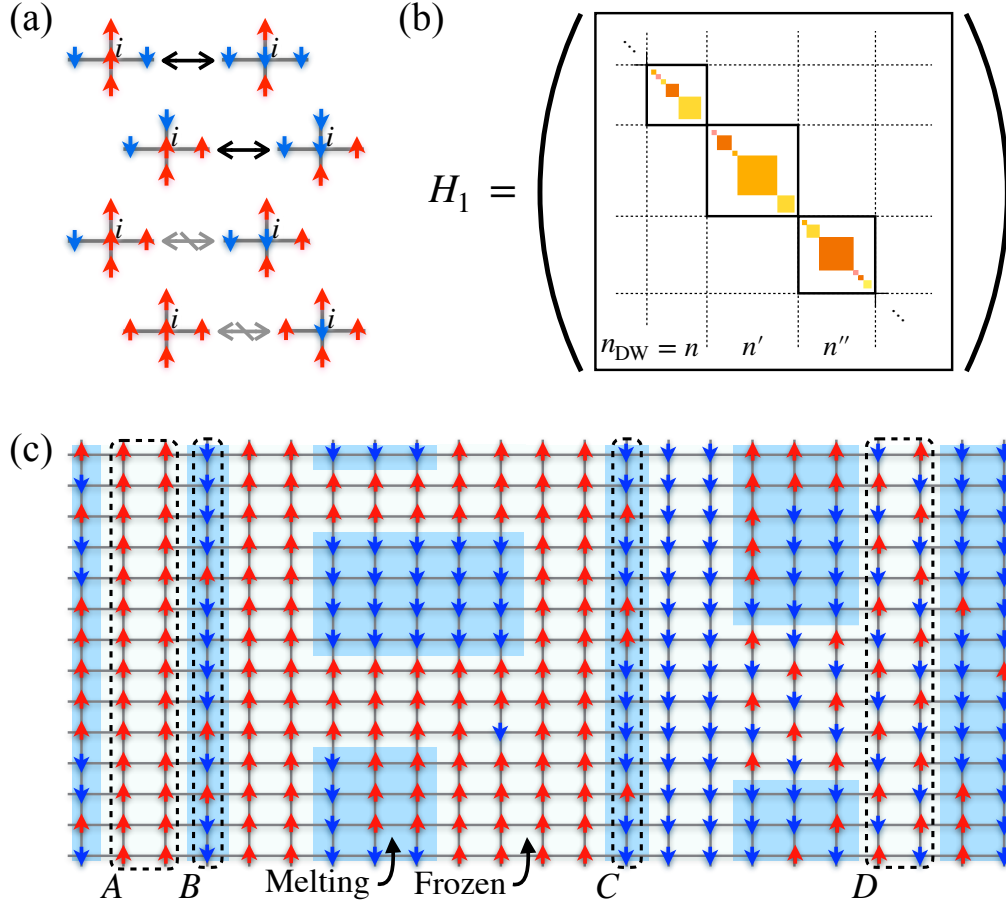


Figure 2.1: (a) Schematic picture of the kinetic constraint arising from the projection operator \hat{Q}_i in the Hamiltonian Eq. (2.4), where we take the dimension d as two. Each spin at site i on a square lattice is flipped only when its two nearest neighbors are up and the other two spins are down. (b) Fragmented structure of the effective Hamiltonian. In addition to the block structure due to the conservation of the domain-wall number n_{DW} , the Hamiltonian matrix for an appropriate basis is further block diagonalized, namely fragmented. (c) An example of frozen regions (non-shaded) and melting regions (blue-shaded), where $d = 2$ and the periodic boundary conditions are assumed. Red and blue arrows on each lattice site represent up and down spins in $\hat{\sigma}_i^z$ basis, respectively. The areas surrounded by dashed lines and labeled A and D exemplify prototypical spin configurations in frozen regions and those labeled B and C indicate one-dimensional melting regions which correspond to the PXP and XX models, respectively. Frozen regions percolate the system, so that every spin in these regions is guaranteed to have at least three nearest-neighboring spins with the same sign. [Reproduced and modified from Fig. 1 in Ref. [74].]

if h_x is sufficiently small [158]. Indeed, from a first-order perturbation theory, we obtain the following effective Hamiltonian [145, 159]:

$$\hat{H}_{\text{eff}} := \hat{H}_{\text{DW}} + h_x \hat{H}_1 \quad (2.3)$$

with

$$\hat{H}_1 := \sum_i \hat{\sigma}_i^x \hat{Q}_i, \quad (2.4)$$

where the operator \hat{Q}_i projects all spin configurations onto the state space in which the sum of the z components of the $2 \times d$ spins surrounding the site i is zero (see Fig. 2.1 (a)). For example, the projector \hat{Q}_i for $d = 2$ is explicitly given by

$$\hat{Q}_i := \frac{5}{8} - \frac{1}{16} \left(\sum_{j \in \text{ngbh}(i)} \hat{\sigma}_j^z \right)^2 + \frac{3}{8} \prod_{j \in \text{ngbh}(i)} \hat{\sigma}_j^z, \quad (2.5)$$

where $\text{ngbh}(i)$ denotes the nearest-neighbor sites of the site i ; see Appendix 2.A for the expression for other spatial dimensions.

The effective Hamiltonian \hat{H}_{eff} approximates the dynamics of local observables governed by the original Hamiltonian (2.1) for a certain time scale that goes to infinity as $h_x \rightarrow 0$ [160, 161]. In Appendix 2.B, we provide numerical estimation of the timescale over which our effective model works well.

In general, the effective Hamiltonian \hat{H}_{eff} can be obtained as the first-order contribution in the degenerate perturbation theory based on the Schrieffer-Wolff transformation (SWT) [162, 163, 158, 164]. In this method, the first-order contribution is formally given by projecting the perturbative term in the Hamiltonian onto the degenerate blocks of the unperturbed Hamiltonian [164]. This is equivalent to taking the time-independent part of the perturbative term in the rotating frame, i.e., the secular part of the perturbative term in the interaction picture; see e.g., Ref. [137] for the derivation of the effective Hamiltonian for the TFIM in $d = 1$. In this Thesis, we only focus on the first-order contribution. The second-order contribution is estimated to be $\mathcal{O}(h_x^2/J)$ in our case, where J denotes the strength of the Ising coupling, which is taken as $J = 1$ in this Chapter. (The error bound for the dynamics in the effective description up to the first order is obtained in Refs. [161, 160], which showed that the deviation from the actual dynamics grows in time at most $\sim \mathcal{O}(h_x^2/J)t$.) We note that the explicit form of the second-order correction to our effective Hamiltonian \hat{H}_{eff} is obtained in Refs. [165, 166].

Since \hat{H}_1 commutes with \hat{H}_{DW} , Hamiltonians \hat{H}_1 and \hat{H}_{eff} lead to the same dynamics when we specify a DW sector. Thus, we focus on the Hamiltonian \hat{H}_1 in the following. The Hamiltonian \hat{H}_1 is non-integrable as we will discuss later; it conserves the DW number and is block diagonalized accordingly. Apart from spatial symmetries, such as inversion, the Hamiltonian also has global chiral symmetry, i.e., \hat{H}_1 anti-commutes with $\prod_i \hat{\sigma}_i^\nu$ ($\nu = y, z$). This symmetry produces non-zero energy eigenvalues in pairs with opposite signs. While the Hamiltonian also has global \mathbb{Z}_2 symmetry (i.e., \hat{H}_1 commutes with $\prod_i \hat{\sigma}_i^x$), we confirm that this symmetry is irrelevant for the emergence of HSF.

2.3 Hilbert space fragmentation

We now demonstrate the Hilbert-space fragmentation of the Hamiltonian \hat{H}_1 in Eq. (2.4). We show that each sector characterized by the number of DWs is further divided into many subspaces (see Fig. 2.1 (b)), leading to the absence of thermalization in this model.

2.3.1 HSF due to appearance of frozen regions

We first show that the kinetic constraint induced by \hat{Q}_i forms regions where the spin dynamics is frozen. More specifically, let us consider a product state $|F\rangle = \prod_{i \in \mathcal{F}} |s_i\rangle$ forming a sub-region \mathcal{F} on the entire lattice Λ , where $|s_i\rangle$ is one of the eigenstates of $\hat{\sigma}_i^z$. If $|F\rangle$ satisfies the following condition, we call \mathcal{F} a frozen region: $\hat{Q}_i(|F\rangle \otimes |M\rangle) = 0$ for $\forall i \in \mathcal{F}$ and any $|M\rangle$ defined on Λ/\mathcal{F} . The frozen regions remain unchanged under the time evolution by \hat{H}_1 (as well as \hat{H}_{eff}). Meanwhile, non-frozen regions, which we call melting regions, are isolated from one another and separated by frozen regions. Nontrivial dynamics occurs only in the melting regions. Below we will focus on the case with $d = 2$ although most observations here hold for $d \geq 3$ too.

Figure 2.1 (c) exemplifies a possible spin configuration and associated frozen and melting regions. One simple example of the frozen region is a ladder-like region along the lattice with all spins aligning up in the z direction, percolating the system from one end to the other (the area A in Fig. 2.1 (c)). Another example is a wider region in which not all the spins are aligned in the same direction (the region between the areas B and C in Fig. 2.1 (c)) and surrounds some melting regions. A spin configuration in a frozen region can also exhibit a checker-board pattern (the area D in Fig. 2.1 (c)). In all of the cases, every spin is arranged in such a way that at least $(d + 1)$ of its nearest-neighbor spins have the same direction, which set the value of \hat{Q}_i to zero. Because this condition prohibits a frozen region from having corners under the periodic boundary conditions, we conjecture that all frozen regions percolate the system from one side to the other; see Appendix 2.C.

Because of the frozen regions, the Hilbert space has exponentially many subspaces. For example, a spin configuration having a frozen region cannot change into another spin configuration having a different frozen region by the Hamiltonian dynamics. This splits the Hilbert space into subspaces. Moreover, even when the arrangement of frozen regions is the same, there are many ways in which the DWs are spatially distributed over separated melting regions. Since the density of DW within each melting region is conserved over time, the Hilbert space is broken up into even smaller subspaces. Each subspace is therefore characterized by the configuration of the frozen regions and the spatial distribution of the DW density for melting regions.

2.3.2 Numerical demonstration of the absence of thermalization

The emergence of the dynamically fragmented subspaces suggests that the relaxation dynamics of the system strongly depends on the details of the initial state. When we take an initial state from one of the subspaces in a given DW sector and let it evolve, the state remains in this subspace. Let us consider, for example, two initial product states $|\psi_1\rangle$ and $|\psi_2\rangle$ shown in Fig. 2.2 (a), which are slightly different in their spin configurations but have the same energy in a DW sector. Figure 2.2 (b) shows the dynamics of the expectation value of the magnetization density from these two initial product states according to the effective Hamiltonian \hat{H}_{eff} . Throughout this Chapter, we perform numerical calculations under the condition that the spins constituting the system are surrounded by fixed frozen spins pointing down. Due to the frozen region in the

middle of the lattice, which emerges only in the state $|\psi_2\rangle$, the magnetization relaxes to substantially different values for the two initial conditions, which indicates ergodicity breaking. This example highlights that a frozen region covering a large area of the system can be converted into a melting region with a small change in the initial configuration in this model. Similar behavior can be also observed under the time evolution by \hat{H}_{TFIM} with a weak transverse field h_x ; see Appendix 2.B.

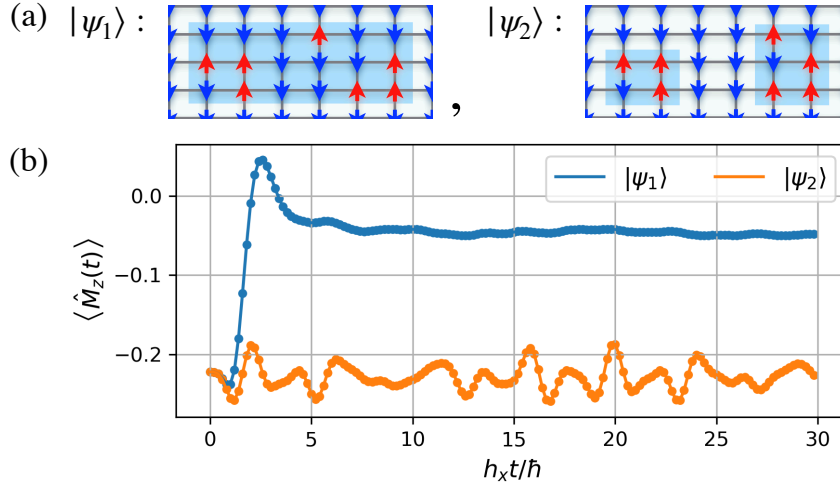


Figure 2.2: (a) Spin configurations of the two initial states for a $N = 3 \times 6$ lattice. We assume that the system is surrounded by fixed spins pointing down. Regions with blue shades show melting ones. (b) Magnetization dynamics starting from the two initial product states. Time evolution of the expectation value $\langle \hat{M}_z(t) \rangle := \langle \psi(t) | (1/N) \sum_i \hat{\sigma}_i^z | \psi(t) \rangle$ shows that a slightly different initial condition results in substantially different stationary states. [Reproduced from Fig. 2 in Ref. [74].]

The non-ergodicity due to the HSF in this model is deeply related to the violation of the ETH. The fragmented structure yields exponentially many non-thermal energy eigenstates. A simple example of such non-thermal states is a variety of product states with all spins being frozen, which constitute fragmented subspaces with the dimension one. We hereafter refer to the states with all frozen spins as frozen states. As detailed in Appendix 2.D, we show that the number of frozen states increases exponentially in the system size, indicating the emergence of the HSF. We note that Ref. [145] also finds a similar frozen state for an effective model of TFIM on a pseudo-one-dimensional ladder, but no HSF was discussed there. As another example, we find eigenstates which have spatially inhomogeneous DW density owing to frozen regions that act as a wall to separate different melting regions.

Figure 2.3 (a) shows the entanglement entropy of all the energy eigenstates of \hat{H}_1 in a fixed DW sector for a $N = 3 \times 6$ lattice. (When numerically diagonalizing the Hamiltonian for Figs. 2.3 (a) and (c), we added perturbative random longitudinal fields with average strength 10^{-5} . This is due to avoid ambiguity caused by exact degeneracy originating from unwanted symmetries such as inversion.) We evaluate it by computing the von-Neumann entropy of the left half of the system. In generic systems obeying the ETH, eigenstate entanglement entropies are close to one another for close eigenenergies. In Fig. 2.3 (a), we demonstrate the violation of the ETH in this model, that is, a broad distribution of the entanglement entropy even for close eigenenergies and the presence of eigenstates with low entanglement. Due to the existence of frozen regions that divide the system into isolated parts, there are many eigenstates with zero bipartite entanglement.

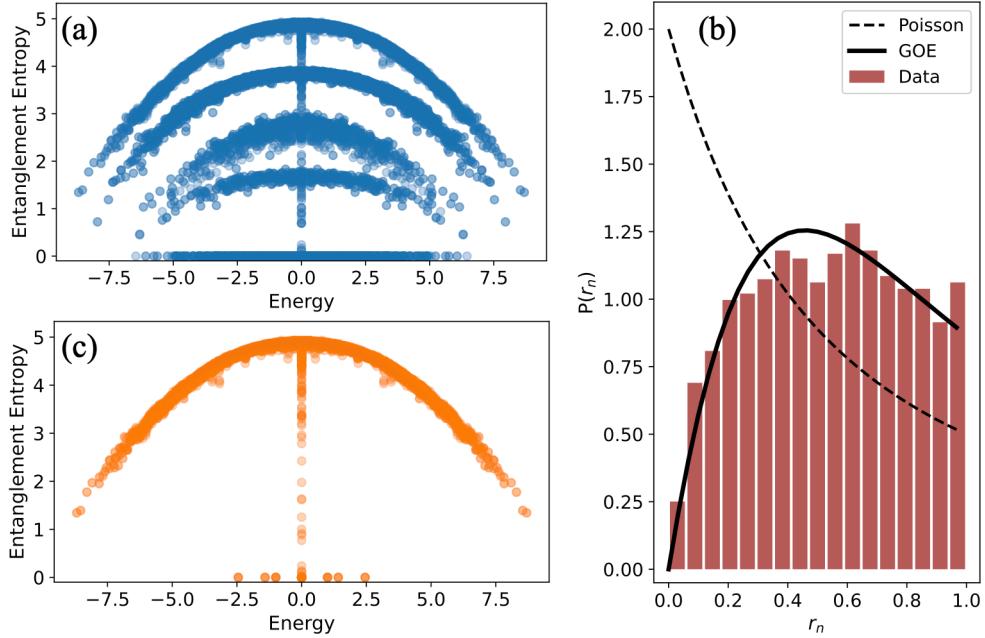


Figure 2.3: (a) Entanglement entropy of all the energy eigenstates in a DW sector for a $N = 3 \times 6$ lattice. At its boundaries, the system is surrounded by fixed frozen spins pointing down. In all panels (a)–(c), we take $n_{\text{DW}} = 20$ out of the possible range of $0 \leq n_{\text{DW}} \leq 36$. We find that the entanglement entropy exhibits a broad distribution even for a fixed energy, indicating the breakdown of the ETH in this DW sector. (b) Distribution of the consecutive energy-gap ratio r_n [99] for the subspace without frozen regions. The statistics is calculated after resolving the two spatial inversion symmetries along the x and y directions; see Sec. 1.3.4. Dashed line shows the Poisson prediction and the solid line shows the GOE prediction. (c) Entanglement entropy of the energy eigenstates in the subspace without frozen regions (extracted from the panel (a)). [Reproduced from Fig. 3 in Ref. [74].]

2.3.3 Remarks

We comment here on some features and implications of the findings in this section. First, let us emphasize again that the kinetic constraint in \hat{H}_1 is associated with the conservation of the DW number \hat{n}_{DW} alone. We have shown that frozen regions appear due to this constraint, leading to the appearance of exponentially many frozen states in our model. The appearance of many frozen states is often found in the previously studied models [28] as a consequence of more than one conserved quantities [34, 36, 35, 115, 109, 112]. Our finding here demonstrates that such nontrivial physics can occur even when there is only one apparent conserved quantity.

Second, consequences of the percolation behavior of frozen regions depend on the dimensionality d . For $d = 2$, the system is always divided into isolated parts by frozen regions that percolate the system and act as walls. In contrast, for $d > 2$, frozen regions do not always divide the system because their shape can be, e.g., a square prism which percolates only in one direction along the lattice. It is also worth mentioning that the Hamiltonian (2.4) for $d = 1$ does not yield many frozen regions and the resulting HSF, while we show that it does for $d > 1$.

Finally, let us comment on implications of the possible appearance of frozen regions in our model \hat{H}_1 for the validity of the ETH in DW sectors. First, we emphasize here that the eigenstates with frozen regions can be found in every DW sector of \hat{H}_1 as long as the system is sufficiently large. This implies that the non-ergodic behavior due to frozen spins can be found for specific initial states with *any* finite energy density with respect to the effective Hamiltonian $\hat{H}_{\text{eff}} = \hat{H}_{\text{DW}} + h_x \hat{H}_1$ as well as to the original TFIM in a weak transverse field. Nevertheless, we note as follows that the possible appearance of frozen regions, although it indeed results in the breakdown of the strong-ETH, does not always imply the breakdown of the weak-ETH (see also Sec. 1.3.3). In fact, most of the eigenstates do not possess frozen regions and may be thermal.

Importantly, states without frozen regions typically belong to a single connected subspace that dominates the DW sector in the thermodynamic limit. In fact, we numerically observed that there appears a single dominant subspace consisting of states without frozen regions among the fragmented subspaces in a typical DW sector of \hat{H}_1 . On the other hand, the other, still exponentially many, subspaces occupy only a vanishingly small fraction of this sector. The latter subspaces consist of states having frozen regions including frozen states. This has been pointed out and examined in Ref. [165]. Specifically, it is numerically shown that every DW sector, except for sectors with sufficiently low, or high, DW densities, possesses a single subspace that dominates the sector in the thermodynamic limit. A sector with this property is also called “weakly fragmented”, while a sector in which the size of the largest subspace in the sector is vanishingly small is called “strongly fragmented” [35, 167, 36]. Reference [165] showed that our model \hat{H}_1 is typically weakly fragmented except for a vanishingly small parameter range of the DW density at which the system becomes strongly fragmented.

One can then question whether the dominant subspace is thermal or not. Notably, as we will show in the next section, the most of the eigenstates in the dominant subspace in a typical DW sector seems thermal. That is, the level statistics and the distribution of the eigenstate entanglement entropy for the eigenstates are consistent with those found in thermal eigenstates of ergodic systems. This implies the validity of the weak ETH in the dominant subspace as well as in the sector to which it belongs. Nevertheless, we will also demonstrate in the following the emergence of atypical eigenstates in a dominant subspace that are melting but non-thermal. This suggests that the ergodicity breaking in the system \hat{H}_1 does not always rely on the appearance of frozen spins.

2.4 Subspace properties

Now we investigate properties of the fragmented subspaces of \hat{H}_1 . The dynamics for each subspace is observed only in the melting regions, being characterized by their shapes and their boundary conditions. Here we specifically consider the case for $d = 2$ and show that there is a rich variety of dynamics in melting regions, including those found in non-integrable, integrable, and quantum many-body scarred systems.

2.4.1 Non-integrable subspace

The Hamiltonian \hat{H}_1 itself is presumably non-integrable. To demonstrate this, let us choose a subspace without any frozen regions in a DW sector. (We numerically find that, such a subspace, if exists, becomes the only subspace occupying the largest Hilbert-space dimension in the DW sector.) In Fig. 2.3 (b), we perform the analysis of energy-level statistics for this subspace. Specifically, we calculate the distribution of the consecutive energy-gap ratio $r_n = \min(\delta_n/\delta_{n-1}, \delta_{n-1}/\delta_n)$ with $\delta_n := E_{n+1} - E_n$, where E_n denotes the n th energy eigenvalue in the subspace [99]. The statistics of this ratio in Fig. 2.3 (b) shows a good agreement with the prediction based on the Gaussian Orthogonal Ensemble (GOE), $P_{\text{GOE}}(r) = (27/4)(r + r^2)/(1 + r + r^2)^{5/2} \Theta(1 - r)$ (solid line in Fig. 2.3 (b)), which is distinct from the Poisson prediction, $P_{\text{Poisson}}(r) = 2/(1 + r)^2 \Theta(1 - r)$ (dashed line in Fig. 2.3 (b)), where Θ is the Heaviside step function. This result indicate that this subspace as well as the entire Hamiltonian \hat{H}_1 is non-integrable.

Additionally, in the subspace without frozen regions, we numerically find the eigenstates with low entanglement in the bulk of the spectrum. The appearance of such states is a typical characteristics of systems with quantum many-body scar (QMBS) states [30, 27, 39]. In Fig. 2.3 (c), most of the other eigenstates with similar energies have similar values of entanglement entropy, in accordance with the ETH. Meanwhile, a small number of low-entangled eigenstates appear around specific values: $E = 0, \pm 1, \pm\sqrt{2}$ and $\pm\sqrt{6}$, which we thus regard as QMBS states. The origin of these states cannot be attributed to frozen regions as they are excluded in this subspace. We find that some of them originate from specific local structures of the adjacency graph of the Hamiltonian [168, 169]; see Appendix 2.E for details.

2.4.2 Subspaces with Integrability and quantum many-body scar states

Interestingly, we find that the one-dimensional PXP model and the XX model can be embedded as melting regions of the model \hat{H}_1 . First, let us discuss the emergent PXP model (see the area B in Fig. 2.1 (c)). In this one-dimensional region, all sites are adjacent to the frozen sites with up spins. Therefore, in this region, every spin can be flipped only when its two nearest neighbors are down due to the kinetic constraint. Hence, the system is effectively governed by

$$\hat{H}_B = \sum_{i \in B} \hat{\sigma}_i^x \frac{1}{4} (1 - \hat{\sigma}_{i+1}^z) (1 - \hat{\sigma}_{i-1}^z). \quad (2.6)$$

This is the one-dimensional PXP model, a well-known non-integrable model for hosting quantum many-body scars [29, 30, 170, 171, 172]. This implies that one observes a long-lived oscillation of an observable in this one-dimensional region if we prepare an appropriate initial configuration.

Second, let us briefly discuss the XX model (the area C in Fig. 2.1 (c)). In this region, the direction of the spin neighboring on the right side is opposite to that neighboring on the left side. We then find that the following Hamiltonian governs the dynamics in this region:

$$\hat{H}_C = \sum_{i \in C} \hat{\sigma}_i^x \frac{1}{2} (1 - \hat{\sigma}_{i+1}^z \hat{\sigma}_{i-1}^z). \quad (2.7)$$

This is the same as the effective Hamiltonian of the Ising chain in a weak transverse field [173] and is mappable to the XX chain [142], which is exactly solvable and thus ergodicity is broken due to the integrability. This implies that some subspaces become integrable when they only have a specific type of melting region.

2.5 Conclusion and outlook

In this Chapter, we have rigorously demonstrated that the effective model obtained from the d -dimensional Ising model in a weak transverse field on a hypercubic lattice exhibits the HSF for $d \geq 2$. In particular, the kinetic constraint, which is attributed to the emergent conservation of the DW number in this model, forms frozen regions that percolate the system. Consequently, each DW sector fractures into exponentially many isolated subspaces, leading to the violation of the ETH. We furthermore showed that there appear subspaces with integrability or non-integrable subspaces with the QMBS states.

Our results indicate that nontrivial initial-state dependence is observed for prethermal dynamics of the Ising models in a weak transverse field. Because the TFIM in two and three dimensions are experimentally realizable [73, 68, 174, 146, 67, 175, 176, 177], we believe that the model serves as a novel platform for observing the signatures of the HSF, which is distinct from previous experiments that required, e.g., tilted potentials [118, 119]. It is also worth mentioning that dynamically frozen spins can survive even if we consider higher-order corrections in our effective model as is discussed in Ref. [165], implying a long prethermal life-time of the nonergodicity in the TFIM. We leave it for future work to investigate the robustness of the transient non-ergodicity under long-range Ising interactions, which often arises in experiments.

There are other future directions. First, given that \hat{H}_{eff} is obtained as the perturbation in the weak-field limit of the TFIM, it will be interesting to see how properties of the Ising model without the transverse field, such as (classical) integrability and finite-temperature phase transition, affect physics in our model. Second, it is important to explore more about dynamical features of our effective model, for example, transport properties in the system. In fact, some other models with the HSF are shown to exhibit non-standard hydrodynamics physics [178]. We note, however, that the domain wall density in our effective model is observed to typically show the ordinary diffusion in Ref. [165], using a cellular automaton dynamics technique [179]. References [166, 180] considered the effective model in the presence of an additional weak longitudinal field and analytically investigate dynamics of smooth interfaces between regions with up spins and down spins, i.e., domain wall, by mapping the dynamics of the interfaces to that in one-dimensional integrable models. In this case, it has been shown that isolated domain walls show localization, oscillation and ballistic propagation depending on the initial configuration and the strength of the additional longitudinal field. Third, our findings are also relevant to quantum technologies. For example, absence of thermalization can be utilized for quantum sensing [181]. Indeed, in the next Chapter, we show that the HSF we find here can be employed to perform entanglement-enhanced sensing in an interacting system.

2.A Appendix: Expression of the projector \hat{Q}_i

Here, we present formal expression of \hat{Q}_i in arbitrary dimensions. Let us consider the system on a hypercubic lattice in d dimensions. The operator \hat{Q}_i projects all spin configurations onto the state space in which the sum of the z components of the $2 \times d$ spins surrounding the site i is zero. Then \hat{Q}_i can be formally given by

$$\hat{Q}_i = \prod_{n=1}^d \left((2n)^2 - \left(\sum_{j \in \text{ngbh}(i)} \hat{\sigma}_j^z \right)^2 \right) / (2n)^2. \quad (2.A.8)$$

For $d = 2$, for example, this expression is reduced to

$$\hat{Q}_i = \frac{5}{8} - \frac{1}{16} \left(\sum_{j \in \text{ngbh}(i)} \hat{\sigma}_j^z \right)^2 + \frac{3}{8} \prod_{j \in \text{ngbh}(i)} \hat{\sigma}_j^z. \quad (2.A.9)$$

and therefore the Hamiltonian $\hat{H}_1 = \sum_i \hat{\sigma}_i^x \hat{Q}_i$ in Eq. (2.4) contains five-body interaction on the square lattice.

2.B Appendix: Time evolution in the Ising model in a weak transverse field

The effective Hamiltonian \hat{H}_{eff} (as well as \hat{H}_1) describes the prethermal dynamics of the Ising model in a weak transverse field. Here we show the time evolution of observables according to the original Hamiltonian \hat{H}_{TFIM} (2.1) with a finite transverse field h_x and compare it with the time evolution for \hat{H}_{eff} (2.4). Note that, in the other Appendices in this Chapter, we perform numerical calculations on the system governed by \hat{H}_{eff} , not \hat{H}_{TFIM} .

Let us consider two initial product states $|\tilde{\psi}_1\rangle$ and $|\tilde{\psi}_2\rangle$ in a system of size 3×4 , as shown in Fig. 2.B.4 (a). These states have the same energy expectation value of \hat{H}_{TFIM} . In Fig. 2.B.4 (b), we show dynamics from these two initial product states according to the two Hamiltonians \hat{H}_{TFIM} and \hat{H}_{eff} , where we take $h_x = 0.3$. Specifically, we calculate the time evolution of the expectation value of the magnetization density. There is a good agreement between the dynamics with the original Hamiltonian and that with the effective Hamiltonian for a time range that we have adopted.

We also see from Fig. 2.B.4 (b) that the relaxation of the magnetization in the TFIM shows a strong dependence on the initial states. In the dynamics governed by \hat{H}_{eff} , there are only two melting sites and the other sites are frozen in $|\tilde{\psi}_1\rangle$ as shown in Fig. 2.B.4 (a). On the other hand, the entire system is melting in $|\tilde{\psi}_2\rangle$. This indicates that the two initial states belong to different subspaces in the fragmented Hilbert space of \hat{H}_{eff} . We can observe the emergence of the fragmented structure of the Hilbert space through the distinct behavior of the magnetization dynamics in the TFIM by preparing two different initial states.

As we decrease h_x to a smaller absolute value, the Hamiltonian \hat{H}_{eff} can approximate the dynamics of the TFIM for a longer time. To see this, we calculate the approximation error of

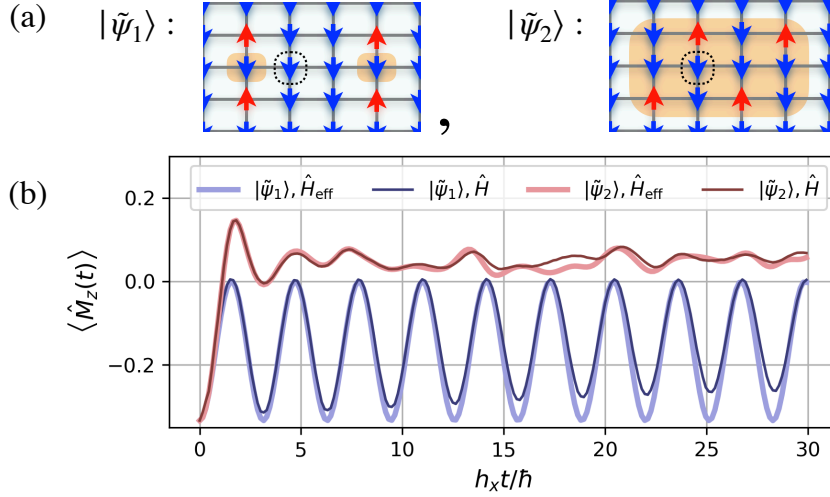


Figure 2.B.4: (a) Spin configurations of the two initial product states for a $N = 3 \times 4$ lattice, where four spins are up and the others are down. Regions with orange shades show the melting regions with respect to the effective Hamiltonian \hat{H}_{eff} . Sites surrounded by broken lines indicate the location of the spin which we consider in Fig. 2.B.5. We assume that the system is surrounded by fixed spins pointing down. (b) Time evolution of the expectation value of the magnetization $\hat{M}_z := (1/N) \sum_i \hat{\sigma}_i^z$ starting from the two initial states. Solid thin lines describe dynamics according to the TFIM's Hamiltonian \hat{H}_{TFIM} with $h_x = 0.3$ and solid thick lines show those of the effective Hamiltonian \hat{H}_{eff} . [Reproduced from Fig. S1 in Ref. [74].]

the time evolution of a spin $\hat{\sigma}_i^z$,

$$\epsilon(\hat{\sigma}_i^z, t) := |\langle \hat{\sigma}_i^z(t) \rangle_{\text{TFIM}} - \langle \hat{\sigma}_i^z(t) \rangle|, \quad (2.B.10)$$

where $\langle \hat{\sigma}_i^z(t) \rangle_{\text{TFIM}}$ and $\langle \hat{\sigma}_i^z(t) \rangle$ denote the expectation values which are evolved by the Hamiltonians \hat{H}_{TFIM} and \hat{H}_{eff} , respectively. We observe that the error $\epsilon(\hat{\sigma}_i^z, t)$ grows more slowly as we decrease the transverse field h_x as shown in Fig. 2.B.5 (a). In Fig. 2.B.5 (b), we show the time evolutions of the approximation errors that are rescaled by a power of the strength of the transverse field, i.e., $(h_x)^{-\alpha} \epsilon(\hat{\sigma}_i^z, t)$. We find that the rescaled errors collapse clearly when we take $\alpha = 2$, especially for a relatively small time range. The linear or slower rate at which the errors grow in Fig. 2.B.5 (b) implies that the approximation works well within a timescale that grows with $\sim 1/h_x^3$ as we decrease h_x . This is consistent with the fact that the generic upper bound on the error in Refs. [160, 161] as well as the bound that we introduce in the next Chapter increase as $\sim t/h_x^2$ ($< t/h_x^3$) for small $|h_x| \ll 1$.

2.C Appendix: Frozen regions and percolation

We here discuss that the frozen regions should percolate the system by observing that they cannot have corners. As we explain in Sec. 2.3.1, a frozen region \mathcal{F} satisfies the following condition: $\hat{Q}_i(|F\rangle \otimes |M\rangle) = 0$ for $\forall i \in \mathcal{F}$ and any $|M\rangle$ defined on Λ/\mathcal{F} , where $|F\rangle = \prod_{i \in \mathcal{F}} |s_i\rangle$ is a product state forming a sub-region \mathcal{F} on the entire lattice Λ and $|s_i\rangle$ denotes one of the eigenstates of $\hat{\sigma}_i^z$. We argue that a region with corners cannot be a frozen region.

Let us focus on a corner spin at site i belonging to a region with corners \mathcal{G} as exemplified in Figs. 2.C.6 (a) and (b) and consider its $2d$ adjacent sites. Among the adjacent sites, we assume

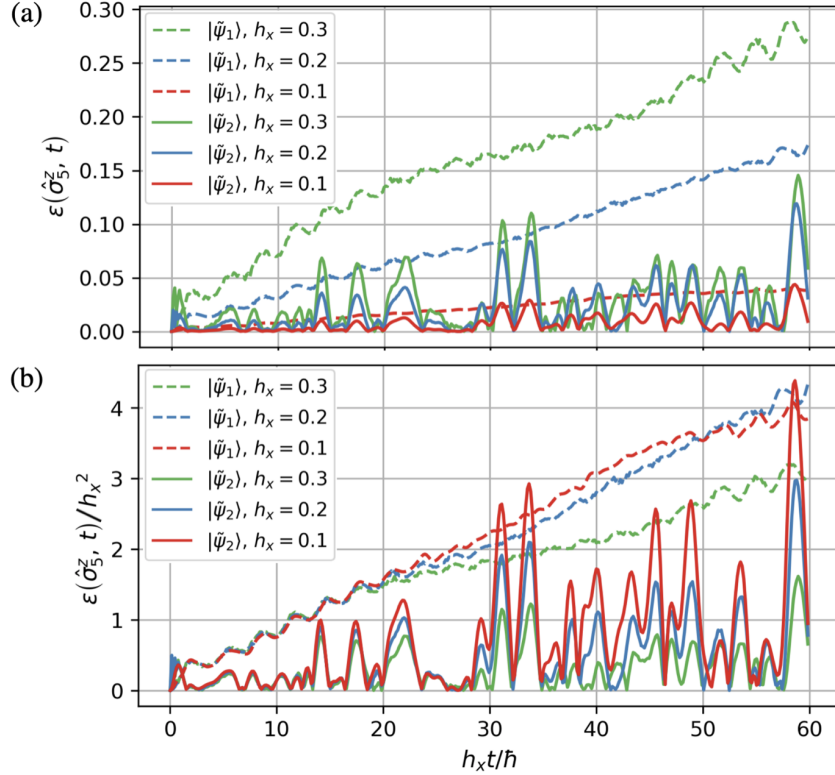


Figure 2.B.5: Time evolution of the approximation error $\epsilon(\hat{\sigma}_i^z, t)$ starting from the two initial states $|\tilde{\psi}_1\rangle$ (three solid lines) and $|\tilde{\psi}_2\rangle$ (three broken lines) given in Fig. 2.B.4 (a) with different values of the transverse field, $h_x = 0.1, 0.2$ and 0.3 . We calculate the errors for a spin (at the site $i = 5$) in the middle of the system which is indicated by the dashed squares in Fig. 2.B.4 (a). The lower panel (b) shows the same data in the panel (a) but are rescaled by the square of the strength of the transverse field, i.e., $(h_x)^{-2}\epsilon(\sigma_5^z, t)$. [Reproduced from Fig. S2 in Ref. [74].]

that j_{d+1}, \dots, j_{2d} belong to \mathcal{G} while j_1, \dots, j_d do not belong to \mathcal{G} (see Figs. 2.C.6 (a) and (b)). If \mathcal{G} were a frozen region, the spins on $i, j_{d+1}, \dots, j_{2d}$ would point fixed directions (up or down in the z direction), whereas j_1, \dots, j_d would belong to a melting region. Since the melting region is described by a superposition of various different spin configurations under the time evolution by \hat{H}_{eff} , the spin directions at every site j_k ($1 \leq k \leq d$) can be opposite to those at the corresponding sites j_{k+d} in one of the spin configurations, and the sum of the z components of all adjacent spins can be zero in this particular case. This means that the spin at site i can flip with a finite probability. This contradicts our assumption that \mathcal{G} is frozen. In conclusion, the above discussion indicates that if a region has corners surrounded by melting regions, the region generally cannot be frozen. Figure. 2.C.6 (c) illustrates an example of melting of spins on a region with corners. Even if all spins are aligned down in a region with corners (see gray-shaded region in Fig. 2.C.6 (c)), given that the region is surrounded by up spins, the spin flip will occur from the corners of the region, and the spin-flip region gradually spreads. Due to the condition on frozen spins, any frozen region should percolate the system. For a system with $d = 2$ under the periodic boundary conditions, they wrap around the torus in the x or y direction.

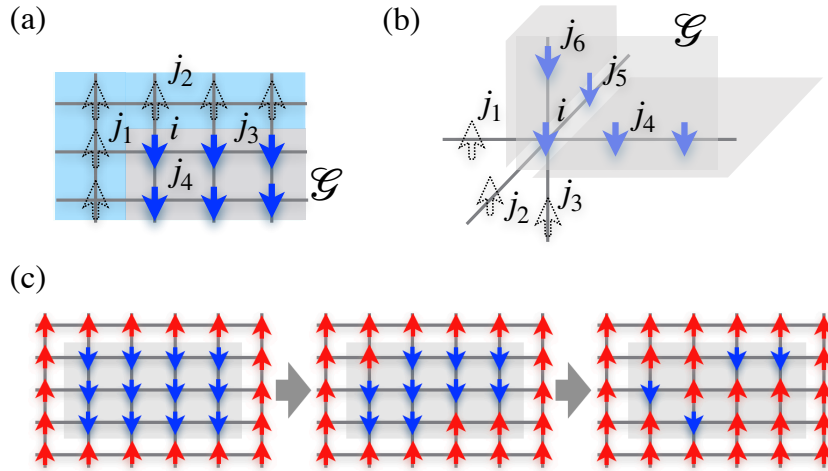


Figure 2.C.6: Spins around a corner of a region \mathcal{G} (gray shaded) (a) for $d = 2$ and (b) for $d = 3$ (panel (b)). (c) Example of melting of an aligned region with corners. [Reproduced from Fig. S3 in Ref. [74].]

2.D Appendix: Exponentially many frozen states

In this section, we demonstrate that the number of fragmented subspaces increases exponentially in the system size. In Sec. 2.3.1, we show that this system has not only frozen states but also subspaces with both frozen and melting regions, and that it leads to the fragmented Hilbert space. Here, we show that the number of frozen states as well as the subspaces with both frozen and melting regions increases exponentially. First, we illustrate one way of constructing many frozen states for a given DW number $n_{\text{DW}} = \alpha_{\text{tot}} N$, where α_{tot} denotes DW density with $0 < \alpha_{\text{tot}} < 2$, and N denotes the system size with $N \gg 1$. For brevity we consider a two-dimensional system with its total sites $N = L^2$ and assume $L/l \in \mathbb{N}$ for an odd integer $l = \mathcal{O}(1)$ in the following. First, we divide the system into N/l^2 subregions as we show in the rightmost figure in Fig. 2.D.7. Second, we consider embedding either spin configuration (p1) or (p2) into each divided subregion, where (p1) denotes an example of an almost staggered configuration

and (p2) denotes an example of an all-up configuration as shown in Fig. 2.D.7. The DW density for each configuration (p1) and (p2) is given by $\alpha_{p1} = 2 - (8l - 10)/l^2$ and $\alpha_{p2} = 0$. In this case, the total number of all possible combinations of the embedding is estimated as

$$(N/l^2)! / (k!(N/l^2 - k)!) = \exp[\mathcal{O}(N)], \quad (2.D.11)$$

where $k = \mathcal{O}(N)$ satisfies $\alpha_{\text{tot}}N = \alpha_{p1}kl^2 + \alpha_{p2}(N - kl^2)$. This indicates that the number of frozen states constructed in the above procedure increases exponentially in the system size N in any DW sectors with finite DW densities.

We extend the above discussion to the case of the subspace with both frozen and melting regions. The configurations (p1) and (p2) should be replaced following the discussion below. As in (p1) and (p2), we consider the configurations that consist of the inner part where each spin can point up or down and the outer frozen part surrounding it where the spins always point up. Here, it is guaranteed that the outer spins are freezing because the spins always point up on the edges of the adjacent subsystems in our configuration. Then, if we want to create subspaces that are partially frozen and partially melting, we can replace (p1) or (p2) with another configuration in which the inner parts are melting.

In addition, we can easily extend the above construction to the three-dimensional case. Instead of a square, we can consider a cube whose surface consists of frozen up spins. For the inner parts, the same discussion as the two-dimensional case can be done for the three-dimensional case.

Finally, it should be noted that the configurations illustrated here are just possible examples, and that there are indeed far more diverse and numerous possible subspaces associated with configurations of frozen or melting regions. We also note that Ref. [165] gives a similar analytical discussion on the number of disconnected subspaces in the entire Hilbert space, while our discussion above focuses on the number of subspaces in each DW sector.

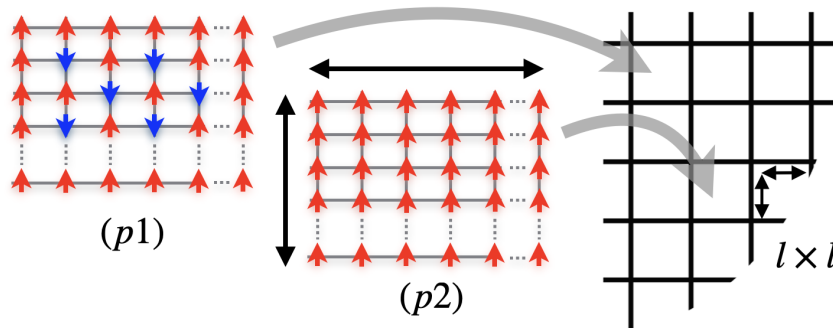


Figure 2.D.7: Construction of frozen states. (p1) and (p2) describe possible spin configurations for subsystems with $l \times l$ sites. We can construct frozen states by embedding either spin configurations (p1) [almost staggered configuration] or (p2) [all-up configuration] as the subregions of the total system in the rightmost figure, which is divided into separated subregions. [Reproduced from Fig. S4 in Ref. [74].]

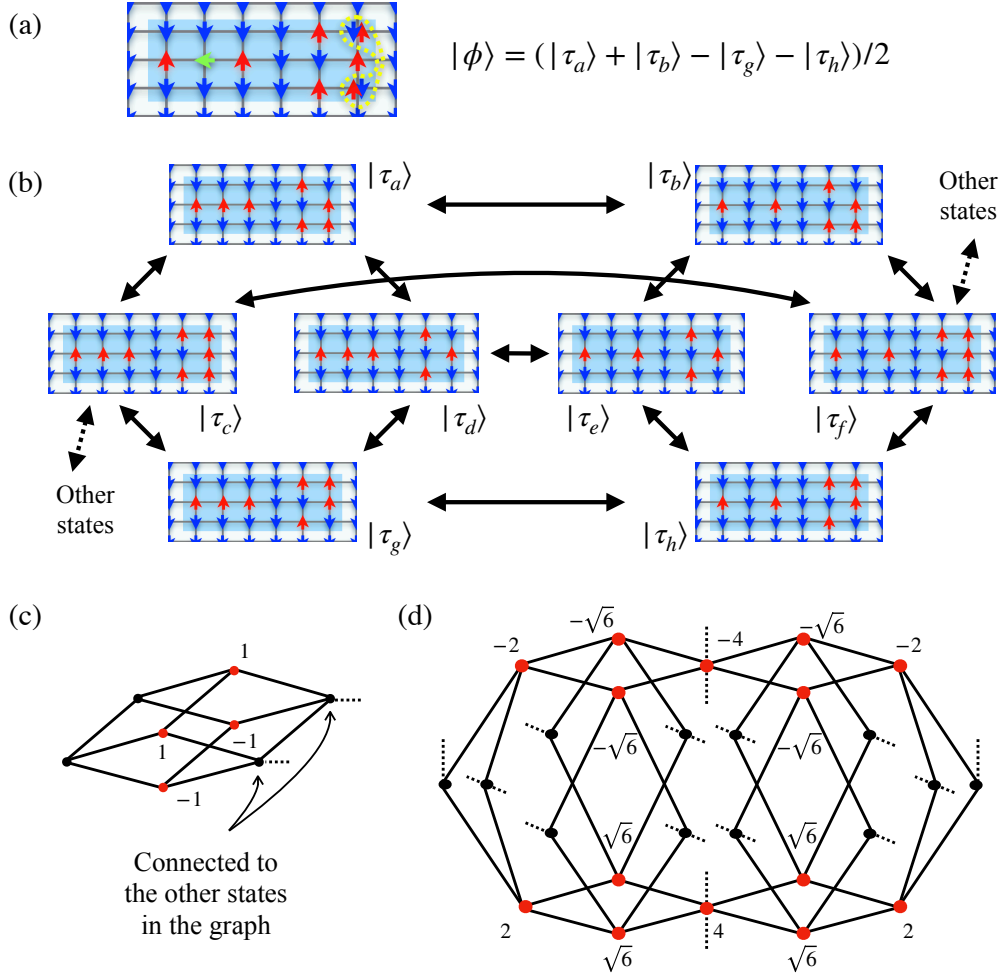


Figure 2.E.8: (a) Schematic picture of a zero-entanglement eigenstate $|\phi\rangle$ with the energy 1 in Fig. 2.3 (c). Red and blue arrows on each lattice site represent up and down spins in $\hat{\sigma}_i^z$ basis, respectively. The green arrow represents the spin pointing to the x direction, i.e., the eigenstate of $\hat{\sigma}_i^x$ with the eigenvalue $+1$, and the spins surrounded by the yellow broken line form a spin-singlet state. (b) Schematic picture of local structure of the adjacency graph that generates the localized eigenstate $|\phi\rangle$. Black arrows indicate that the two spin configurations are connected by the off-diagonal elements of the Hamiltonian matrix. The states $|\tau_c\rangle$ and $|\tau_f\rangle$ are connected with other states in the bulk of the graph which are not shown here. (c, d) Examples of local graph structures that give rise to localized energy eigenstates. The graph in (c) describes the same graph structure as in (b). Red nodes represent the basis with non-zero amplitudes in a localized energy eigenstate with the eigenenergy $E = 1$ [$E = \sqrt{6}$] for (c) [(d)], and the numbers associated with the red nodes represent the actual values of the amplitude (before normalization). [Reproduced and modified from Fig. S5 in Ref. [74].]

2.E Appendix: Atypical states in the subspace without frozen regions

In Fig. 2.3 (c), we find that some eigenstates show zero bipartite entanglement even in the subspace without frozen regions. They have specific energies $E = 0, \pm 1, \pm\sqrt{2}$, and $\pm\sqrt{6}$ in our calculation in Fig. 2.3 (c). Here we discuss the origin of these states. We specifically focus on the eigenstates with non-zero energies. For the energy eigenstates with zero energy, the analysis is difficult due to the large degeneracy. In fact, it is known that the presence of the chiral symmetry and spatial inversion symmetry together induces exponentially many zero-energy eigenstates [182]. However, we numerically observe that the degeneracy is not always lifted by the addition of longitudinal random fields, which breaks the symmetries. We leave investigation of these zero-energy states for future work.

We find that the origin of some atypical states in Fig. 2.3 (c) is well captured by an adjacency graph of the Hamiltonian \hat{H}_1 , where the nodes represent the computational-basis states and the edges between the nodes describe the connections by the off-diagonal elements of the Hamiltonian (see Fig. 2.E.8). The atypical eigenstates correspond to wave functions that are localized on a part of the adjacency graph, which we call localized energy eigenstates. We use the word of “localized energy eigenstate” in order to refer to an eigenstate composed of superpositions of a small number of computational basis states. Similar states with low entanglement which are associated with the structure of the adjacency graph have been discussed recently [168, 169]. Localized eigenstates in a similar setting are also studied for example in Refs. [183, 184, 185], where the graph in these context is defined on the real space.

Figure 2.E.8 (a) describes one of the localized eigenstates with $E = 1$. In this case, the state $|\phi\rangle$ in Fig. 2.E.8 (a) is identified as a superposition of four computational basis states. These basis states are connected to other basis states in the subspace on the adjacency graph as we illustrate in the diagram in Fig. 2.E.8 (b). The part of the adjacency graph is described in Fig. 2.E.8 (c), where red nodes represent the basis states with non-zero amplitudes in the localized energy eigenstate $|\phi\rangle$. (Note that the diagram in Fig. 2.E.8 (b) represents the same state described by the graph in Fig. 2.E.8 (c).)

In general, when \hat{H}_1 acts on one of the basis states, it becomes a superposition of several basis states. However, the state $|\phi\rangle$ is still localized on the graph due to a destructive interference on the other nodes, which allows $|\phi\rangle$ to be an eigenstate of \hat{H}_1 . Such eigenstates that are expanded by only a few number of basis states have only limited amount of entanglement and even show zero entanglement entropy when the bipartite cut is set suitably.

There are various types of local structures of the adjacency graph which allow for localized eigenstates. Figure 2.E.8 (c) and (d) show two examples of such structures. As is exemplified by the state $|\phi\rangle$, localized eigenstates appear when a part of the adjacency graph of the Hamiltonian has a structure that induces the destructive interference. Indeed, low-entangled eigenstates with $E = \pm 1, \pm\sqrt{2}$, and $\pm\sqrt{6}$ (and a part of the eigenstates for $E = 0$) in Fig. 2.3 (c) are identified as localized eigenstates on the adjacency graph with local structures described either in Fig. 2.E.8 (c) or (d).

Finally, from numerical simulations, we observe oscillatory behavior associated with the localized eigenstates, which is a typical signature of quantum many-body scarred systems [29, 30, 170, 186, 187]. In Fig. 2.E.9 (b), we show dynamics of the magnetization starting from two initial states in Fig. 2.E.9 (a). Specifically, we calculate the time evolution of the expectation value of the magnetization density for a system surrounded by fixed down spins. For typical

initial states such as the state $|\overline{\psi}_1\rangle$ in Fig. 2.E.9 (a), the system rapidly relaxes to a steady state. However, for the initial state $|\overline{\psi}_2\rangle$ in Fig. 2.E.9 (a), namely the state $|\tau_a\rangle$ in Fig. 2.E.8 (b), which has a large overlap with the localized eigenstate $|\phi\rangle$, we observe a long-time oscillation; see Fig. 2.E.9 (b). This result, combined with the other results in this Chapter, suggests that our model possesses various types of quantum many-body scar states in some subspaces such as localized eigenstates and those mappable to the PXP model [30, 170, 171, 172].

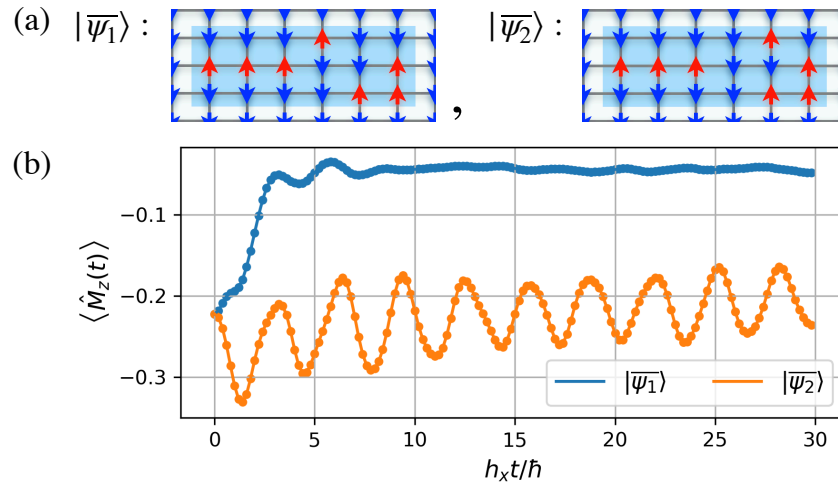


Figure 2.E.9: (a) Spin configurations of the two initial states. We take the fixed boundary condition surrounded by down spins. Note that the state $|\overline{\psi}_2\rangle$ corresponds to the state $|\tau_a\rangle$ in Fig. 2.E.8 (b). (b) Magnetization dynamics for two initial product states according to \hat{H}_1 . We numerically calculate the evolution of the expectation value of the magnetization $\hat{M}_z := (1/N) \sum_i \hat{\sigma}_i^z$ for a $N = 3 \times 6$ lattice. [Reproduced from Fig. S6 in Ref. [74].]

Chapter 3

Quantum Metrology Protected by Hilbert Space Fragmentation

In this Chapter, we consider a new approach to perform quantum sensing using a probe systems with always-on interaction. Specifically, we propose an entanglement-enhanced sensing scheme that is robust against spatially inhomogeneous always-on Ising interactions. Our strategy is to tailor quantum coherent dynamics by employing the Hilbert-space fragmentation (HSF) in the quantum Ising models, which we have studied in the previous Chapter. We analytically show that the emergent HSF enables us to design a stable state in which a part of the spins is effectively decoupled from the rest of the system. Using the decoupled spins as a probe to measure a transverse field, we demonstrate that the Heisenberg limit is achieved without being obstructed by thermalization.

This Chapter is organized as follows. First, we give the introduction of this Chapter in Sec. 3.1. Then in Sec. 3.2, after introducing the model and notations in this Chapter, we discuss how the presence of interactions affect sensitivities of conventional sensing schemes. We introduce our quantum sensing scheme in Sec. 3.3, which uses the HSF that approximately appears in a weak transverse field to protect desired coherence in the probe state. Section. 3.3.2 briefly discusses the sensitivity of our scheme for a finite target transverse field in an analytical way. We then mention applicability of our scheme and propose an approach for the state preparation in Sec. 3.4, before concluding this Chapter in Sec. 3.5. We also have appendices as Secs. 3.A–3.C to give analytical derivations on our evaluations in Secs. 3.2.2 and 3.3.2

3.1 Introduction

Taming entanglement and coherence of a multiple qubit system is a crucial task in today's quantum technology. One of the most notable applications featuring quantum advantage is quantum metrology, in which entanglement enables enhanced sensitivity in evaluating external fields [188, 189, 46]. For a given number N of probe spins to measure the fields, the uncertainty in the estimation can be reduced in proportion to N^{-1} for entangled states, which is called the Heisenberg limit (HL). In contrast, the corresponding scaling for separable states becomes only $N^{-1/2}$, which is known as the standard quantum limit (SQL). Due to the fundamental and practical interests, quantum metrology has extensively been studied both theoretically [190, 191, 192, 49, 193, 194] and experimentally [195, 196, 197, 198, 199].

One major challenge for quantum metrology is to precisely control the dynamics of many-

body interacting systems. On the one hand, interactions among qubits are necessary for preparing entangled states. On the other hand, complicated interactions, which are in general spatially inhomogeneous in actual experiments, make the many-body system thermalize. In fact, recent studies on quantum dynamics elucidate that even isolated system can thermalize due to the eigenstate thermalization hypothesis (ETH) [6, 7, 92, 8], which states that every energy eigenstate becomes locally thermal. This effect of thermalization [57] would spoil the sensitivity more severely when target magnetic fields become weaker than the interactions.

To overcome this unwanted effect of interactions, several approaches have been proposed. One possible approach is the dynamical decoupling, in which we actively perform a sequence of pulses to eliminate unwanted terms in Hamiltonians [200, 201, 202, 203, 58]. In general, this method demands a large number of precise pulses applied to the probe system. Another recent approach [181] that does not involve active operations is to utilize quantum many-body scars [29, 30, 204, 39, 205], which are non-thermalizing eigenstates in certain interacting Hamiltonians. However, the approach is based on Hamiltonians with fine-tuned interactions and hence susceptible to, e.g., spatially inhomogeneous perturbations.

Hilbert space fragmentation (HSF) is another novel mechanism that prohibits thermalization in interacting non-integrable systems and has gathered recent attention [34, 35, 36, 27, 28, 116, 39]. In some models with kinetic constraints, the Hilbert space is fractured into exponentially many invariant subspaces, which leads to non-ergodicity (see also Sec. 1.3.5). This phenomenon also appears in an effective model that describes the transverse-field Ising model (TFIM) in the limit of a weak field [74, 165, 166], as we have shown in the previous Chapter. In this model, eigenstates can involve “frozen regions,” in which spins in the z direction cannot be dynamically flipped. The eigenstates with frozen regions appear due to a constraint arising from the emergent conservation of the interaction energy in the weak-field limit and break the ETH and thermalization. Notably, the structure of the HSF does not rely on the translation invariance and fine-tuning of the Hamiltonian.

In the present Chapter, we propose a novel entanglement-enhanced sensing scheme in a strongly interacting inhomogeneous Ising model, in which the emergent HSF protects the relevant quantum coherence against interactions. Our strategy is to design a metrologically useful state arranged as in Fig. 3.1 (a,b), in which the probe spins are embedded in the ancillary spins. This state belongs to one of the fragmented subspaces in the TFIM in the weak-field limit, where the HSF emerges as shown in Fig. 3.1 (c) for the leading order approximation, and thus evades fast thermalization. More concretely, the probe spins undergo tailored coherent dynamics just with additional bias fields, being decoupled from the ancillary spins that are dynamically frozen. We rigorously show that our scheme reaches the Heisenberg-limited sensitivity in estimating the target transverse field for sufficiently strong interactions. Our method is robust under various perturbations, such as inhomogeneity, additional longitudinal fields, and certain changes in the lattice structure and spatial dimensions.

3.2 Quantum sensing in an interacting system

3.2.1 Model and the Ramsey sensing scheme

We consider a system of spin-1/2 particles (qubits) with always-on Ising interactions between them. We here assume that the spins are arranged on a square lattice, although generalization to higher dimensions and other types of lattices are straightforward. The system is exposed to

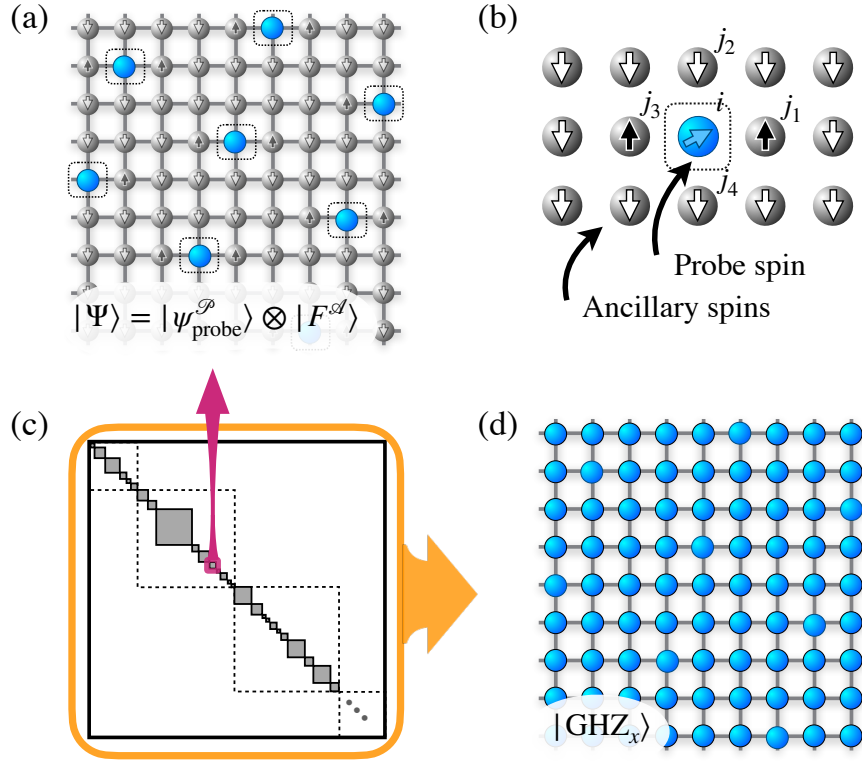


Figure 3.1: (a) Schematic of how we split the system into probe spins and ancillary spins for our quantum sensing scheme. The blue sites surrounded by the dotted lines represent the probe spins, and the other gray sites correspond to the ancillary spins. (b) Spin configuration around a probe spin in (a), which induces dynamical freezing of the ancillary ones. Each ancillary spin is an eigenstate of $\hat{\sigma}_i^z$, which corresponds to either spin-up or down state. (c) Schematic picture of the emergent Hilbert space fragmentation (HSF) in our transverse-field Ising model in the weak-field limit. Emergent conservation law of the number of domain walls block-diagonalizes the Hamiltonian, which is further block-diagonalized due to the HSF. (d) Illustration of the GHZ state on a square lattice, which is used as a probe state in the conventional approach. [Reproduced and modified from Fig. 1 in Ref. [75].]

a weak target magnetic field with magnitude ω_x , which we try to estimate by quantum sensing. The Hamiltonian is then given by

$$\hat{H}_{\text{TFIM}} = \hat{H}_{\omega_x} + \hat{H}_{\text{int}}, \quad (3.1)$$

$$\hat{H}_{\omega_x} = \frac{\omega_x}{2} \sum_i \hat{\sigma}_i^x, \quad (3.2)$$

$$\hat{H}_{\text{int}} = - \sum_{\langle i,j \rangle} J_{ij} \hat{\sigma}_i^z \hat{\sigma}_j^z. \quad (3.3)$$

where $\langle i, j \rangle$ indicates that the sites i and j are nearest neighbors and we set $\hbar = 1$. Here, $J_{ij} = \bar{J} + \Delta J_{ij}$ denotes the Ising coupling constant, where \bar{J} does not depend on $\langle i, j \rangle$. We assume that $|\Delta J_{ij}|$ does not exceed $|\bar{J}|/2$, i.e., $\max_{i,j} 2|\Delta J_{ij}|/|\bar{J}| =: k < 1$. Without loss of generality, we consider the ferromagnetic case hereafter, namely $\bar{J} > 0$.

Throughout this Chapter, we adopt the Ramsey scheme [46] summarized as follows: (i) we prepare initial probe spins in a metrologically useful state; (ii) we let them exposed to the static target field, whose Hamiltonian is given by \hat{H}_{ω_x} , for an interaction time T_{int} ; (iii) we perform a projective measurement described by an operator \hat{P}_s and obtain an outcome; and (iv) we estimate the value of ω_x from the outcome obtained by the repetition of (i)-(iii). The uncertainty in the estimation of ω_x under this scheme is calculated as

$$\delta\omega_x = \frac{\Delta P_s}{\left| \frac{\partial P_s}{\partial \omega_x} \right| \sqrt{M}}, \quad (3.4)$$

where $P_s = \langle \hat{P}_s \rangle$ denotes the expectation value of \hat{P}_s , which corresponds to the probability for the projection onto the desired basis to successfully occur. Here, $\Delta P_s = \sqrt{P_s(1 - P_s)}$ denotes the standard deviation of \hat{P}_s and M denotes the number of repetitions of the measurements [5]. For a total available time T_{all} , the number M is calculated as $M = T_{\text{all}}/T_{\text{sensing}}$, where T_{sensing} denotes a combined time of the three procedures (i)-(iii) of the sensing scheme. For simplicity, below we take $T_{\text{sensing}} = T_{\text{int}}$ by assuming that T_{int} for (ii) is much longer than the duration for (i) and (iii).

To begin with, let us consider quantum sensing in the absence of the interaction \hat{H}_{int} . In this case, we can estimate ω_x with the HL by preparing the Greenberger-Horne-Zeilinger (GHZ) state $|\text{GHZ}_x\rangle := (\bigotimes_{j=1}^N |+\rangle_j + \bigotimes_{j=1}^N |-\rangle_j)/\sqrt{2}$ as a probe state [125, 206] in (i), where $|\pm\rangle_j$ denote the eigenstates of $\hat{\sigma}_j^x$ with eigenvalues ± 1 and N denotes the number of spins. After this initial state acquires the relative phase $\omega_x N T_{\text{int}}$ through (ii), we perform a projective measurement $\hat{P}'_s = |\text{GHZ}'_x\rangle\langle\text{GHZ}'_x|$ with $|\text{GHZ}'_x\rangle := (\bigotimes_{j=1}^N |+\rangle_j + i \bigotimes_{j=1}^N |-\rangle_j)/\sqrt{2}$ in (iii), and finally we estimate ω_x from the relation $\langle \hat{P}'_s \rangle = (1/2)(1 + \sin(\omega_x N T_{\text{int}}))$. Throughout this Chapter, we assume that the target field ω_x is weak and satisfies $\omega_x N T_{\text{int}} = \mathcal{O}(N^0) \ll 1$. We also assume $T_{\text{int}} = \mathcal{O}(N^0)$ unless otherwise mentioned. The uncertainty $\delta\omega_x$ of the estimation is then calculated from [Eq. (3.4)] as $\delta\omega_x = N^{-1}(T_{\text{int}} T_{\text{all}})^{-1/2}$. This demonstrates that the HL is achieved by using the GHZ state in the absence of the internal interaction \hat{H}_{int} .

3.2.2 Sensitivity in a conventional sensing scheme in the presence of the interaction

However, the sensitivity decreases when \hat{H}_{int} is taken into consideration. Due to the flipping of spin states from $|\pm\rangle_i|\pm\rangle_j$ to $|\mp\rangle_i|\mp\rangle_j$ caused by Ising-type interactions of \hat{H}_{int} , the probe state after (ii) no longer remains in a simple superposition of $\bigotimes_{j=1}^N |+\rangle_j$ and $\bigotimes_{j=1}^N |-\rangle_j$. To show the destructive effect of the interaction, we show in Fig. 3.2 (a) the time evolution of the dynamical fidelity $F_d(t) := \left| \langle \text{GHZ}_x | e^{i\hat{H}_{\omega_x}t} e^{-i\hat{H}_{\text{TFIM}}t} | \text{GHZ}_x \rangle \right|^2$, which quantifies the difference between the ideal state evolved by \hat{H}_{ω_x} and the actual state evolved by \hat{H}_{TFIM} with nonzero interaction \hat{H}_{int} . The rapid decay of $F_d(t)$ in Fig. 3.2 (a) implies that the probe state is unstable under the effect of the interaction. The decay rate increases as the interaction becomes stronger. This implies that naive sensing with the GHZ states, as illustrated in Fig. 3.1 (d), will be challenging, especially under the strong always-on Ising interactions.

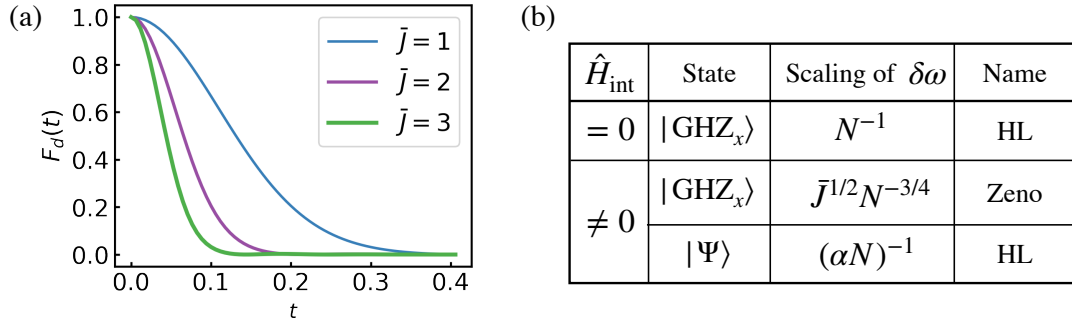


Figure 3.2: (a) Decay of the dynamical fidelity $F_d(t)$, which compares the time evolutions from the GHZ state $|\text{GHZ}_x\rangle$ with respect to \hat{H}_{ω_x} and \hat{H}_{TFIM} for three values of \bar{J} . We use an $N = 3 \times 4$ square-lattice system surround by fixed down spins. Spatial fluctuations of the interaction ΔJ_{ij} are generated from Gaussian random variables by setting the mean and the variance as zero and $0.3\bar{J}$, respectively. We fix the transverse field $\omega_x = 0.4$ in all of the cases. (b) The asymptotic dependence of $\delta\omega_x$ on N and the interaction strength \bar{J} for three Ramsey schemes. We compare the sensing schemes using initial states that are explained in the caption of Fig. 3.1, where we take $|\psi_{\text{probe}}^{\mathcal{P}}\rangle = |\text{GHZ}_x^{\mathcal{P}}\rangle$ for the state $|\Psi\rangle$ here. [Reproduced and modified from Fig. 2 in Ref. [75].]

We note that it is possible to achieve a sensitivity beyond the SQL but below the HL with our model using the GHZ state. The idea is to appropriately tune the interaction time T_{int} in the step (ii) so that the effects from the interaction are minimized. Specifically, if we decrease T_{int} as $T_{\text{int}} = \mathcal{O}(\bar{J}^{-1} N^{-1/2})$ for increasing N , the uncertainty in the estimation scales as $\delta\omega_x = \mathcal{O}(\bar{J}^{1/2} N^{-3/4})$; see Appendix 3.A for more detail. This scaling is called the Zeno scaling [207, 208, 198]. While the scaling exceeds the SQL, it is still unsatisfactory since the sensitivity becomes severely worse as the interaction strength increases.

3.3 HSF-protected quantum metrology

3.3.1 Description of our sensing scheme

We now illustrate our entanglement-enhanced sensing scheme that is robust against strong always-on-Ising coupling with spatial inhomogeneity. Instead of using all spins as a probe (see also Fig. 3.1 (d)), we design a state such that a fraction of probe spins are embedded in the ancillary spins as shown in Fig. 3.1 (a). Specifically, we take the following initial state in step (i):

$$|\Psi\rangle := |\psi_{\text{probe}}^{\mathcal{P}}\rangle \otimes |F^{\mathcal{A}}\rangle \quad (3.5)$$

Here, $|\psi_{\text{probe}}^{\mathcal{P}}\rangle$ denotes a state of αN probe spins, and $|F^{\mathcal{A}}\rangle$ denotes that of $(1 - \alpha)N$ ancillary spins, where we take a constant α as $\alpha = 1/11$. The superscript \mathcal{P} (\mathcal{A}) indicates that the state is defined on probe (ancillary) spins. Figure 3.1 (a) illustrates how we divide the system into these two groups of spins. Each probe spin is interspersed among the ancillary spins that are in the eigenstates of $\hat{\sigma}_j^z$. Figure 3.1 (b) illustrates the spin configuration of the ancillary spins around each probe spin in Fig. 3.1 (a). Each probe spin is surrounded by ancillary spins with two up spins (see the sites j_1 and j_3 in Fig. 3.1 (b)) and two down spins (see the sites j_2 and j_4 in Fig. 3.1 (b)).

Notably, our model exhibits the HSF in the weak-transverse-field limit, which makes $|\Psi\rangle$ a non-ergodic state with $|F^{\mathcal{A}}\rangle$ being a frozen region and leads to the coherent time-evolution of $|\psi_{\text{probe}}^{\mathcal{P}}\rangle$ in step (ii). Here, “frozen” means that the spins cannot be flipped under the time evolution. In particular, we show that the following approximation holds for any observable \hat{P}_s with large \bar{J}/ω_x :

$$\langle \Psi | e^{i\hat{H}_{\text{total}}t} \hat{P}_s e^{-i\hat{H}_{\text{total}}t} | \Psi \rangle \simeq \langle \Psi | e^{i\hat{H}_{\omega_x}^{\mathcal{P}}t} \hat{P}_s e^{-i\hat{H}_{\omega_x}^{\mathcal{P}}t} | \Psi \rangle, \quad (3.6)$$

where $\hat{H}_{\text{total}} = \hat{H}_{\text{TFIM}} + \hat{H}_{\text{shift}}^{\mathcal{P}}$ and

$$\hat{H}_{\omega_x}^{\mathcal{P}} := \frac{\omega_x}{2} \sum_{i \in \text{probe}} \hat{\sigma}_i^x, \quad (3.7)$$

$$\hat{H}_{\text{shift}}^{\mathcal{P}} := - \sum_{i \in \text{probe}} h_i^z \hat{\sigma}_i^z. \quad (3.8)$$

Here, “ $i \in \text{probe}$ ” indicates that the sum is taken over all probe spin sites. As detailed below, we tune h_i^z in $\hat{H}_{\text{shift}}^{\mathcal{P}}$ so that we can cancel out effective longitudinal fields on probes that arise due to \hat{H}_{int} . Equation (3.6) suggests that the probe spins are decoupled from the rest of the interacting but dynamically frozen spins and exposed only to the target field $\hat{H}_{\omega_x}^{\mathcal{P}}$.

To understand Eq. (3.6), we first note that a spin flip by \hat{H}_{ω_x} with small ω_x is suppressed when the flip causes a large change in the energy due to $\hat{H}_{\text{int}} + \hat{H}_{\text{shift}}^{\mathcal{P}}$. For simplicity, let us start from the case with $\Delta J_{ij} = h_i^z = 0$ and $\omega_x/\bar{J} \rightarrow 0$. In this case, the large interaction \hat{H}_{int} leads to a constraint that a spin can flip only when two surrounding spins are up and the other two surrounding spins are down. This constraint results in the occurrence of the HSF as studied in Refs. [74, 165]; the effective Hamiltonian has a block-diagonal structure by the emergent conservation law of the domain-wall (DW) number $\hat{n}_{DW} := \sum_{\langle i,j \rangle} (1 - \hat{\sigma}_i^z \hat{\sigma}_j^z)/2$, which is further fragmented nontrivially as shown in Fig. 3.1 (c). This suggests non-ergodicity even within each sectors.

We next argue that a similar HSF emerges for $\Delta J_{ij} \neq 0$ and that $|\Psi\rangle$ corresponds to a state in one of the fragmented subspaces. More concretely, $|F^A\rangle$ constitutes a frozen region; from the construction given in Fig. 3.1 (b), every ancillary spin is always surrounded by at least three down spins. Then, the action of \hat{H}_{ω_x} is energetically suppressed on this region even for nonzero ΔJ_{ij} , since the magnitude of the fluctuation ΔJ_{ij} is assumed not to exceed $\bar{J}/2$. Thus, $|F^A\rangle$ becomes dynamically stable in the limit of $\omega_x/\bar{J} \rightarrow 0$, independent of the state of the probe spins $|\psi_{\text{probe}}^{\mathcal{P}}\rangle$. Due to the constraint, such a frozen region appears in other configurations as well, leading to exponentially many invariant subspaces, which means the occurrence of the HSF. Our designed initial state $|\Psi\rangle$ then belongs to one of such subspaces and time-evolves only within it; see Figs. 3.1 (a) and (c). Note that this is in contrast to the GHZ state of all spins, i.e., $|\text{GHZ}_x\rangle := (\bigotimes_{j=1}^N |+\rangle_j + \bigotimes_{j=1}^N |-\rangle_j)/\sqrt{2}$, which contains a superposition of many computational basis states that spread across the fragmented subspaces; see Figs. 3.1 (c) and (d).

We now discuss the origin of $\hat{H}_{\omega_x}^{\mathcal{P}}$ in Eq. (3.6), focusing on probe spins. Since each probe spin is surrounded by two up and two down frozen spins, the probe spin is effectively exposed to an effective longitudinal magnetic field $\tilde{h}_i^z = -\Delta J_{ij_1} + \Delta J_{ij_2} - \Delta J_{ij_3} + \Delta J_{ij_4}$; see Fig. 3.1 (b). Assuming that \tilde{h}_i^z is known from calibration, we can cancel the effective field by choosing $h_i^z = -\tilde{h}_i^z$ in Eq. (3.8). Therefore, \hat{H}_{total} acting on our state $|\Psi\rangle$ is reduced to $\hat{H}_{\omega_x}^{\mathcal{P}}$ for $|\omega_x/\bar{J}| \ll 1$ (specifically under the first-order approximation in the degenerate perturbation theory based on the Schrieffer-Wolff transformation (SWT) [162, 163, 158, 164]; see Sec. 2.2 in the previous Chapter).

In our scheme, we perform the Ramsey sensing (i)–(iv) with the following two modifications. First, we only use the probe spins as a resource of metrology and make the other spins ancillary. In other words, we prepare $|\Psi\rangle$ with $|\psi_{\text{probe}}^{\mathcal{P}}\rangle = |\text{GHZ}_x^{\mathcal{P}}\rangle$ in (i) and readout outcomes by using a projective operator $\hat{P}_s = |\text{GHZ}'_x^{\mathcal{P}}\rangle\langle\text{GHZ}'_x^{\mathcal{P}}| \otimes \hat{I}^A$ in (iii). Second, we additionally apply the shift field $\hat{H}_{\text{shift}}^{\mathcal{P}}$ to the probe spins during the exposure (ii). This shift field is used to cancel out the effective fields on probe spins originating from interactions with the ancillary spins, which are dynamically frozen for $\omega_x/\bar{J} \rightarrow 0$. In this limit, Eq. (3.6) is exact, and the uncertainty is calculated as $\delta\omega_x = (\alpha N)^{-1}(T_{\text{int}}T_{\text{all}})^{-1/2}$, which demonstrates the Heisenberg-limited sensitivity. Our scheme does not require turning off the interactions or controlling T_{int} during the interrogation process.

The table in Fig. 3.2 (b) summarizes three schemes that we introduced in this Chapter. The sensing scheme that uses the state $|\text{GHZ}_x\rangle$ of all spins would not achieve the HL in the presence of the Ising interactions although it can show an entanglement-enhanced sensitivity. In contrast, our scheme that uses $|\Psi\rangle$ (the state $|\text{GHZ}_x^{\mathcal{P}}\rangle$ only for probe spins) can indeed achieve the HL under large enough couplings \bar{J}/ω_x . (Note that the Zeno scaling for the case with $\hat{H}_{\text{int}} \neq 0$ and the state $|\text{GHZ}_x\rangle$ is achieved by shortening the duration of time T_{int} as N or \bar{J} increases, in contrast to the other two cases, where T_{int} is assumed to be a constant.)

3.3.2 Stability for finite ω_x/\bar{J}

While the freezing of the ancillary spins discussed above is exact only for $\omega_x/\bar{J} \rightarrow 0$, we here analytically show that the HL is still achieved in our scheme even for sufficiently small but finite ω_x/\bar{J} . To see this, we first evaluate the uncertainty of ω_x by taking account of the deviation $\epsilon(t)$

from the approximation in Eq. (3.6) (see Appendix 3.B for the derivation):

$$\delta\omega_x = \frac{1}{aN T_{\text{int}}} \left(\frac{\langle \hat{P}_s \rangle_{\text{actual}} (1 - \langle \hat{P}_s \rangle_{\text{actual}})}{M} + |\epsilon(T_{\text{int}})|^2 \right)^{1/2}, \quad (3.9)$$

where $\epsilon(t) := \langle \hat{P}_s \rangle_{\text{actual}} - \langle \hat{P}_s \rangle_{\text{eff}}$ denotes the difference between $\langle \hat{P}_s \rangle_{\text{actual}} := \langle \Psi | e^{i\hat{H}_{\text{total}}t} \hat{P}_s e^{-i\hat{H}_{\text{total}}t} | \Psi \rangle$ and $\langle \hat{P}_s \rangle_{\text{eff}} := \langle \Psi | e^{i\hat{H}_{\omega_x}^{\mathcal{P}}t} \hat{P}_s e^{-i\hat{H}_{\omega_x}^{\mathcal{P}}t} | \Psi \rangle$. When $\epsilon(T_{\text{int}}) = \mathcal{O}(N^0)$, the uncertainty $\delta\omega_x$ scales as $\mathcal{O}(N^{-1})$ and the HL remains to be achieved.

Now, we can analytically show that $\epsilon(T_{\text{int}}) = \mathcal{O}(N^0)$ from the following inequality (see Appendix 3.C for the derivation):

$$|\epsilon(T_{\text{int}})| \leq \frac{2N\omega_x}{J_g} + 2(e^{N\omega_x/J_g} - 1) N\omega_x T_{\text{int}}, \quad (3.10)$$

where $J_g = \min_i \left[4\bar{J} - \sum_{j \in \langle i, j \rangle} |2\Delta J_{ij}| \right] \geq 4(1 - k)\bar{J} > 0$ is evaluated from the minimum energy change associated with flipping of ancillary spins (remember the assumption $\max_{i,j} 2|\Delta J_{ij}|/\bar{J} = k < 1$). Since $N\omega_x T_{\text{int}} = \mathcal{O}(N^0) \ll 1$ and $T_{\text{int}} = \mathcal{O}(N^0)$ are assumed here as a typical setting in Ramsey-type sensing with GHZ states, we have $\epsilon(t) = \mathcal{O}(N^0)$. Furthermore, the deviation becomes $|\epsilon(T_{\text{int}})| \ll 1$ for $N\omega_x \ll J_g$, which shows that strong interaction is beneficial. We note that the bound in Eq. (3.10) is derived by generalizing the error bound discussed in Refs. [161, 160, 209]. Equation (3.10) also shows that the effective description of the dynamics in the subspace becomes valid for the intermediate timescale for a weak target transverse field. That is, our sensing scheme exploits the HSF that emerges in a prethermal regime [158, 77] before evolving into the final equilibrium.

3.4 Discussion

Our scheme leads to better sensitivity for stronger interactions, in stark contrast to conventional methods as summarized in Fig. 3.2 (b). Importantly, our scheme is robust against the inhomogeneity of the interaction. The mechanism of the approximate freezing is also applicable for finite-range farther-neighbor interactions, cubic or triangular lattices, as well as the additional presence of weak longitudinal fields. This is due to the broad applicability of the mechanism of the suppression of spin flips under a weak transverse field and strong Ising interactions. Therefore, our HSF-protected sensing scheme can be generalized for these situations.

Finally, we describe a possible procedure for creating the entangled state $|\text{GHZ}_x^{\mathcal{P}}\rangle \otimes |F^{\mathcal{A}}\rangle$ as follows. We first prepare the GHZ state $|\text{GHZ}_x\rangle$ using the entire spins. by, e.g., adiabatically transforming a trivial state into the state $|\text{GHZ}_z\rangle$ as suggested in Refs. [130, 132, 210] and then rotating every spin by the angle $\pi/2$. Note that the state $|\text{GHZ}_z\rangle$ corresponds to a superposition of the two ground states of the system Hamiltonian \hat{H}_{int} in the ferromagnetic case. Then we obtain our desired state after performing the projection $\hat{P}_{\Psi} = I^{\mathcal{P}} \otimes |F^{\mathcal{A}}\rangle\langle F^{\mathcal{A}}|$ to $|\text{GHZ}_x\rangle$, which is equivalent to measurement feedback control on the ancillary spins; we measure the ancillary spins in the z basis and then apply single-spin rotations in the direction that depends on the measurement results.

3.5 Conclusion

In this Chapter, we have proposed a quantum sensing scheme for a system with spatially non-uniform always-on Ising interactions. Specifically, we show that we can robustly perform entanglement-enhanced sensing by designing a tailored state that evades thermalization due to the emergent Hilbert-space fragmentation (HSF). In this state, the entangled probe spins are decoupled from the rest of the system. This decoupling is due to a kinetic constraint that approximately emerges in the prethermal regime for strong Ising couplings and allows us to measure a transverse field stably. Our scheme establishes a novel approach to realize quantum sensing in a quantum many-body system with spatial inhomogeneity by using no dynamical controls. It is rigidly applicable even when the lattice shape and spatial dimensions are altered as long as the HSF structure offers us a way to control coherent dynamics without thermalization.

Here, we have introduced a concept of designing quantum states that avoid many-body thermalization by the HSF. Beyond quantum metrology, this HSF-protected manipulation of quantum dynamics would be advantageous for other quantum technologies as well, for which retaining entanglement in the presence of interactions is crucial. Finally, it is worth mentioning that although we assumed perfect state preparation in this chapter, preparation of the macroscopically entangled state is still another challenge in quantum metrology, especially under the presence of always-on interactions. In the next chapter, we will discuss an approach that addresses this problem in a slightly simpler setting, assuming again that the Ising interactions are always present among the probe qubits.

3.A Appendix: Derivation of the Zeno scaling

We discuss a way to obtain the sensitivity better than the standard quantum limit (SQL) in our system just by controlling the interaction time T_{int} , which turns out to be below the Heisenberg limit (HL). Specifically, we show that by sufficiently shortening T_{int} , we can suppress the effect of the residual interaction \hat{H}_{int} and obtain the Zeno scaling $\delta\omega_x \propto N^{-3/4}$ [207, 208, 198]. Although this scaling of $N^{-3/4}$ is worse than the HL, it is better than the SQL. We consider preparing a state $|\text{GHZ}_x\rangle$ and let it evolve for time T_{int} according to \hat{H} in [Eq. (3.1)]. Assuming that T_{int} is sufficiently small and that the perturbation series converge, the expectation value of the projective measurement \hat{P}_s in this case is evaluated up to the second order in the form

$$P_s = \frac{1}{2} + \frac{1}{2}\omega_x N T_{\text{int}} - \frac{1}{2}T_{\text{int}}^2 \sum_{\langle i,j \rangle} J_{ij}^2 + \mathcal{O}(T_{\text{int}}^3). \quad (3.A.11)$$

Note that we can make the approximation $\frac{1}{2} \sum_{\langle i,j \rangle} J_{ij}^2 \sim \bar{J}^2 N$ for simplicity. The expression (3.A.11) shows that the expectation value of the measurement outcomes is affected by the presence of the interaction term \hat{H}_{int} . On the one hand, as this additional term due to the interaction increases quadratically in time T_{int} , the standard deviation $\sqrt{P_s(1-P_s)}$ increases for large T_{int} , which contributes to the deterioration of the sensitivity. On the other hand, as we increase the interaction time, $|\partial P_s / \partial \omega_x|$ becomes large, which contributes to the enhancement of the sensitivity. These suggest that there is an optimal interaction time T_{int} for the sensitivity $\delta\omega_x$.

Now we evaluate the optimal sensitivity by shortening the interaction time T_{int} . Let us take $T_{\text{int}} = \tau N^{-1/2-\beta} \bar{J}^{-1-\gamma}$, where τ , β and γ are constants with $\tau \ll 1$. First, we can see that if either β or γ were negative, the second-order term in Eq. (3.A.11) would diverge as we take either $N \rightarrow \infty$ or $\bar{J} \rightarrow \infty$. Therefore, we take $\beta, \gamma \geq 0$ below. To make the situation similar to

the main text, we again assume that $\omega_x = \mathcal{O}(N^{-1})$ and set $\omega_x = \omega_0 N^{-1}$, where ω_0 is a constant. Then we can evaluate the uncertainty using Eq. (3.4) and Eq. (3.A.11) as follows:

$$\delta\omega_x = \frac{2}{T_{\text{all}}^{1/2}} \left(\frac{1}{4} \tau^{-1} \bar{J}^{1-\gamma} N^{-3/2-\beta} - \frac{1}{4} \omega_0^2 \tau \bar{J}^{-1+\gamma} N^{-5/2+\beta} + \omega_0 \tau^2 \bar{J}^{2\gamma} N^{-2+2\beta} - \bar{J}^{1+3\gamma} \tau^3 N^{-3/2+3\beta} \right)^{1/2}. \quad (3.A.12)$$

For large N , this is minimized when we take $\beta = 0$. In this case, $\gamma = 0$ gives the optimal sensitivity. Noting that the first term in the parenthesis dominates in Eq. (3.A.12), we can estimate the optimal scaling of the uncertainty as

$$\delta\omega_x \simeq (\bar{J}/\tau T_{\text{all}})^{1/2} N^{-3/4} = \mathcal{O}(N^{-3/4}), \quad (3.A.13)$$

which demonstrates the Zeno scaling. Note that the uncertainty increases as \bar{J} becomes larger in this case. This is consistent with our observation in Sec. 3.2.2, which shows a faster decay of the dynamical fidelity for a larger \bar{J} in case of using the state $|\text{GHZ}_x\rangle$ as the initial state.

3.B Appendix: Derivation of the uncertainty Eq. (3.9)

We evaluate the uncertainty $\delta\omega_x$ by taking into account the deviation in the approximation Eq. (3.6) with finite ω_x/\bar{J} . For this purpose, let us remind that ω_x in our scheme is estimated from a sequence of measurement outcomes. Suppose that we obtain M outcomes by repeating the step (i)–(iii) using our scheme. Let us define $\{m_1, m_2, \dots, m_M\}$ with $m_j \in \{0, 1\}$ as the sequence of the measurement outcomes and $S_M = (1/M) \sum_{j=1}^M m_j$ as the average of m_j . We estimate the unknown parameter ω_x from S_M as follows. When M goes to infinity, the average S_M is given by the quantum expectation value of the measurement $\langle \hat{P}_s \rangle_{\text{actual}} := \langle \Psi | e^{i\hat{H}_{\text{total}} T_{\text{int}}} \hat{P}_s e^{-i\hat{H}_{\text{total}} T_{\text{int}}} | \Psi \rangle$. Although calculating the ω_x -dependence of $\langle \hat{P}_s \rangle_{\text{actual}}$ analytically is difficult in general, we made the approximation Eq. (3.6) in the main text, which can be recast to the following:

$$\langle \hat{P}_s \rangle_{\text{actual}} = (1/2) (1 + \sin(\alpha N \omega_x T_{\text{int}})) + \epsilon(T_{\text{int}}), \quad (3.B.14)$$

where $\epsilon(T_{\text{int}}) := \langle \hat{P}_s \rangle_{\text{actual}} - \langle \hat{P}_s \rangle_{\text{eff}}$ is the deviation in the approximation due to finite ω_x/\bar{J} and we substitute T_{int} for t in Eq. (3.6). As discussed in the main text, when $N\omega_x \ll \bar{J}$, $\epsilon(T_{\text{int}})$ becomes small. Assuming $N\omega_x \ll T_{\text{int}}^{-1}$ as well, we can approximate Eq. (3.B.14) as $\langle \hat{P}_s \rangle_{\text{actual}} \simeq (1/2) (1 + \alpha N \omega_x T_{\text{int}})$. Let us introduce $\omega_{xM}^{\text{est}} := (1/\alpha N T_{\text{int}})(2S_M - 1)$, where ω_{xM}^{est} denotes the estimated value of ω_x in our scheme. Importantly, in the limit of large M and \bar{J} , we obtain $\omega_x = \omega_{xM}^{\text{est}}$. On the other hand, ω_{xM}^{est} does not necessarily coincide with the actual ω_x when $\epsilon(t)$ or M is finite. Below we consider this case and evaluate the uncertainty. Assuming $N\omega_x T_{\text{int}} \ll 1$, we obtain $\omega_x \simeq \left(2\langle \hat{P}_s \rangle_{\text{actual}} - 1 - 2\epsilon(T_{\text{int}}) \right) / (\alpha N T_{\text{int}})$ from Eq. (3.B.14), and

then the uncertainty is calculated as [211, 212]

$$\delta\omega_x^2 := \langle (\omega_{x_M}^{est} - \omega_x)^2 \rangle_{\text{stat}} \quad (3.B.15)$$

$$= \left\langle \left(\frac{2S_M - 1}{\alpha N T_{\text{int}}} - \frac{2\langle \hat{P}_s \rangle_{\text{actual}} - 1 - 2\epsilon(T_{\text{int}})}{\alpha N T_{\text{int}}} \right)^2 \right\rangle_{\text{stat}} \quad (3.B.16)$$

$$= \frac{4}{\alpha^2 N^2 T_{\text{int}}^2} \left\langle \left(S_M - \langle \hat{P}_s \rangle_{\text{actual}} \right)^2 + \epsilon(T_{\text{int}})^2 \right\rangle_{\text{stat}} \quad (3.B.17)$$

$$= \frac{4}{\alpha^2 N^2 T_{\text{int}}^2} \left(\frac{\langle \hat{P}_s \rangle_{\text{actual}} (1 - \langle \hat{P}_s \rangle_{\text{actual}})}{M} + \epsilon(T_{\text{int}})^2 \right), \quad (3.B.18)$$

where $\langle \cdot \rangle_{\text{stat}}$ is the statistical average of the outcomes m_j . In the last line, we used $\langle m_j \rangle_{\text{stat}} = \langle \hat{P}_s \rangle_{\text{actual}}$ and $\langle m_i m_j \rangle_{\text{stat}} = 0$ for $i \neq j$ to derive

$$\left\langle \left(S_M - \langle \hat{P}_s \rangle_{\text{actual}} \right)^2 \right\rangle_{\text{stat}} = \left\langle \sum_i \sum_j \left(m_i - \langle \hat{P}_s \rangle_{\text{actual}} \right) \left(m_j - \langle \hat{P}_s \rangle_{\text{actual}} \right) \right\rangle_{\text{stat}} / M^2 \quad (3.B.19)$$

$$= \left\langle \left(1/M \right) \sum_i \left(m_i - \langle \hat{P}_s \rangle_{\text{actual}} \right)^2 \right\rangle_{\text{stat}} / M \quad (3.B.20)$$

$$= \langle \hat{P}_s \rangle_{\text{actual}} (1 - \langle \hat{P}_s \rangle_{\text{actual}}) / M. \quad (3.B.21)$$

This evaluation means that $\delta\omega_x$ consists of the statistical error coming from finite M and the systematic error coming from finite $\epsilon(T_{\text{int}})$.

3.C Appendix: Derivation of the error bound Eq. (3.10)

[Note: The key idea of the proof in this section is obtained by Dr. Ryusuke Hamazaki.]

Here we show how one can derive the upper bound given in Eq. (3.10). We introduce the following theorem, which is a generalized version of the bound in Ref. [160].

Theorem 3.C.1 (Universal error bound) Consider a Hamiltonian $\hat{H} = \hat{H}_0 + \hat{V}$ of a quantum system, where \hat{H}_0 is regarded as a non-perturbed part and \hat{V} is a small perturbation. Let \mathcal{H}_P be a certain energy eigenspace of \hat{H}_0 and write \hat{P} as the projection operator on \mathcal{H}_P . Suppose that another energy eigenspace \mathcal{H}_R ($\mathcal{H}_P \cap \mathcal{H}_R = \phi$) of the Hamiltonian \hat{H}_0 satisfies the following [see Fig. 3.C.3]; (I) $\hat{P}\hat{V}(1 - \hat{P}) + (1 - \hat{P})\hat{V}\hat{P} = \hat{P}\hat{V}\hat{R} + \hat{R}\hat{V}\hat{P}$, where \hat{R} is the projection onto the energy eigenspace \mathcal{H}_R ; (II) Energy spectra of \mathcal{H}_P and \mathcal{H}_R are separated by a finite energy gap $\Delta_{PR} > 0$, where $\Delta_{PR} := \min_{|E\rangle \in \mathcal{H}_P, |E'\rangle \in \mathcal{H}_R} |E - E'|$. Then, starting from an initial state belonging to \mathcal{H}_P , we have the following error bound between the original dynamics described by \hat{H} and effective dynamics by $\hat{H}_P = \hat{P}\hat{H}\hat{P}$:

$$\epsilon(t) := \left\| \hat{P} \left(e^{i\hat{H}t} \hat{O} e^{-i\hat{H}t} - e^{i\hat{H}_P t} \hat{O} e^{-i\hat{H}_P t} \right) \hat{P} \right\| \quad (3.C.22)$$

$$\leq \frac{4\|\hat{V}\|}{\Delta_{PR}} + 2 \left(e^{2\|\hat{V}\|/\Delta_{PR}} - 1 \right) \|\hat{V}\|t \quad (3.C.23)$$

for any \hat{O} with $\|\hat{O}\| = 1$, where $\|\cdot\|$ denotes the operator norm.

In contrast to the bounds in Refs. [161, 160], which rely on the energy gap between \mathcal{H}_P and the rest of the spectrum, our theorem does not require that the eigenspace \mathcal{H}_P is isolated in the energy spectrum of \hat{H}_0 ; see Fig. 3.C.3. This means that when \hat{V} and \hat{P} satisfy the conditions (I) and (II), $\epsilon(t)$ is still bounded by using the energy gap between \mathcal{H}_P and a part of the spectrum \mathcal{H}_R , which is connected from \mathcal{H}_P via \hat{V} . In fact, the upper bound in Ref. [160] corresponds to the special case in which $\hat{R} = 1 - \hat{P}$. In this section, we only give the outline of the proof while emphasizing the difference from Ref. [160] for brevity and we leave the full proof of the theorem to Appendix A.

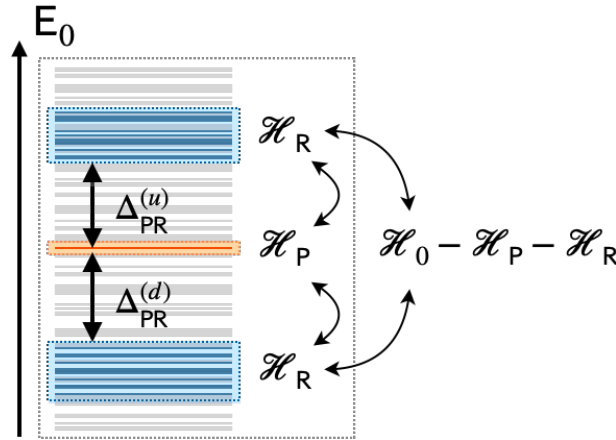


Figure 3.C.3: Energy spectrum of \hat{H}_0 . The energy eigenspace \mathcal{H}_P does not need to be isolated from the rest of the spectrum with an energy gap. Another eigenspace $\mathcal{H}_R \subseteq \mathcal{H}_0 \setminus \mathcal{H}_P$ is connected via \hat{V} from \mathcal{H}_P , where \mathcal{H}_0 denotes the total Hilbert space of \hat{H}_0 . We assume that \mathcal{H}_P and \mathcal{H}_R are separated by a finite energy gap $\Delta_{PR} \equiv \min\{\Delta_{PR}^{(u)}, \Delta_{PR}^{(d)}\}$. [Reproduced from Fig. S1 in Ref. [75].]

Our theorem can be derived just by following the proof in Ref. [160] with a slight modification. The proof is divided into two parts. In the first step, we derive

$$\epsilon(t) \leq 4\|\hat{T}\| + 2(e^{2\|\hat{T}\|} - 1)\|\hat{V}\|t. \quad (3.C.24)$$

Here, \hat{T} is an anti-Hermitian operator \hat{T} (i.e., $\hat{T}^\dagger = -\hat{T}$) that satisfies

$$[\hat{T}, \hat{H}_0] = -\hat{V}_{\text{off}} \quad (3.C.25)$$

with $\hat{V}_{\text{off}} := \hat{P}\hat{V}(1 - \hat{P}) + (1 - \hat{P})\hat{V}\hat{P}$. The derivation is obtained and explained in Section II-B in Ref. [160] (see especially Eqs. (23) and (30)). In the second step, which is different from Ref. [160], we derive an upper bound on $\|\hat{T}\|$ as follows:

$$\|\hat{T}\| = \|\bar{T}_{PR}\| \leq \frac{\|\bar{V}_{PR}\|}{\Delta_{PR}} \leq \frac{\|\hat{V}\|}{\Delta_{PR}}. \quad (3.C.26)$$

Here, the matrix \bar{T}_{PR} is the solution for the Sylvester equation

$$\bar{H}_{0P}\bar{T}_{PR} - \bar{T}_{PR}\bar{H}_{0R} = \bar{V}_{PR}, \quad (3.C.27)$$

where $\bar{V}_{\text{PR}} \equiv \hat{P}\hat{V}\hat{R}$, $\bar{T}_{\text{PR}} \equiv \hat{P}\hat{T}\hat{R}$, $\bar{H}_{0\text{P}} \equiv \hat{P}\hat{H}_0\hat{P}$, and $\bar{H}_{0\text{R}} \equiv \hat{R}\hat{H}_0\hat{R}$. Our observation here is that we can take a solution \hat{T} of Eq. (3.C.25) as $\hat{T} = \hat{P}\hat{T}\hat{R} + \hat{R}\hat{T}\hat{P}$ under the condition (I). In this case, Eq. (3.C.25) is reduced to Eq. (3.C.27), which is different from the one in Ref. [160]. Using the condition (II) on the spectra of $\bar{H}_{0\text{P}}$ and $\bar{H}_{0\text{R}}$, we can adopt known relations for the Sylvester equation [160, 213] to obtain $\|\bar{T}_{\text{PR}}\| \leq \|\bar{V}_{\text{PR}}\|/\Delta_{\text{PR}}$. [See also Eq. (29) in Ref. [160]]. In addition, using a similar argument given in Eq. (25) in Ref. [160], we arrive at Eq. (3.C.26).

Now, we explain how we adopt the theorem to our system. By taking $\hat{H}_0 = \hat{H}_{\text{total}} - \hat{H}_{\omega_x}$, $\hat{V} = \hat{H}_{\omega_x}$, and $\hat{P} = \hat{P}_{\Psi} = |\Psi\rangle\langle\Psi|$ (see Eqs. (3.7) and (3.8)) we have $\|\hat{V}\| = N\omega_x/2$, $\Delta_{\text{PR}} \geq \min_i \left[4\bar{J} - \sum_j |2\Delta J_{ij}| \right]$, and

$$\hat{H}_{\text{P}} = \hat{P}_{\Psi}\hat{H}_{\text{total}}\hat{P}_{\Psi} = (\hat{\mathbb{I}}^{\text{P}} \otimes |F^{\mathcal{A}}\rangle\langle F^{\mathcal{A}}|)\hat{H}_{\text{total}}(\hat{\mathbb{I}}^{\text{P}} \otimes |F^{\mathcal{A}}\rangle\langle F^{\mathcal{A}}|) \quad (3.C.28)$$

$$= \hat{H}_{\omega_x}^{\text{P}} \otimes |F^{\mathcal{A}}\rangle\langle F^{\mathcal{A}}|, \quad (3.C.29)$$

where $\hat{\mathbb{I}}^{\text{P}}$ denotes the identity operator on the probe spins. Below we explain how we evaluate Δ_{PR} . The eigenspace \mathcal{H}_{R} in this case, which is connected to \hat{P}_{Ψ} via the action of \hat{H}_{ω_x} , is formally expressed as $\mathcal{H}_{\text{R}} := \text{span}\{|\phi_{(k)}\rangle \otimes (\hat{\sigma}_i^x |F^{\mathcal{A}}\rangle) : |\phi_{(k)}\rangle (k = 1, 2, \dots, 2^{\alpha N}) \text{ are eigenstates of probe spins; } i \text{ is any site on ancillary spins}\}$. In other words, \mathcal{H}_{R} is spanned by computational basis states whose configuration includes the same configuration as $|F^{\mathcal{A}}\rangle$ except for any but one ancillary spin whose state is flipped from $|F^{\mathcal{A}}\rangle$. Then the energy gap between \mathcal{H}_{P} and \mathcal{H}_{R} is obtained by finding the minimum energy difference in $\hat{H}_{\text{total}} - \hat{H}_{\omega_x}$ caused by flipping one ancillary spin in $|F^{\mathcal{A}}\rangle$. Using the condition that every ancillary spin in $|F^{\mathcal{A}}\rangle$ is surrounded by at least three neighboring spins in the down states, we can evaluate Δ_{PR} as $\Delta_{\text{PR}} \geq J_g := \min_i \left[4\bar{J} - \sum_{j \in \langle i, j \rangle} |2\Delta J_{ij}| \right]$. Note that J_g is always positive since we assume that the spatial fluctuations of the interaction are relatively weak such that $|\Delta J_{ij}| < \bar{J}/2$.

Chapter 4

Entanglement-enhanced sensing with the one-dimensional Ising model using quantum domino dynamics

In this Chapter, we propose another entanglement-enhanced sensing scheme using a dynamical property of the quantum Ising model. We again consider using the Ising model as the probe system. In contrast to the scheme in the previous Chapter, in which we focused on the interrogation step in the Ramsey sensing scheme and assumed the target field to be a weak transverse field, in this Chapter we mainly focus on the other steps in the sensing scheme, namely the state preparation and readout, and assume the target field to be a weak longitudinal field. In particular, we consider making use of the so-called quantum domino dynamics for quantum sensing that arises in the Ising chain with a weak transverse field. In addition, here we perform a numerical calculation taking into account the effect of environmental noise.

This Chapter is organized as follows. First, we give introduction for this Chapter, starting again from a broad perspective. In Sec. 4.2, we review the Ramsey sensing scheme while introducing the notation that we specifically use in this Chapter, with particular attention to the use of entangling gates for state preparation and readout. We also review the quantum domino dynamics, which plays a key role in our scheme. In Sec. 4.3, we illustrate our scheme in an analytical way and compare it with the conventional scheme, and then numerically calculate the uncertainty of the estimation of the target field in the absence of environmental noise. In Sec. 4.4, we take into account the effect of dephasing as a realistic environmental noise and numerically investigate the performance of our scheme in the presence of noise. After discussing a possible approach to applying our scheme for a large system in Sec. 4.5, we summarize this Chapter in Sec. 4.6.

4.1 Introduction

The improvement of the sensitivity is a key objective for sensing technologies. Recent developments have enabled us to perform high precision sensing in a variety of areas, such as in life science [214, 4], investigation of semiconductor devices [215], and study of the condensed matter physics [216]. In particular, the detection of a weak magnetic field with the use of quantum technologies has been attracting great attentions.

Quantum metrology using spins (qubits) [217, 188, 194, 46] is an essential technique to

improve the estimation precision. Typical sensing scheme consists of the three procedures: preparing the probe spins in a specific quantum state, exposing the state to the target magnetic field, and performing a measurement for the readout. It is well known that the standard quantum limit (SQL) bounds the sensitivities when we prepare separable states for the probe spins [188]. On the other hand, by exploiting quantum properties of entanglement among the probe spins, the bound can be upgraded to the Heisenberg limit (HL) [218, 42, 194].

The challenge of the entanglement-enhanced sensing is to develop a practical method of preparing useful entangled states between the probe spins. For the entanglement-enhanced sensing of a magnetic field, we need both a strong coupling with the target magnetic field and controllability of the spins. The former is essential to achieve a better sensitivity, while the latter is crucial for the creation of the entangled states. However, as the coupling with the target magnetic field is increased, decoherence rate of the spin due to the unavoidable coupling with the environment typically increases, resulting in poor controllability of the spin. This means that it is difficult to accurately control the spins for the magnetic field sensing. Because of this difficulty, although a great number of methods requiring high controllability have been proposed, practical entanglement-enhanced sensing is still challenging in this area.

One of the typical entangled states for quantum metrology is the Greenberger-Horne-Zeilinger (GHZ) state [125, 206]. The GHZ state can be created by using a sequence of gate operations [219, 195, 220, 221, 128, 222, 129]. However, entangling gate operations including controlled-NOT (CNOT) gates require an accurate control of the interaction between spins. Such a requirement of the high controllability could be a bottleneck for the practical entanglement enhanced sensing.

In this Chapter, we propose an entanglement-enhanced sensing scheme to measure a magnetic field with an always-on nearest-neighbor interaction. Our scheme does not require either entangling gate operations or switching on/off the interaction among spins. More specifically, we consider a one-dimensional spin chain with a nearest-neighbor ferromagnetic Ising interaction accompanied by the homogeneous transverse magnetic field for control. In our scheme, performing a single-spin measurement on one of the edges of the chain at equilibrium induces unitary dynamics due to the intrinsic Hamiltonian of the system, which generates an entangled state suitable for quantum metrology. When we expose our probe spins to the target magnetic field, the interaction is still on; we just need to turn on/off global magnetic fields. Furthermore, the readout for the estimation of the target magnetic field can be implemented with a single spin measurement on the edge of the chain. Complicated operations, such as turning on/off the interactions are not required in our scheme, which is in stark contrast to the conventional scheme with GHZ states that requires precise control of the interaction.

4.2 Setting

In this section, we review ideas of quantum sensing and quantum domino dynamics, which we use in our sensing scheme.

4.2.1 Ramsey measurement scheme with separable states

For completeness, we start by briefly reviewing the Ramsey measurement scheme using L separable spins [46]. Our target magnetic field in this Chapter is a longitudinal field, whose Hamil-

tonian is described by

$$\hat{H}_{\omega_z} = \frac{\omega_z}{2} \sum_{n=1}^L \hat{\sigma}_n^z, \quad (4.1)$$

where ω_z denotes the strength of the static and homogeneous target magnetic field and n denotes the sites of the probe spins. The sensing scheme is summarized as follows. First, we prepare a separable probe state $\bigotimes_{n=1}^L |+\rangle_n$, where $|+\rangle_n$ denotes the eigenstate of $\hat{\sigma}_n^x$ with the eigenvalue $+1$. Here, $\hat{\sigma}_n^\nu$, $\nu \in \{x, y, z\}$ denotes the Pauli spin operators on site n . Second, we let the state interact with the target field for time T_{int} . Third, we perform a projective measurement $\hat{P}_{n,y}^+ = (\hat{\sigma}_n^y + 1)/2$ on each spin. After repeating these three steps, we estimate ω_z from the distribution of the outcomes.

The uncertainty of the estimated value of ω_z for each spin is commonly obtained as

$$\delta\omega_z = \frac{\sqrt{P(1-P)}}{\left| \frac{\partial P}{\partial \omega_z} \right| \sqrt{M}}, \quad (4.2)$$

where $P = (1 + \sin \omega_z T_{\text{int}})/2$ denotes the expectation value of $\hat{P}_{n,y}^+$ and M denotes the number of experimental repetition [46, 212]. For a total available time T_{all} , the number M is calculated as $M = T_{\text{all}}/T_{\text{sensing}}$, where T_{sensing} denotes a combined time of the three procedures of a sensing scheme, i.e., $T_{\text{sensing}} := T_{\text{reset}} + T_{\text{prep}} + T_{\text{int}} + T_{\text{read}}$. Here, T_{reset} denotes the time it takes to initialize the probe system, T_{prep} denotes the time it takes to generate a metrologically useful state from this initial state, and T_{read} denotes the time to readout the phase information acquired in the quantum state during the exposure to the magnetic field. In this section, we assume that the interaction time T_{int} accounts for a large fraction of the sensing time, i.e., $T_{\text{sensing}} \simeq T_{\text{int}}$. Then, the uncertainty of the estimation of ω_z using L separable spins is calculated as $\delta\omega_z = (LT_{\text{all}}T_{\text{int}})^{-1/2}$, which shows the SQL. The scaling of $\delta\omega_z$ can be improved to L^{-1} if we appropriately exploit an entanglement among the spins as we describe below.

4.2.2 Quantum sensing with the GHZ state

Next, we illustrate a quantum sensing scheme with the GHZ state using entangling gates. For the sake of the notation, we define a CNOT gate between spins on site n and site $n+1$ as

$$\text{CNOT}_{n,n+1} := [1 - \hat{\sigma}_n^z + (1 + \hat{\sigma}_n^z)\hat{\sigma}_{n+1}^x]/2. \quad (4.3)$$

In Fig. 4.1, we show a schematic picture of the conventional scheme which we describe below. A typical scheme to generate the GHZ state by gate operations is summarized as follows [46]. (i) We prepare an L -spin state $\bigotimes_{n=1}^L |0\rangle_n$, where $|0\rangle_n$ and $|1\rangle_n$ denote the eigenstate of $\hat{\sigma}_n^z$ with the eigenvalue -1 and $+1$, respectively. (ii) We implement a Hadamard gate on the first spin and perform a sequence of CNOT gates between adjacent spins in order to create the GHZ state $|\psi\rangle$, i.e.,

$$|\psi\rangle = \frac{1}{\sqrt{2}} \left(\bigotimes_{n=1}^L |0\rangle_n + \bigotimes_{n=1}^L |1\rangle_n \right). \quad (4.4)$$

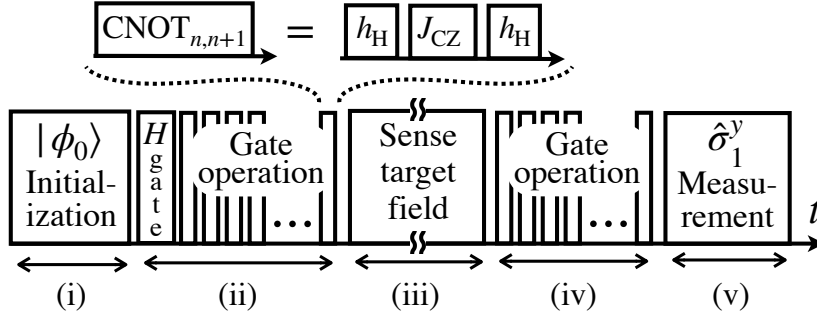


Figure 4.1: Schematic picture of required operations in the conventional scheme (i)–(v). The initial state $|\phi_0\rangle$ in the picture is $|\phi_0\rangle := \otimes_{n=1}^L |0\rangle_n$. We assume that the system has nearest-neighbor Ising interactions and gate operations consist of a sequence of CNOT gates, which can be expressed as in Eq. (4.11). [Reproduced and modified from Fig. 1 in Ref. [76].]

Here, the gates of $\text{CNOT}_{1,2}$, $\text{CNOT}_{2,3}$, \dots , and $\text{CNOT}_{L-1,L}$ are performed in sequence. (iii) We expose the state to the target magnetic field (4.1) for time T_{int} and obtain the state with a phase shift, i.e.,

$$|\psi(T_{\text{int}})\rangle = \frac{e^{i\omega_z L T_{\text{int}}/2}}{\sqrt{2}} \left(\bigotimes_{n=1}^L |0\rangle_n + e^{-i\omega_z L T_{\text{int}}} \bigotimes_{n=1}^L |1\rangle_n \right). \quad (4.5)$$

(iv) implement a sequence of CNOT gates again on the spins and obtain a disentangled state

$$|\psi'(T_{\text{int}})\rangle = \frac{e^{iL\omega_z T_{\text{int}}/2}}{\sqrt{2}} (|0\rangle_1 + e^{-iL\omega_z T_{\text{int}}} |1\rangle_1) \otimes \bigotimes_{n=2}^L |0\rangle_n. \quad (4.6)$$

Here, the CNOT gates are performed in the reverse order compared with the case in the step (ii). More specifically, the gates of $\text{CNOT}_{L-1,L}$, $\text{CNOT}_{L-2,L-1}$, \dots , and $\text{CNOT}_{1,2}$ are performed in sequence. (v) We measure the first spin in the $\hat{\sigma}_1^y$ basis and obtain an outcome of either $+1$ or -1 . The combination of the steps (iv) and (v) effectively measures the probability of projecting $|\psi(T_{\text{int}})\rangle$ in Eq. (4.5) to $(\bigotimes_{n=1}^L |0\rangle_n + i \bigotimes_{n=1}^L |1\rangle_n) / \sqrt{2}$.

By repeating these steps, we generate a histogram of the outcomes, which let us estimate the value of ω_z . The probability of obtaining the outcome of $+1$ in the $\hat{\sigma}_1^y$ basis is then calculated as

$$P = \langle \psi'(T_{\text{int}}) | \hat{P}_{1,y}^+ | \psi'(T_{\text{int}}) \rangle \quad (4.7)$$

$$= \frac{1}{2} + \frac{1}{2} \sin L\omega_z T_{\text{int}}. \quad (4.8)$$

Using Eq. (4.2), the uncertainty of the estimated value of ω_z is now obtained as $\delta\omega_z = L^{-1} (T_{\text{int}} T_{\text{all}})^{-1/2}$. This is the HL, which is $L^{-1/2}$ times smaller than the SQL.

Evaluation of the time for state preparation using the entangling gates

Let us estimate here the required time for the GHZ state generation when we use gate operations. To implement a gate of $\text{CNOT}_{n,n+1}$ to spins in a system with nearest-neighbor Ising interactions and magnetic fields, we can use Hadamard gates and a CZ (CPHASE) gate. These correspond

to the unitary dynamics induced by Hamiltonians of

$$\hat{H}_H^{(n)} := h_H(\hat{\sigma}_n^x + \hat{\sigma}_n^z)/\sqrt{2} \quad (4.9)$$

and

$$\hat{H}_{CZ}^{(n,n+1)} := \frac{J_{CZ}}{4} [1 - \hat{\sigma}_n^z + (1 + \hat{\sigma}_n^z)\hat{\sigma}_{n+1}^z], \quad (4.10)$$

where h_H denotes the strength of the magnetic field and J_{CZ} denotes the interaction strength. More specifically, the CNOT gate can be described as

$$\text{CNOT}_{n,n+1} = \exp\left(i\frac{\pi}{2h_H}\hat{H}_H^{(n+1)}\right) \exp\left(i\frac{\pi}{J_{CZ}}\hat{H}_{CZ}^{(n,n+1)}\right) \exp\left(i\frac{\pi}{2h_H}\hat{H}_H^{(n+1)}\right). \quad (4.11)$$

Hence, the necessary time is evaluated as $\pi/h_H + \pi/J_{CZ}$.

4.2.3 Transverse-field Ising chain

Next, we introduce the transverse-field Ising chain [223, 224]. The Hamiltonian is described as follows:

$$\hat{H}_{\text{TFIM}} = \hat{H}_{\text{Ising}} + \hat{H}_x, \quad (4.12)$$

$$\hat{H}_{\text{Ising}} = -\frac{J}{4} \sum_{n=1}^{L-1} \hat{\sigma}_n^z \hat{\sigma}_{n+1}^z, \quad (4.13)$$

$$\hat{H}_x = \frac{h_x}{2} \sum_{n=1}^L \hat{\sigma}_n^x, \quad (4.14)$$

where $J > 0$ denotes the strength of the ferromagnetic interaction and h_x denotes the magnitude of the transverse magnetic field. Without loss of generality, we assume $h_x > 0$. The model exhibits a quantum phase transition at $h_x/J = 1/2$ at the zero temperature in the thermodynamic limit and shows a ferromagnetic order in the z direction for $h_x/J < 1/2$. For a finite L and $h_x/J < 1/2$, the system has two almost degenerate ground states with an exponentially small energy difference. More specifically, the ground state and the first excited state can be approximated as $\left(\bigotimes_{n=1}^L |0\rangle_n \pm \bigotimes_{n=1}^L |1\rangle_n\right)/\sqrt{2}$. with the energy difference which is exponentially small in L [225]. The excited states are separated from them by a finite energy gap $\sim J/2 - h_x$.

Throughout this Chapter, we assume that we use thermal equilibrium states as the initial states unless specifically mentioned. For a finite system at equilibrium with an inverse temperature β , the thermal equilibrium state $\hat{\rho}_\beta := e^{-\beta\hat{H}_{\text{TFIM}}}/\text{Tr}[e^{-\beta\hat{H}_{\text{TFIM}}}]$ can be well approximated by the mixed state

$$\hat{\rho}_\beta \simeq \hat{\rho}_{\text{mix}} := \frac{1}{2} \left(\bigotimes_{n=1}^L |0\rangle_n \right) \left(\bigotimes_{n=1}^L \langle 0|_n \right) + \frac{1}{2} \left(\bigotimes_{n=1}^L |1\rangle_n \right) \left(\bigotimes_{n=1}^L \langle 1|_n \right) \quad (4.15)$$

for $h_x/J \ll 1/2$ and $1/\beta \ll J/2 - h_x$. More specifically, we should decrease $1/\beta$ as we increase L because the probability of having the ground states in $\hat{\rho}_\beta$ becomes extremely small for a large L . In Sec. 4.3, we will assume that the temperature is sufficiently low in our scheme so that the

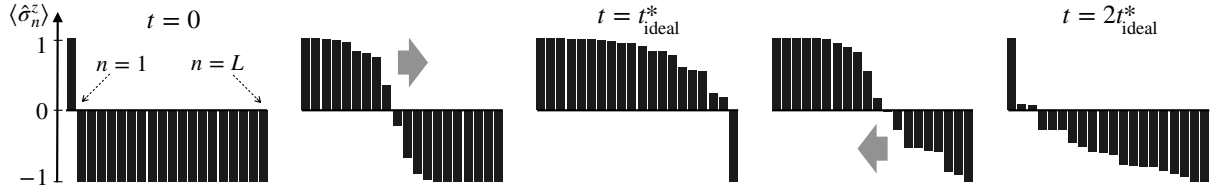


Figure 4.2: Quantum domino dynamics induced by the Hamiltonian (4.20) with the initial state $|1\rangle_1 \otimes \bigotimes_{n=2}^L |0\rangle_n$. Black bars show the magnetization at each site n at time steps of $t = 0, t_{\text{ideal}}^*/2, t_{\text{ideal}}^*, 3t_{\text{ideal}}^*/2, \text{ and } 2t_{\text{ideal}}^*$. We choose $L = 20$ and $h_x t_{\text{ideal}}^* = 1.05L$ here. [Reproduced and modified from Fig. 2 in Ref. [76].]

condition of $\hat{\rho}_\beta \sim \hat{\rho}_{\text{mix}}$ should be approximately valid. To illustrate how low the temperature should be for satisfying the condition $\hat{\rho}_\beta \sim \hat{\rho}_{\text{mix}}$, we calculate the fidelity $F = F(\hat{\rho}_\beta, \hat{\rho}_{\text{mix}}) = \text{Tr} \left[\left(\hat{\rho}_\beta^{1/2} \hat{\rho}_{\text{mix}} \hat{\rho}_\beta^{1/2} \right)^{1/2} \right]$ and obtain $F = 87\%$ for $\beta = 10, J = 1, h_x = 0.1$ and $L = 12$. We can prepare the thermal equilibrium state just by using the energy relaxation process from the environment, so that precise control is not required.

4.2.4 Quantum domino dynamics

Here, we review the concept of “quantum domino” dynamics in the transverse-field Ising chain, which was theoretically discussed in Refs. [137, 138, 139, 140] and demonstrated in Ref. [141]. It is observed when we prepare a state $|1\rangle_1 \otimes \bigotimes_{n=2}^L |0\rangle_n$ as the initial state and let the state evolve according to the Hamiltonian (4.12) with a weak transverse magnetic field; the spin-flip on the first site propagates, which induces a sequence of flipping across the system up to the $(L - 1)$ th spin.

In short, quantum domino dynamics can approximately realize the following transformation when we appropriately tune the evolution time:

$$\hat{U} \left(|1\rangle_1 \otimes \bigotimes_{n=2}^L |0\rangle_n \right) \simeq \left(\bigotimes_{n=1}^{L-1} |1\rangle_n \right) \otimes |0\rangle_L, \quad (4.16)$$

$$\hat{U} \left(|0\rangle_1 \otimes \bigotimes_{n=2}^L |1\rangle_n \right) \simeq \left(\bigotimes_{n=1}^{L-1} |0\rangle_n \right) \otimes |1\rangle_L, \quad (4.17)$$

where \hat{U} denotes the unitary dynamics due to the Hamiltonian (4.12). On the other hand, if all spins are initialized in the same direction, for instance $\bigotimes_{n=1}^L |0\rangle_n$, the system stays almost in the same state i.e., $\hat{U} \bigotimes_{n=1}^L |0\rangle_n \simeq \bigotimes_{n=1}^L |0\rangle_n$. Therefore, we can approximately generate the GHZ state of $(L - 1)$ spins if we induce the quantum domino dynamics with an initial state of $|+\rangle_1 \otimes \bigotimes_{n=2}^L |0\rangle_n$ [139].

Importantly, the quantum domino dynamics can also occur in the opposite direction, i.e.,

$$\hat{U} \left[\left(\bigotimes_{n=1}^{L-1} |1\rangle_n \right) \otimes |0\rangle_L \right] \simeq |1\rangle_1 \otimes \bigotimes_{n=2}^L |0\rangle_n, \quad (4.18)$$

$$\hat{U} \left[\left(\bigotimes_{n=1}^{L-1} |0\rangle_n \right) \otimes |1\rangle_L \right] \simeq |0\rangle_1 \otimes \bigotimes_{n=2}^L |1\rangle_n. \quad (4.19)$$

These equations now imply that the entangled state $\hat{U} \left(|+\rangle_1 \otimes \bigotimes_{n=2}^L |0\rangle_n \right)$ can go back to the initial state approximately by applying \hat{U} again. We will refer to the dynamics (4.18) and (4.19) as well as (4.16) and (4.17) as ideal domino dynamics.

The emergence of the quantum domino dynamics in the transverse-field Ising chain can be explained as follows. Regarding \hat{H}_x as a perturbative term, the Hamiltonian in the interaction picture is described as $e^{i\hat{H}_{\text{Ising}}t} \hat{H}_x e^{-i\hat{H}_{\text{Ising}}t}$. By using a secular approximation to ignore oscillating terms with high frequencies of J [137], we obtain the following Hamiltonian

$$\hat{H}_{\text{secular}} = \frac{h_x}{4} \sum_{n=2}^{L-1} \hat{\sigma}_n^x (1 - \hat{\sigma}_{n-1}^z \hat{\sigma}_{n+1}^z) \quad (4.20)$$

as the effective Hamiltonian in the interaction picture. (Note that this Hamiltonian is basically the same as the Hamiltonian Eq. (2.7) in Chapter 2 and allows for analytical calculations [137].) The Hamiltonian (4.20) shows that the spin flip on the site n by the operator $\hat{\sigma}_n^x$ occurs only when its two adjacent spins are in the opposite direction. Suppose that the spins at the sites $n = 1, 2, \dots, k$ are aligned up while the other spins are aligned down. In this case, only the k th and $(k+1)$ th spins could flip while the other spins remain in the original state. Therefore, a system which is initialized in the state $|1\rangle_1 \otimes \bigotimes_{n=2}^L |0\rangle_n$ exhibits a sequence of spin flips from the second to the $(L-1)$ th spins.

We show in Fig. 4.2 quantum domino dynamics induced by the Hamiltonian (4.20). Starting from the state $|1\rangle_1 \otimes \bigotimes_{n=2}^L |0\rangle_n$, the spin flip propagates forwardly until a time $t = t_{\text{ideal}}^*$, and then this propagates back for $t_{\text{ideal}}^* < t < 2t_{\text{ideal}}^*$, where t_{ideal}^* denotes the optimal time to maximize the total magnetization density of the time-evolved state due to the Hamiltonian (4.20).

Strictly speaking, there is still a small difference between the unitary dynamics induced by the Hamiltonian (4.20) and the ideal quantum domino dynamics (4.16)–(4.19). As the flipping propagates further, the difference between the ideal domino dynamics and the dynamics by the Hamiltonian (4.20) becomes larger as shown in Fig. 4.2. In the ideal domino dynamics, the total magnetization density, i.e., $M_z/L := (1/2L) \sum_{n=1}^L \langle \hat{\sigma}_n^z \rangle$, would be $M_z/L = 1/2 - 1/L$ for the right-hand side of Eq. (4.16). On the other hand, for the actual dynamics, it is not trivial whether the maximum total magnetization density converges to a finite value as we increase the system size L . Fortunately, it has been found that, when we prepare an initial state $|1\rangle_1 \otimes \bigotimes_{n=2}^L |0\rangle_n$ and let this state evolve by the Hamiltonian (4.20) for a certain time, we can obtain a finite magnetization density $M_z/L \sim 0.37$ for a large L [137]. The optimal time t_{ideal}^* is also numerically estimated as $t_{\text{ideal}}^* \sim 1.06L/h_x$ in Ref. [137]. We will estimate the appropriate time of the duration for the original Hamiltonian (4.12) with a finite L and h_x in Sec. 4.3.4.

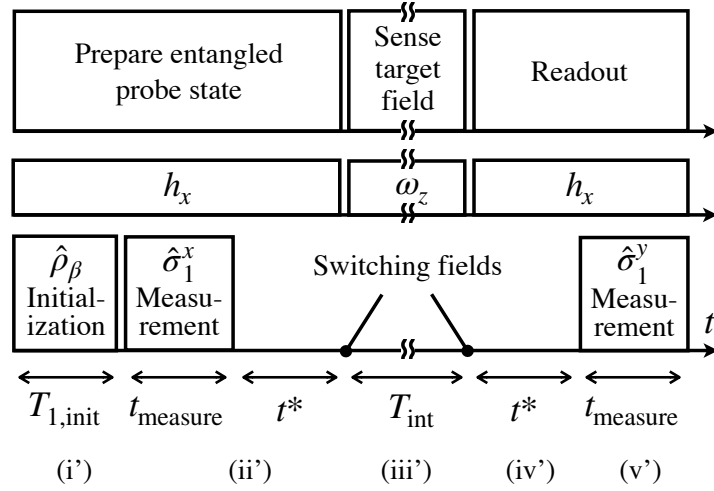


Figure 4.3: Schematic picture of our sensing scheme. The upper panel represents the prescription of our scheme. The middle panel shows how we apply global magnetic fields. The lower panel shows the procedure (i')–(v') and the time it takes for each step. During the interrogation step (iii'), we turn off the transverse magnetic field and expose the probe to the target magnetic field. We assume that the interaction time T_{int} is much longer than the other times involved. [Reproduced and modified from Fig. 3 in Ref. [76].]

4.3 Our quantum sensing scheme with always-on interaction

In this section, we present our sensing scheme with an always-on interaction between the nearest-neighbor spins in the probe chain. In the following scheme, the only necessary operations are to initialize the system, to perform projective measurements on the first spin, and to turn on/off global magnetic fields.

4.3.1 Description of our sensing scheme

Our scheme can be summarized as follows (see also Fig. 4.3): (i') we prepare a thermal equilibrium state of the Hamiltonian (4.12) with $h_x/J < 1/2$; (ii') we perform a projective measurement on the first spin along the x direction at $t = 0$ and then let the system evolve according to the same Hamiltonian (4.12) until $t = t^*$; (iii') we turn off the transverse magnetic field in Eq. (4.12) and instead let the system interact with the target magnetic field (4.1) for a time T_{int} ; (iv') we let the system evolve according to (4.12) again for the time t^* ; (v') we perform a projective measurement on the first spin in the $\hat{\sigma}_1^y$ basis. By repeating these steps, we generate the histogram of the outcomes.

The key idea of our scheme is the use of the quantum domino dynamics. Although the state is mainly described by the Schrödinger picture in this Chapter, we use the interaction picture $\hat{\rho}_I(t) = e^{itH_{\text{Ising}}}\hat{\rho}_S(t)e^{-itH_{\text{Ising}}}$ in this paragraph to avoid cumbersome expressions, i.e., the state $\hat{\rho}_S$ in the Schrödinger picture is obtained after considering the time evolution according to the Hamiltonian \hat{H}_{Ising} (see also Sec. 4.2.4). The state after the measurement in the step (ii') is

approximated as

$$\hat{\rho}_I(0) = |+\rangle_{11}\langle +| \otimes \left(\bigotimes_{n=2}^L |0\rangle_n \langle 0| + \bigotimes_{n=2}^L |1\rangle_n \langle 1| \right) / 2 \quad (4.21)$$

because of Eq. (4.15) for the case in which the measurement outcome is +1. This state evolves into

$$\hat{\rho}_I(t^*) = \frac{1}{2} \left(\bigotimes_{n=1}^{L-1} |0\rangle_n + \bigotimes_{n=1}^{L-1} |1\rangle_n \right) \left(\bigotimes_{n=1}^{L-1} \langle 0| + \bigotimes_{n=1}^{L-1} \langle 1| \right) \otimes \frac{1}{2} (|0\rangle_{LL} \langle 0| + |1\rangle_{LL} \langle 1|) \quad (4.22)$$

under the ideal domino dynamics (4.16) and (4.17), which is approximately induced by the Hamiltonian (4.12) in the step (ii'). After obtaining a phase shift at the third step (iii'), i.e.,

$$\begin{aligned} \hat{\rho}_I(t^* + T_{\text{int}}) &= \frac{1}{2} \left(\bigotimes_{n=1}^{L-1} |0\rangle_n + e^{-i\omega_z(L-1)T_{\text{int}}} \bigotimes_{n=1}^{L-1} |1\rangle_n \right) \left(\bigotimes_{n=1}^{L-1} \langle 0| + e^{i\omega_z(L-1)T_{\text{int}}} \bigotimes_{n=1}^{L-1} \langle 1| \right) \\ &\otimes \frac{1}{2} (|0\rangle_{LL} \langle 0| + |1\rangle_{LL} \langle 1|), \end{aligned} \quad (4.23)$$

the state evolves into

$$\begin{aligned} \hat{\rho}_I(2t^* + T_{\text{int}}) &= \frac{1}{2} (|0\rangle_1 + e^{-i\omega_z(L-1)T_{\text{int}}} |1\rangle_1) ({}_1\langle 0| + e^{i\omega_z(L-1)T_{\text{int}}} {}_1\langle 1|) \\ &\otimes \frac{1}{2} \left(\bigotimes_{n=2}^L |0\rangle_n \langle 0| + \bigotimes_{n=2}^L |1\rangle_{11} \langle 1| \right), \end{aligned} \quad (4.24)$$

in the step (iv'), which replaces the disentangling procedure (iv) in the conventional scheme in Sec. 4.2.2 by the time evolution with the Hamiltonian (4.12). In this case, the Hamiltonian (4.12) approximately induces the ideal domino dynamics (4.18) and (4.19). Here, the combination of the steps (iv') and (v') effectively measures the probability of projecting $(L - 1)$ -spin state of $\hat{\rho}_I(t^* + T_{\text{int}})$ in Eq. (4.23) to $\left(\bigotimes_{n=1}^{L-1} |0\rangle_n + i \bigotimes_{n=1}^{L-1} |1\rangle_n \right) / \sqrt{2}$.

For our scheme, T_{reset} , T_{prep} , and T_{read} are expressed as $T_{\text{reset}} = T_{1,\text{init}}$, $T_{\text{prep}} = t^* + t_{\text{measure}}$, and $T_{\text{read}} = t^* + t_{\text{measure}}$, where t_{measure} denotes the time required for the projective measurements and $T_{1,\text{init}}$ denotes the relaxation time of the system to thermalize, i.e., the time for the step (i'). In this Chapter, we assume that $T_{1,\text{init}}$ and t_{measure} are much shorter than t^* and T_{int} . In addition, for simplicity, we ignore the effect of dephasing in the sensing steps except for the step (iii') in this Chapter. In the noiseless case, we can in principle set T_{int} to be much longer than the other times that are required in the sensing steps. In general, the sensitivity increases as the interaction time T_{int} becomes comparable with the total time T_{all} in the noiseless case whereas in the presence of the environmental noise, making T_{int} close to the dephasing time T_2 results in better sensitivity.

We note that we need more careful consideration on the assumption $T_{\text{int}} \gg T_{\text{reset}}$ when we consider the experimental implementation in the presence of dephasing. Nevertheless, we assume that the time T_{reset} can be made much shorter than the dephasing time T_2 in experiments because of the following reason. For a long-lived spin, T_2 can be much longer than t^* and t_{readout} . However, in most of the solid-state systems, the energy relaxation time, which we denote $T_{1,\text{relax}}$, is even longer than the dephasing time T_2 [226, 227, 228, 229, 230, 231, 232], which may imply $T_{\text{reset}} > T_2 \sim T_{\text{int}}$. For example, nitrogen vacancies in diamond have an

energy relaxation time of $T_1 \simeq 45$ seconds [226], while the dephasing time is around $T_2 \simeq 2$ ms [233]. Fortunately, there are experimental techniques that temporarily decrease the energy relaxation time [234, 235, 236, 237]. We refer to such an artificial and short energy relaxation time as $T_{1,\text{init}}$. Here, we assume that such resetting techniques are available when our sensing scheme is implemented in experiments and thus take $T_{\text{int}} \gg T_{\text{reset}} = T_{1,\text{init}}$.

4.3.2 Analytical evaluation of the sensitivity

The probability P of obtaining $+1$ as the measurement outcome in the step (v') is written as

$$P = \text{Tr}[\hat{U}_{\text{scheme}} \hat{\rho}_0 \hat{U}_{\text{scheme}}^\dagger \hat{P}_{1,y}^+], \quad (4.25)$$

where

$$\hat{\rho}_0 := \frac{\hat{P}_{1,x}^+ \hat{\rho}_\beta \hat{P}_{1,x}^+}{\text{Tr}[\hat{P}_{1,x}^+ \hat{\rho}_\beta]}, \quad (4.26)$$

$$\hat{U}_{\text{scheme}} := e^{-i\hat{H}_{\text{TFIM}}t^*} e^{-i(\hat{H}_{\text{Ising}} + \hat{H}_{\omega_z})T_{\text{int}}} e^{-i\hat{H}_{\text{TFIM}}t^*}. \quad (4.27)$$

Hereafter, we assume that the measurement outcome in the step (i') is $+1$ without loss of generality. The projection $\hat{P}_{1,x}^+$ to the state in which we get the measurement outcome $+1$ at the step (i') denotes $\hat{P}_{1,x}^+ := (\hat{\sigma}_1^x + 1)/2$. For the case in which the outcome in the step (i') is -1 , we exchange the measurement basis in the step (v') from $\hat{\sigma}_1^y$ to $-\hat{\sigma}_1^y$.

Let us derive the sensitivity of our scheme by using some approximations. In Sec. 4.3.4, we will numerically calculate the sensitivity without approximations by directly calculating Eq. (4.25). Assuming the validity of the approximation (4.15) and the ideal domino dynamics (4.16)–(4.19), we can estimate the probability (4.25) as

$$P \simeq \frac{1}{2} + \frac{1}{2} \cos \left[J \left(t^* + \frac{T_{\text{int}}}{2} \right) \right] \sin [(L-1)\omega_z T_{\text{int}}]. \quad (4.28)$$

The oscillating part $\cos [J(t^* + T_{\text{int}}/2)]$ in Eq. (4.28), which did not appear in Eq. (4.8), represents the effect of the presence of the Ising interaction. By tuning t^* , the probability becomes the same as that with the GHZ state composed of $(L-1)$ spins; see Eq. (4.8). Therefore, we can achieve the HL in this case similarly to the case in Sec. 4.2.2.

Equation (4.28) also shows that the probability approaches to $1/2$ as ω_z goes to 0. Although we derived Eq. (4.28) with several approximations, we can derive this from a more general setup as follows. The Hamiltonian \hat{H}_{TFIM} and the measurement $\hat{P}_{1,x}^+$ as well as the initial state $\hat{\rho}_\beta$ commutes with the parity symmetry $\hat{U}_x := \prod_{n=1}^L \hat{\sigma}_n^x$, while $\hat{\sigma}_1^y$ in $\hat{P}_{1,y}^+$ anti-commutes with \hat{U}_x . From these relations and Eqs. (4.25)–(4.27), we find that the expectation value of $\hat{\sigma}_1^y = 2\hat{P}_{1,y}^+ - 1$ always vanishes for $\omega_z T_{\text{int}} = 0$. This shows that the deviation of the probability of the measurement outcomes from $1/2$ always signals the presence of non-vanishing ω_z .

We emphasize here that even though Eq. (4.28) is the result of an approximation, the effect of the presence of the Ising interaction at the interrogation step (iii') can always be canceled out by setting $T_{\text{int}} = m4\pi/J$, where m denotes a natural number. When the probe spins interact with the target field, they can be affected by an additional Hamiltonian, such as residual interactions between spins, as we have shown in the previous Chapter. The effect of such an additional Hamiltonian has been discussed in some studies. It was shown in Ref. [238] that when one

prepares an optimal state for sensing the target field in the presence of additional Hamiltonian, this term cannot enhance the sensitivity anymore compared to the case in which there is no such terms. Reference [239] considered estimation of the target longitudinal magnetic field in the transverse Ising chain, whose interaction is of XX type. By utilizing the integrability of the model in one dimension, it was shown that the sensitivity can still achieve the Heisenberg-limited scaling if an appropriate GHZ-type state is used. In contrast, the sensitivities with and without residual interactions are the same in our case in the present Chapter. Here, we take an advantage of the fact that the Ising interaction commutes with the target magnetic field and we can cancel out the additional phase shift by tuning the interaction time. We hence can obtain the HL if we could prepare and disentangle the GHZ state perfectly.

4.3.3 Comparison with the conventional scheme using entangling gates

Here, we summarize the difference between our scheme in Sec.4.3.1 and the conventional one introduced in Sec. 4.2.2.

First, there is a difference in state preparation. We use the time evolution according to the time-independent Hamiltonian (4.12) in preparing a metrologically useful state. Importantly, since we straightforwardly use the dynamics induced by the Hamiltonian for these processes, our scheme does not require any temporal control over the individual Ising interactions between spins. This is in stark contrast to the conventional scheme that uses gate operations for the entanglement generation, which typically requires turning on/off the interaction.

Second, the way to readout the state is different. We use the Hamiltonian dynamics to transform the entangled probe state into an almost separable state so that we can extract the information of the target magnetic field from the single spin measurement. On the other hand, in the conventional approach, a combination of gate operations and projective measurements is required.

Finally, we compare the time required for our scheme which uses the quantum domino dynamics and that for the conventional scheme which uses the gate operations. When a system has Ising interactions with strength of J_{CZ} , the operation time for implementing one CNOT gate is $(\pi/J_{CZ} + 2\tau_H)$ from our estimation in Sec. 4.2.2, where τ_H denotes a necessary gate time to implement the Hadamard gate. On the other hand, it takes about $1.06/h_x$ for flipping single spin on average in the domino dynamics. In Sec. 4.3.4 and 4.4 we demonstrate that our scheme beats the SQL by a constant factor, where we set $J = 1$ and $h_x = 0.1$. This shows that even if we ignore the operation time for the Hadamard gates, the preparation time for the case of using the quantum domino dynamics is only around three times longer than that for the case of using a sequence of CNOT gates, under the assumption that the Ising interaction strength is the same, i.e., $J_{CZ} = J$. As long as the coherence time is long, it is more advantageous to use quantum domino dynamics than gate type operations. Therefore, our scheme can be a practical way to realize entanglement-enhanced sensing in a spin system with fixed Ising interaction.

4.3.4 Numerical results for the case without environmental noise

We now present numerical results to show the performance of our scheme without noise. We calculate the uncertainty of the estimated value of ω_z using Eqs. (4.25)–(4.27). We here take the interaction strength and the transverse magnetic field to be $J = 1$ and $h_x = 0.1$.

For each size L , we numerically find the optimal preparation time t_{opt}^* in order to obtain the

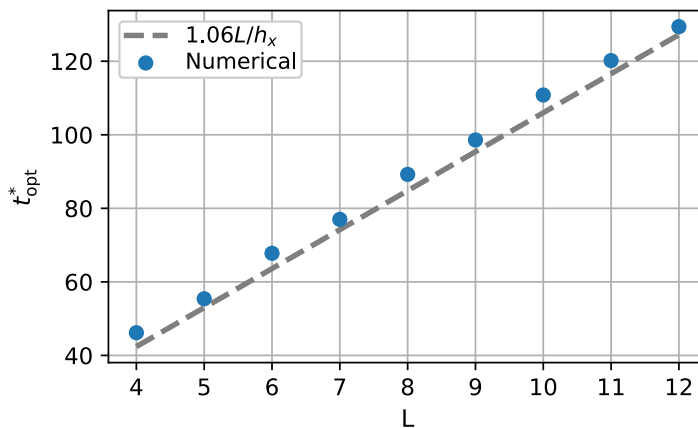


Figure 4.4: The optimal preparation time t_{opt}^* which we use in the step (ii') and the step (iv') when we numerically simulate our scheme. The blue points show t^* at which $\delta\omega_z$ can be minimized for $h_x = 0.1$ and $\beta = 10$. The broken line shows the scaling function $t_{\text{opt}}^* = 1.06L/h_x$. All parameters are normalized by $J = 1$. [Reproduced from Fig. 4 in Ref. [76].]

smallest uncertainty $\delta\omega_z$. In Fig. 4.4, we show the size dependence of t_{opt}^* , which takes the value around $t_{\text{opt}}^* \sim 1.06L/h_x \simeq t_{\text{ideal}}^*$ as we mentioned in Sec. 4.2.4. Throughout the Chapter, we use these values of t_{opt}^* as t^* when we plot $\delta\omega_z$ and T_{int} for each L . We have numerically checked that t_{opt}^* does not depend on β in the parameter sets which we use in this Chapter. In order to take into account the effect of the preparation time on the uncertainty, we take $T_{\text{sensing}} = T_{\text{int}} + 2t_{\text{opt}}^*$, although T_{int} is much longer than t_{opt}^* in the following calculations. We ignore the other times involved for simplicity.

In Fig. 4.5 (a), we observe an oscillation in the preparation time t^* with the probability (4.25) as we have discussed in Eq. (4.28). The oscillation frequency is almost the same as $J = 1$, which is consistent with our approximate analytical expression (4.28). The optimal time t_{opt}^* which provides the smallest uncertainty $\delta\omega_z$ corresponds to the minimal point of the oscillation.

Figure 4.5 (b) shows the uncertainty against the number of the spins with different initial states. These results demonstrate that our scheme achieves the high precision sensing beyond the SQL by a constant factor. However, when we increase L with a fixed β , the uncertainty starts to saturate, as a tendency of which can be observed in the plot for $\beta = 5$ in Fig. 4.5 (b). This is due mainly to the breakdown of the approximation (4.15), which requires β to be large. We will discuss this point again in Sec. 4.5.

In the conventional quantum domino dynamics the initial state is assumed to be pure, namely $\bigotimes_{n=1}^L |0\rangle_n$. For comparison, we calculate the uncertainty when the initial state is the same state $\bigotimes_{n=1}^L |0\rangle_n$. Interestingly, the uncertainty with this pure initial state is almost the same as that with the thermal equilibrium states $\hat{\rho}_\beta$ with $\beta = 10$ and 20 , as shown in Fig. 4.5 (b). Therefore, the use of the thermal states does not necessarily degrade the sensitivity compared with the case of using a pure state.

4.4 Quantum Sensing under time-inhomogeneous dephasing

In this section, we consider the effect of dephasing during the interrogation step (iii') and show that our scheme beats the SQL by a constant factor even in the presence of the dephasing noise.

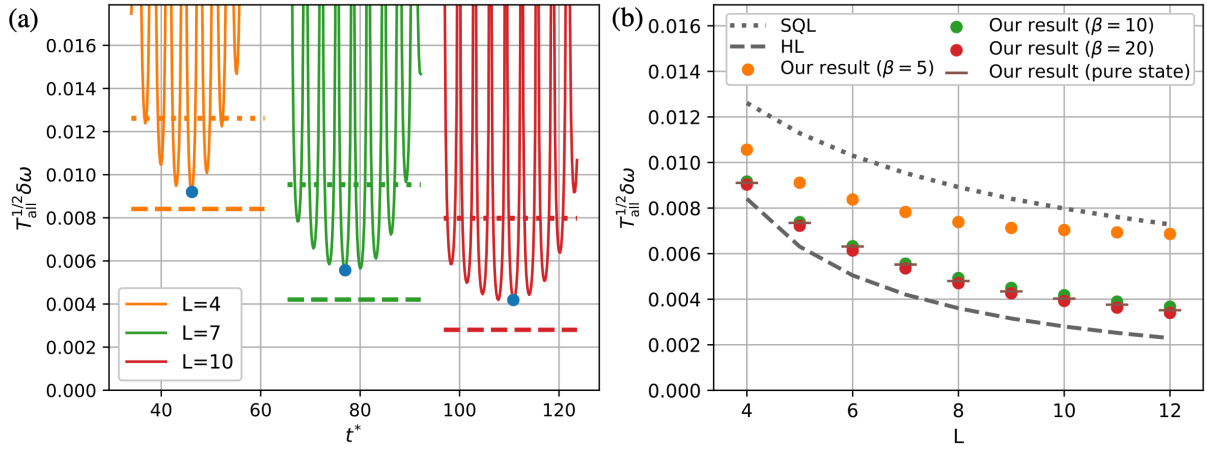


Figure 4.5: (a) The oscillation of $\delta\omega_z$ in the preparation time t^* . Three blue points show the minimum of $T_{\text{all}}^{1/2} \delta\omega_z$ at t_{opt}^* for each size L with $L = 4, 7$, and 10 . The dotted line and the broken line show the uncertainty of the SQL for L spins and the HL for $(L - 1)$ spins, respectively. (b) Size dependence of the uncertainty $\delta\omega_z$ in our scheme. The dotted line and the broken line show the SQL for L -spins and the HL for $(L - 1)$ spins, respectively. The other symbols in the figure show $\delta\omega_z$ for the cases in which the initial states are $\hat{\rho}_\beta$ with $\beta = 5, 10$, and 20 , and $\bigotimes_{n=1}^L |0\rangle_n$, respectively. In both (a) and (b), we take the parameters as $h_x = 0.1$, $\omega_z = 10^{-6}$, and $T_{\text{int}} = 500\pi$. All parameters are normalized by $J = 1$. [Reproduced from Figs. 5 and 6 in Ref. [76].]

To this end, we consider shortening the interaction time T_{int} so that the detrimental effect of the environmental noise may become small, which is a similar method to the case in Sec. 3.A of Chapter 3 where we considered the noise arising from internal interactions.

4.4.1 Description of the noise model

For the Ramsey measurement scheme which uses the GHZ state as the probe state, it has been found that improved sensitivity with the scaling $\delta\omega_z = \mathcal{O}(L^{-3/4})$ can be achieved with the interaction time of $T_{\text{int}} = \mathcal{O}(L^{-1/2})$ when the noise is time-inhomogeneous dephasing [51, 52, 52, 134, 198, 240, 241, 242], which is also referred to as Non-Markovian dephasing [51, 52, 52, 240, 56]. This scaling is called the Zeno limit. On the other hand, no improvement of scaling over the SQL is realized in the presence of Markovian noise [49, 50]. Time-inhomogeneous dephasing can be observed when the correlation time τ_c of the environment is longer than the coherence time of the spins. It is known that solid-state systems that have a strong coupling with magnetic fields, such as a superconducting flux qubit [243, 227, 244], a spin spin in a quantum dot [245, 246], and an NV center in diamond [219, 222, 247, 248], are typically subject to such time-inhomogeneous dephasing and the correlation time of these systems is much longer than the coherence time in these systems. In this section, we consider the effect of time-inhomogeneous dephasing acting on each spin independently.

We assume that the dephasing time T_2 and the relaxation time $T_{1,\text{relax}}$ of the spins satisfy

$$T_{1,\text{init}}, t_{\text{measure}}, t^* \ll T_2 \ll T_{1,\text{relax}} \ll \tau_c. \quad (4.29)$$

This implies the following three: first, the necessary condition of our noise model $T_2 \ll \tau_c$ is

satisfied; second, the relaxation time of the probe spins $T_{1,\text{relax}}$ is much longer than T_2 during the exposure; third, the total sensing time T_{sensing} is well approximated by T_{int} . For most of the solid-state systems, $T_{1,\text{relax}}$ is much longer than T_2 especially at a low temperature [226, 227, 228, 229, 230, 231, 232] as we have mentioned in Sec. 4.3.1. Therefore we assume that the effect of the energy relaxation is negligible compared to that of the dephasing during the exposure of the probe spins to the target magnetic field.

We specifically consider the following master equation of the system during the step (iii');

$$\frac{d}{dt}\hat{\rho}(t) = -i[\hat{H}_{\text{Ising}} + \hat{H}_{\omega_z}, \hat{\rho}(t)] - \frac{t}{2T_2^2} \sum_{n=1}^L [\hat{\sigma}_n^z, [\hat{\sigma}_n^z, \hat{\rho}(t)]]. \quad (4.30)$$

This kind of model has been used to describe noise in various solid-state systems [249, 243, 244, 247, 250, 248, 251, 227, 252, 240]. We then obtain the solution for Eq. (4.30) as follows:

$$\hat{\rho}(T_{\text{int}}) = \varepsilon_1(\varepsilon_2(\cdots \varepsilon_L(\hat{\rho}_I(0)) \cdots)), \quad (4.31)$$

$$\varepsilon_n(\hat{\rho}) := \frac{1 + e^{-(T_{\text{int}}/T_2)^2}}{2} \hat{\rho} + \frac{1 - e^{-(T_{\text{int}}/T_2)^2}}{2} \hat{\sigma}_n^z \hat{\rho} \hat{\sigma}_n^z, \quad (4.32)$$

$$\hat{\rho}_I(0) := e^{-i(\hat{H}_{\text{Ising}} + \hat{H}_{\omega_z})T_{\text{int}}} \hat{\rho}(0) e^{i(\hat{H}_{\text{Ising}} + \hat{H}_{\omega_z})T_{\text{int}}}. \quad (4.33)$$

4.4.2 Numerical results for the case with environmental noise

Now, we numerically calculate $\delta\omega_z$ using Eqs. (4.31)–(4.33). As in the noiseless case we take $T_{\text{sensing}} = T_{\text{int}} + 2t_{\text{opt}}^*$ in the calculation. In contrast to the case in Sec. 4.3.4, where the probability (4.25) is the function of $\omega_z T_{\text{int}}$, the slope $|dP/d\omega_z|$ depends nontrivially on T_{int} in the presence of noise [51, 52, 56]. We thereby numerically tune the interaction time T_{int} so that the uncertainty may take a minimum value. The size dependence of the interaction time T_{int} is shown in Fig. 4.6 (a). This size dependence is consistent with the previous results using the GHZ state for sensing under the effect of time-inhomogeneous dephasing [49, 51, 52, 56]. We stress here that the interaction time T_{int} is much longer than the optimized preparation time t_{opt}^* with the parameter sets we choose in Figs. 4.6 (a) and 4.6 (b).

Figure 4.6 (b) shows the uncertainty $\delta\omega_z$ in the presence of the time-inhomogeneous dephasing at the step (iii') in our scheme with three values of β . They demonstrate that our scheme beats the SQL by a constant factor except when the inverse temperature of the initial state is $\beta = 5$. However, we find that the improvement of $\delta\omega_z$ in our scheme over the SQL of the conventional scheme becomes smaller compared with the case without dephasing (see Fig. 4.5 (b)).

4.5 Discussion: Application to a large system

In this section, we discuss the metrological advantage of our scheme in a large system. As we have seen in Fig. 4.5 (b), the uncertainty begins to saturate as we increase L with a fixed β , and eventually our scheme may give no advantage over the conventional scheme with separable L -spin states. However, as long as there is at least one length L^* at which our scheme with the initial state $\hat{\rho}_\beta$ beats the SQL, one can make use of our scheme to obtain an improved sensitivity by taking the length of the chain as L^* . For an N -spin probe, using N/L^* copies of the transverse-field Ising chain of length L^* allows us to obtain the sensitivity which is $\delta\omega_z^{\text{SQL}}(L^*)/\delta\omega_z(L^*, \beta)$ times better than the SQL (see Fig. 4.7), where $\delta\omega_z^{\text{SQL}}(L)$ denotes the SQL with L spins and

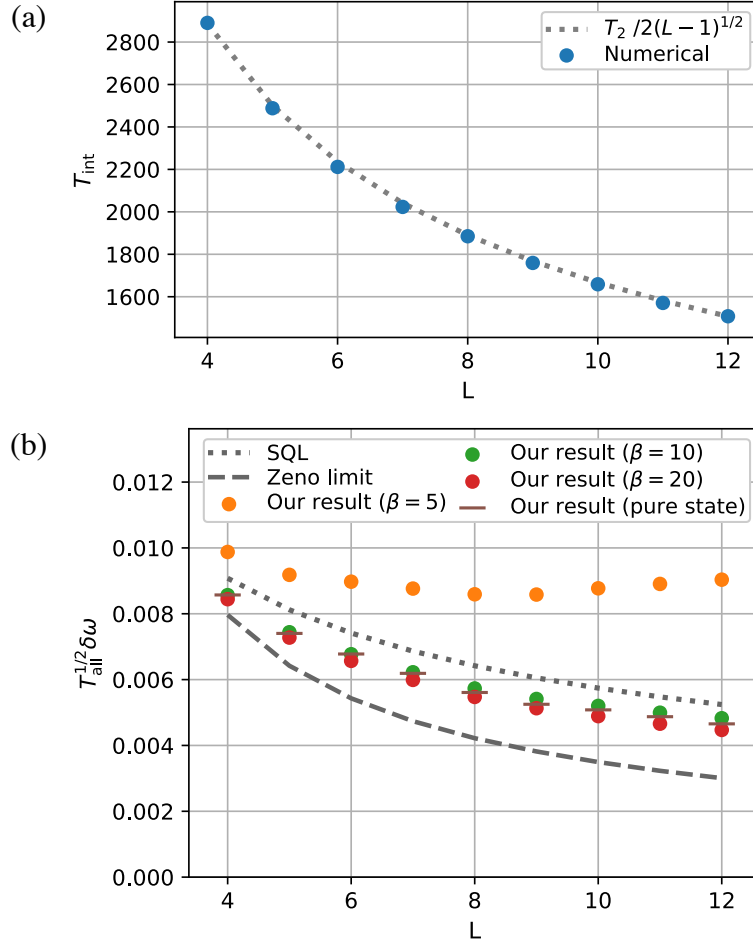


Figure 4.6: (a) The optimal interaction time T_{int} in the presence of noise. We numerically obtained T_{int} at which the minimum uncertainty is achieved in our scheme under the time-inhomogeneous dephasing. The broken line shows the function $T_{\text{int}} = (1/2)T_2(L-1)^{-1/2}$ at which the minimum uncertainty is achieved when the probe is in the GHZ state of $(L-1)$ spins [51, 52, 56]. (b) Size dependence of the uncertainty $\delta \omega_z$ in our scheme under the time-inhomogeneous dephasing. The dotted line shows the SQL for L -spins, i.e., $T_{\text{all}}^{1/2} \delta \omega_z = \sqrt{2} \exp(1/4)(LT_2)^{-1/2}$, and the broken line shows the Zeno limit for $(L-1)$ spins, i.e., $T_{\text{all}}^{1/2} \delta \omega_z = \sqrt{2} \exp(1/4)(L-1)^{-3/4} T_2^{-1/2}$ [49, 51, 52, 56]. The other symbols in the figure show $\delta \omega_z$ for the cases in which the initial states are $\hat{\rho}_\beta$ with $\beta = 5, 10$, and 20 , and $\bigotimes_{n=1}^L |0\rangle_n$, respectively. Both in (a) and (b), the parameters are taken as $h_x = 0.1$, $\beta = 10$, $\omega_z = 10^{-6}$, and $T_2 = 10^4$. All parameters are normalized by $J = 1$. [Reproduced from Fig. 7 and 8 in Ref. [76].]

$\delta\omega_z(L, \beta)$ denotes the uncertainty in our scheme with L spin equilibrium state $\hat{\rho}_\beta$. This constant-factor improvement can be maximized by tuning the length of each chain under the restriction that $\delta\omega_z(L, \beta) < \delta\omega_z^{\text{SQL}}(L)$. A similar technique was discussed in Ref. [253].

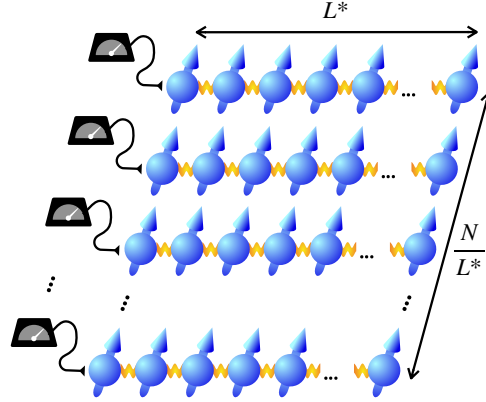


Figure 4.7: For a large number $N (\gg L^*)$ of spins, improved sensitivity by a constant factor can be maintained by separating the spins into the chains of length L^* . In this case, the probe consists of N/L^* copies of the transverse-field Ising chain. [Reproduced from Fig. 9 in Ref. [76].]

Summarizing the above, the uncertainty in our scheme can beat the SQL as we show in Figs. 4.5 (b) and 4.6 (b) as long as the the following assumptions (a) and (b) in addition to the validity of the secular approximation (4.20) are valid: (a) the temperature of the initial state $1/\beta$ is small enough for a fixed chain length L , so that the approximation Eq. (11) becomes good; (b) the decoherence times T_1 and T_2 are long enough compared to $T_{1,\text{init}}$, t_{measure} , and t_{opt}^* for a fixed chain length L , so that T_{int} dominates the sensing time T_{sensing} . (When the noise is present, $T_{\text{int}} \simeq (1/2)T_2(L-1)^{-1/2}$ is needed for achieving the minimum uncertainty [49, 50], see Fig. 4.6 (a), and hence T_2 should be also much longer than $2(L-1)^{1/2}$.) We note that if we keep increasing the length of the chain of spins while keeping β , T_1 and T_2 fixed, the sensitivity in our scheme will be eventually degraded with the increase of L . However, if we increase the number of chains as the number of available spins grows, while keeping the length of the chains fixed but large enough, we can achieve scaling of the SQL with an improved constant.

4.6 Conclusion and outlook

In this Chapter, we have proposed a novel scheme for quantum sensing using an Ising chain with homogeneous nearest-neighbor couplings. Our scheme consists of three operations: initialization of the system in a thermal equilibrium state, switching on/off global magnetic fields, and projective measurements on a single spin at the start and the end of the scheme. Specifically, we approximately create a GHZ state from the equilibrium of the transverse-field Ising chain by inducing the quantum domino dynamics. We have numerically shown that our scheme beats the SQL by a constant factor even in the presence of time-inhomogeneous dephasing. Since neither an accurate control of the spins, such as the entangling gate operations, nor long-range interaction between spins is required in the whole process, our scheme may provide an experimentally feasible way to realize entanglement enhanced sensors. Finally, we note that the quantum domino dynamics can be largely enhanced, i.e., nearly perfect creation of a GHZ state can be achieved, by employing a method using a moving control field in Ref. [139], which is shown to be even robust against the presence of disorders in Ising couplings. We expect that

our scheme in this Chapter can be improved and made more robust by combining with other techniques in the future [254].

Chapter 5

Conclusion

In this Thesis, we have studied quantum thermalization and quantum metrology using quantum Ising models. In Chapter 2, we revealed that a novel form of the Hilbert space fragmentation (HSF) emerges in this model, exhibiting a rich variety of non-equilibrium phenomena in isolated quantum systems. We then demonstrated in Chapter 3 that our findings above can be employed to design a new scheme of robust quantum sensor for measuring a weak magnetic field. We also showed in Chapter 4 that another phenomenon which has been found in the quantum Ising model can be utilized to propose a new entanglement-enhanced sensing scheme that requires few controls on the probe system. The present Thesis can be seen as yet another example of how fundamental understanding of a simple quantum model may aid increase our knowledge of the ubiquitous but challenging problems of quantum thermalization and furthermore result in applications in quantum technologies, such as quantum metrology.

In Chapter 2, we showed the breakdown of ergodicity in d -dimensional Ising models with a weak transverse field in a prethermal regime. The quantum Ising model is one of the fundamental models in quantum many-body systems, yet a full understanding of its dynamics remains elusive in higher than one dimension. We investigated the effective model that is obtained as the first-order approximation of the weak transverse field and demonstrated that the novel HSF occurs in this non-integrable model with $d \geq 2$ as a consequence of the emergent conservation law of the domain wall (DW) number. Our results indicate nontrivial initial-state dependence for non-equilibrium prethermal dynamics of the original Ising models in a weak transverse field. From the broader perspective of understanding quantum thermalization, our results suggest that the seemingly ubiquitous phenomenon of thermalization can be hindered for a certain timescale owing to a microscopic detail of the model, namely the DW conserving constraint on the spin-flip process.

Here, we describe future perspective. First, a question as to the final equilibrium of the original quantum Ising model remains open. In other words, it is not completely clear whether the Ising model under a weak magnetic field always eventually thermalize, as we have reviewed in Chapter 1. As a next step in understanding dynamics of this model, it would be interesting to investigate an effective model that describes a longer timescale than the model studied here, as has been partly studied in Ref. [165, 166, 180]. Second, it is worth mentioning that the HSF is deeply related to the question of which conserved quantity should be considered in confirming the ETH. In general, global conserved quantities can be always constructed for any model by adopting projection operators onto the energy eigenstates, which generally have no locality. Therefore, completely ignoring the locality in considering conserved quantities in the model should be too naive to be useful. Typically, the ETH in non-integrable models has been

numerically examined after resolving conventional symmetries, such as lattice symmetries including inversion symmetry, and local conservation laws including particle number conservation [11, 105, 106]. Importantly, the HSF suggests that the appearance of non-trivial and non-local conserved quantities [109, 116] can shatter conventional symmetry sectors into disconnected subspaces, while some of which can obey the ETH restricted to the fractured Krylov subspaces [34]. The quest of constructing a unified way for characterizing physically relevant conserved quantities remains an important direction to be explored.

In Chapter 3, we proposed an entanglement-enhanced sensing scheme that is robust against spatially non-uniform always-on Ising interactions. In particular, the use of the HSF constitutes a new approach in our quantum sensing scheme. Using the non-thermalizing behavior due to the emergent HSF in the quantum Ising model which we discovered in Chapter 2, we showed that a particular probe state can be used to statically decouple a fraction of spins from interacting with the rest of the system. We have also analytically evaluated the sensitivity in our scheme and demonstrated the Heisenberg limit can be achieved. We expect that methods like ours, that is to employ nontrivial mechanisms known in the field of quantum thermalization for preventing desired probe states of interacting probe systems from thermalization, would be beneficial in other areas where maintaining entanglement plays a crucial role.

We note here that the sensitivity in Chapter 3 was evaluated analytically by assuming that environmental noises are negligible. However, it is unclear how robust our quantum scheme is to realistic environmental noises such as the dephasing. Examining robustness of the freezing of spins as well as the sensitivity against noises and perturbations are other future directions of extending our results. Additionally, it will be important to make sure that the preparation of our entangled probe state is feasible in order to demonstrate the usefulness of our strategy. Future works will need to address issues such as the relevant timescale for projecting the ancillary spins onto the frozen configuration and estimating maximal errors that are allowed to be accumulated during the preparation and readout steps.

In Chapter 4, we proposed another quantum sensing scheme. This time, we adopted the quantum Ising chain as the probe system, making use of the quantum domino dynamics for the generation and readout of the entangled states. Our scheme can be implemented without dynamically controlling the interactions and requires few individual controls on the system, specifically, cooling down the system, two projective measurements on a single qubit, and turning on/off the uniform magnetic fields. Unlike in Chapter 3, we included the effect of environmental noise in our evaluation of the sensitivity and numerically demonstrated that our scheme achieves an improved sensitivity beyond the standard quantum limit even under the effect of time-inhomogeneous dephasing.

Quantum domino dynamics has been experimentally demonstrated [141], and we thereby expect that our sensing scheme will be useful in physical systems where individual control of interactions and pulse controls of each qubit are difficult. Nevertheless, we note that more work will be needed to show the improved sensitivity in realistic settings, since the present calculations do not account for the effect of environmental noise on the Domino dynamics, which would make the sensitivity worse compared to our results in which we take into account environmental noise only in the interrogation step. It will be interesting to investigate if we can design more realistic sensing schemes while retaining the advantages of our approach.

In the present thesis, we investigated two fundamental questions. The first question addresses what mechanisms can suppress thermalization in isolated quantum systems, the answer of which will lead to a better understanding of the conditions that allow for quantum thermalization. The second question explores how entanglement-enhanced magnetic-field sensors can be realized

when the probe qubits have always-on internal interactions, which will help realizing highly sensitive quantum sensors for practical use. To address the first question, this thesis analytically presented that the kinetic constraint due to the conservation of the domain-wall number hinders quantum thermalization through the emergence of HSF. Our discovery that the HSF appears even in well-known models including the TFIMs when considering a prethermal regime suggests the subtlety of discussing the ETH and highlights the need for further research in this area. In addressing the second question, we proposed two novel approaches that utilize knowledge of non-equilibrium phenomena in systems with Ising-type interactions to prepare, protect, and read out quantum states that are useful for sensing. Our results demonstrate a potential for realizing entanglement-enhanced sensors in realistic scenarios in which many-body interactions become non-negligible. Overall, this thesis contributes to the advancement of our understanding of non-equilibrium physics in isolated quantum systems and its applications to quantum metrology.

Appendix A

Proof of the theorem in Appendix 3.C

In this Appendix, to make this thesis self-contained, we provide a proof of our theorem which we introduced in Appendix 3.C. As we have clarified in Chapter 3, this is a generalized version of the bound in Ref. [160] and one can prove it by following the description Ref. [160] with a slight modification. The difference between the proof in Ref. [160] and the proof below is described in Appendix 3.C.

– Universal error bound

Consider a Hamiltonian $\hat{H} = \hat{H}_0 + \hat{V}$ of a quantum system, where \hat{H}_0 is regarded as a non-perturbed part and \hat{V} is a small perturbation. Let \mathcal{H}_P be a certain energy eigenspace of \hat{H}_0 and write \hat{P} as the projection operator on \mathcal{H}_P . Suppose that another energy eigenspace \mathcal{H}_R ($\mathcal{H}_P \cap \mathcal{H}_R = \phi$) of the Hamiltonian \hat{H}_0 satisfies the following two conditions:

- (I) $\hat{P}\hat{V}(1 - \hat{P}) + (1 - \hat{P})\hat{V}\hat{P} = \hat{P}\hat{V}\hat{R} + \hat{R}\hat{V}\hat{P}$, where \hat{R} is the projection onto the energy eigenspace \mathcal{H}_R ;
- (II) Energy spectra of \mathcal{H}_P and \mathcal{H}_R are separated by a finite energy gap $\Delta_{PR} > 0$, where $\Delta_{PR} := \min_{|E\rangle \in \mathcal{H}_P, |E'\rangle \in \mathcal{H}_R} |E - E'|$.

Then, starting from an initial state belonging to \mathcal{H}_P , we have the following error bound between the original dynamics described by \hat{H} and effective dynamics by $\hat{H}_P = \hat{P}\hat{H}\hat{P}$:

$$\epsilon(t) := \left\| \hat{P} \left(e^{i\hat{H}t} \hat{O} e^{-i\hat{H}t} - e^{i\hat{H}_P t} \hat{O} e^{-i\hat{H}_P t} \right) \hat{P} \right\| \quad (\text{A.1})$$

$$\leq \frac{4\|\hat{V}\|}{\Delta_{PR}} + 2 \left(e^{2\|\hat{V}\|/\Delta_{PR}} - 1 \right) \|\hat{V}\|t \quad (\text{A.2})$$

for any \hat{O} with $\|\hat{O}\| = 1$, where $\|\cdot\|$ denotes the operator norm.

– proof

We divide the proof into the following five steps (i)–(v). In step (ii), we assume that there is an anti-Hermitian operator \hat{T} ($\hat{T}^\dagger = -\hat{T}$) that satisfies

$$[\hat{T}, \hat{H}_0] = -\hat{V}_{\text{off}}. \quad (\text{A.3})$$

In fact, the existence of the solution \hat{T} for Eq. (A.3) is proved in step (iii) by using the condition (II).

Step (i)

We show

$$\epsilon(t) \leq 4\|\hat{T}\| + 2\|\hat{V}'\|t, \quad (\text{A.4})$$

where $\hat{V}' := \hat{S}\hat{H}\hat{S}^\dagger - \hat{H}_1$ with $\hat{H}_1 := \hat{H}_0 + \hat{V}_{\text{diag}}$ and $\hat{S} := e^{\hat{T}}$.

Step (ii)

We show

$$\|\hat{V}'\| \leq (e^{2\|\hat{T}\|} - 1)\|\hat{V}\|. \quad (\text{A.5})$$

Step (iii)

We show that there always exists the solution \hat{T} for Eq. (A.3) when the condition (II) is satisfied, which has the form of $\hat{T} = (\hat{P}\hat{T}\hat{R} + \hat{R}\hat{T}\hat{P})$. In particular, we derive the matrix $\bar{T}_{\text{PR}} \equiv \hat{P}\hat{T}\hat{R}$ from the Sylvester equation $\bar{H}_{0\text{P}}\bar{T}_{\text{PR}} - \bar{T}_{\text{PR}}\bar{H}_{0\text{R}} = \bar{V}_{\text{PR}}$, where $\bar{H}_{0\text{P}} \equiv \hat{P}\hat{H}_0\hat{P}$, $\bar{H}_{0\text{R}} \equiv \hat{R}\hat{H}_0\hat{R}$, and $\bar{V}_{\text{PR}} \equiv \hat{P}\hat{V}\hat{R}$.

Step (iv)

We show

$$\|\bar{T}_{\text{PR}}\| \leq \frac{\|\bar{V}_{\text{PR}}\|}{\Delta_{\text{PR}}}. \quad (\text{A.6})$$

Step (v)

We show

$$\|\hat{T}\| = \|\bar{T}_{\text{PR}}\| \quad (\text{A.7})$$

and

$$\|\bar{V}_{\text{PR}}\| \leq \|\hat{V}\|. \quad (\text{A.8})$$

Combining Eqs. (A.4)–(A.8), we arrive at the universal bound Eq. (A.2). Below, we show the derivations Eqs. (A.4)–(A.7) in each proof step.

Step (i): derivation of Eq. (A.4)

First, we rewrite $\epsilon(t)$ as follows:

$$\epsilon(t) = \left\| \hat{\mathbb{P}} \left(e^{i\hat{H}t} \hat{O} e^{-i\hat{H}t} - e^{i\hat{H}_P t} \hat{O} e^{-i\hat{H}_P t} \right) \hat{\mathbb{P}} \right\| \quad (\text{A.9})$$

$$= \left\| \hat{\mathbb{P}} \left(e^{-i\hat{H}_P t} e^{i\hat{H}t} \hat{O} e^{-i\hat{H}t} e^{i\hat{H}_P t} - \hat{O} \right) \hat{\mathbb{P}} \right\| \quad (\text{A.10})$$

$$= \left\| \hat{\mathbb{P}} \left(e^{-i\hat{H}_1 t} e^{i\hat{H}t} \hat{O} e^{-i\hat{H}t} e^{-i\hat{H}_1 t} - \hat{O} \right) \hat{\mathbb{P}} \right\| \quad (\text{A.11})$$

$$= \left\| \hat{\mathbb{P}} \left(e^{-i\hat{H}_1 t} e^{-\hat{\mathbb{T}}} e^{i\hat{H}_1 t} e^{-i\hat{H}_1 t} e^{\hat{\mathbb{T}}} e^{i\hat{H}t} e^{-\hat{\mathbb{T}}} e^{\hat{\mathbb{T}}} \hat{O} e^{-\hat{\mathbb{T}}} e^{\hat{\mathbb{T}}} e^{-i\hat{H}t} e^{-\hat{\mathbb{T}}} e^{i\hat{H}_1 t} e^{-i\hat{H}_1 t} e^{\hat{\mathbb{T}}} e^{i\hat{H}_1 t} - \hat{O} \right) \hat{\mathbb{P}} \right\| \quad (\text{A.12})$$

$$= \left\| \hat{\mathbb{P}} \left(S^\dagger(t) \hat{\mathbb{L}}(t) S \hat{O} S^\dagger \hat{\mathbb{L}}(t)^\dagger \hat{\mathbb{S}}(t) - \hat{O} \right) \hat{\mathbb{P}} \right\|, \quad (\text{A.13})$$

where operators \hat{H}_1 , $\hat{\mathbb{S}}(t)$, and $\hat{\mathbb{L}}(t)$ are defined as

$$\hat{H}_1 := \hat{H}_0 + \hat{V}_{\text{diag}}, \quad (\text{A.14})$$

$$\hat{\mathbb{S}}(t) := e^{-i\hat{H}_1 t} \hat{\mathbb{S}} e^{i\hat{H}_1 t} = e^{-i\hat{H}_1 t} e^{\hat{\mathbb{T}}} e^{i\hat{H}_1 t}, \quad (\text{A.15})$$

$$\hat{\mathbb{L}}(t) := e^{-i\hat{H}_1 t} e^{\hat{\mathbb{T}}} e^{i\hat{H}t} e^{-\hat{\mathbb{T}}}, \quad (\text{A.16})$$

with

$$\hat{V}_{\text{diag}} := \hat{\mathbb{P}} \hat{V} \hat{\mathbb{P}} + (1 - \hat{\mathbb{P}}) \hat{V} (1 - \hat{\mathbb{P}}) \quad (\text{A.17})$$

and we used $\hat{\mathbb{P}} \hat{H}_1 = \hat{H}_1 \hat{\mathbb{P}} = \hat{H}_P$. Then, using the following inequalities

$$\left\| \hat{U} \hat{O} \hat{U}^\dagger - \hat{O} \right\| = \left\| [\hat{U}, \hat{O}] \hat{U}^\dagger \right\| \leq \left\| [\hat{U}, \hat{O}] \right\|, \quad (\text{A.18})$$

$$\left\| [\hat{U}_a \hat{U}_b, \hat{O}] \right\| = \left\| \hat{U}_a [\hat{U}_b, \hat{O}] + [\hat{U}_a, \hat{O}] \hat{U}_b \right\| \leq \left\| [\hat{U}_b, \hat{O}] \right\| + \left\| [\hat{U}_a, \hat{O}] \right\|, \quad (\text{A.19})$$

we obtain a bound on $\epsilon(t)$ as follows:

$$\epsilon(t) \leq \left\| \left(S^\dagger(t) \hat{\mathbb{L}}(t) S \hat{O} S^\dagger \hat{\mathbb{L}}(t)^\dagger \hat{\mathbb{S}}(t) - \hat{O} \right) \right\| \quad (\text{A.20})$$

$$\leq \left\| [\hat{\mathbb{S}}, \hat{O}] \right\| + \left\| [\hat{\mathbb{S}}(t), \hat{O}] \right\| + \left\| [\hat{\mathbb{L}}(t), \hat{O}] \right\|. \quad (\text{A.21})$$

Second, we use another inequality

$$\left\| [e^{\hat{\mathbb{T}}}, \hat{O}] \right\| = \left\| \int_0^1 d\lambda e^{\lambda \hat{\mathbb{T}}} [e^{\hat{\mathbb{T}}}, \hat{O}] e^{-\lambda \hat{\mathbb{T}}} \right\| \leq \int_0^1 d\lambda \left\| e^{\lambda \hat{\mathbb{T}}} [e^{\hat{\mathbb{T}}}, \hat{O}] e^{-\lambda \hat{\mathbb{T}}} \right\| \leq 2 \left\| \hat{\mathbb{T}} \right\| \quad (\text{A.22})$$

to arrive at

$$\epsilon(t) \leq 4 \left\| \hat{\mathbb{T}} \right\| + \left\| [\hat{\mathbb{L}}(t), \hat{O}] \right\| \quad (\text{A.23})$$

from Eq. (A.21). Finally, we see that the second term of the left-hand side of Eq. (A.23) can be upper bounded as

$$\left\| [\hat{L}(t), \hat{O}] \right\| = \left\| \hat{L}^\dagger(t) \hat{O} \hat{L}(t) - \hat{O} \right\| \quad (\text{A.24})$$

$$= \left\| i \int_0^t d\tau \frac{d}{d\tau} \left(e^{-i\hat{S}\hat{H}\hat{S}^\dagger\tau} e^{i\hat{H}_1\tau} \hat{O} e^{-i\hat{H}_1\tau} e^{i\hat{S}\hat{H}\hat{S}^\dagger\tau} \right) \right\| \quad (\text{A.25})$$

$$= \left\| \int_0^t d\tau e^{-i\hat{S}\hat{H}\hat{S}^\dagger\tau} e^{i\hat{H}_1\tau} [\hat{H}_1 - e^{-i\hat{H}_1\tau} \hat{S}\hat{H}\hat{S}^\dagger e^{i\hat{H}_1\tau}, \hat{O}] e^{-i\hat{H}_1\tau} e^{i\hat{S}\hat{H}\hat{S}^\dagger\tau} \right\| \quad (\text{A.26})$$

$$= \left\| \int_0^t d\tau e^{-i\hat{S}\hat{H}\hat{S}^\dagger\tau} e^{i\hat{H}_1\tau} [-e^{-i\hat{H}_1\tau} \hat{V}' e^{i\hat{H}_1\tau}, \hat{O}] e^{-i\hat{H}_1\tau} e^{i\hat{S}\hat{H}\hat{S}^\dagger\tau} \right\| \quad (\text{A.27})$$

$$= \left\| \int_0^t d\tau L^\dagger(\tau) [e^{-i\hat{H}_1\tau} \hat{V}' e^{i\hat{H}_1\tau}, \hat{O}] L(\tau) \right\| \quad (\text{A.28})$$

$$\leq \int_0^t d\tau \left\| [e^{-i\hat{H}_0\tau} \hat{V}' e^{i\hat{H}_0\tau}, \hat{O}] \right\| \quad (\text{A.29})$$

$$\leq 2 \left\| \hat{V}' \right\| t, \quad (\text{A.30})$$

and thus we obtain the following:

$$\epsilon(t) \leq 4 \left\| \hat{T} \right\| + 2 \left\| \hat{V}' \right\| t. \quad (\text{A.31})$$

Step (ii): derivation of Eq. (A.5)

First we rewrite \hat{V}' as

$$\hat{V}' = \sum_{n=0}^{\infty} \frac{1}{n!} \text{ad}_{\hat{T}}^n(\hat{H}_0 + \hat{V}) - \hat{H}_1 \quad (\text{A.32})$$

$$= \sum_{n=0}^{\infty} \frac{1}{n!} \text{ad}_{\hat{T}}^n(\hat{H}_0) + \sum_{n=0}^{\infty} \frac{1}{n!} \text{ad}_{\hat{T}}^n(\hat{V}) - (\hat{H}_0 + \hat{V}_{\text{diag}}) \quad (\text{A.33})$$

$$= \sum_{n=0}^{\infty} \frac{1}{n!} \text{ad}_{\hat{T}}^n(\hat{V}_{\text{off}} + \hat{V}_{\text{diag}}) - \sum_{n=1}^{\infty} \frac{1}{(n+1)!} \text{ad}_{\hat{T}}^n(\hat{V}_{\text{off}}) - (\hat{V}_{\text{off}} + \hat{V}_{\text{diag}}) \quad (\text{A.34})$$

$$= \sum_{n=1}^{\infty} \frac{1}{n!} \text{ad}_{\hat{T}}^n(\hat{V}_{\text{off}} + \hat{V}_{\text{diag}}) - \sum_{n=1}^{\infty} \frac{1}{(n+1)!} \text{ad}_{\hat{T}}^n(\hat{V}_{\text{off}}) \quad (\text{A.35})$$

by using the expansion

$$\sum_{n=0}^{\infty} \frac{1}{n!} \text{ad}_{\hat{T}}^n(\hat{H}_0) = \hat{H}_0 + [\hat{T}, \hat{H}_0] + \frac{1}{2} [\hat{T}, [\hat{T}, \hat{H}_0]] + \dots \quad (\text{A.36})$$

$$= \hat{H}_0 - \hat{V}_{\text{off}} - \frac{1}{2} [\hat{T}, \hat{V}_{\text{off}}] - \frac{1}{6} [\hat{T}, [\hat{T}, \hat{V}_{\text{off}}]] - \dots \quad (\text{A.37})$$

$$= \hat{H}_0 - \hat{V}_{\text{off}} - \sum_{n=1}^{\infty} \frac{1}{(n+1)!} \text{ad}_{\hat{T}}^n(\hat{V}_{\text{off}}), \quad (\text{A.38})$$

where $\text{ad}_{\hat{T}}(\cdot)$ indicates taking a commutation $[\hat{T}, \cdot]$. Using Eq. (A.35), we can evaluate $\|\hat{V}'\|$ as follows:

$$\|\hat{V}'\| \leq \sum_{n=1}^{\infty} \frac{1}{n!} \|\text{ad}_{\hat{T}}^n(\hat{V})\| + \sum_{n=1}^{\infty} \frac{1}{(n+1)!} \|\text{ad}_{\hat{T}}^n(\hat{V}_{\text{off}})\| \quad (\text{A.39})$$

$$\leq \sum_{n=1}^{\infty} \frac{\|2\hat{T}\|^n}{n!} \|\hat{V}\| + \sum_{n=1}^{\infty} \frac{\|2\hat{T}\|^n}{(n+1)!} \|\hat{V}\| \quad (\text{A.40})$$

$$\leq \left(\sum_{n=0}^{\infty} \frac{\|2\hat{T}\|^n}{n!} - 1 + \sum_{n=1}^{\infty} \frac{\|2\hat{T}\|^n}{(n+1)!} \right) \|\hat{V}\| \quad (\text{A.41})$$

$$\leq \left(\sum_{n=0}^{\infty} \frac{\|2\hat{T}\|^n}{n!} + \sum_{n=0}^{\infty} \frac{\|2\hat{T}\|^n}{(n+1)n!} - 2 \right) \|\hat{V}\| \quad (\text{A.42})$$

$$\leq 2 \left(\sum_{n=0}^{\infty} \frac{\|2\hat{T}\|^n}{n!} - 1 \right) \|\hat{V}\| \quad (\text{A.43})$$

$$\leq 2 \left(e^{\|2\hat{T}\|} - 1 \right) \|\hat{V}\|. \quad (\text{A.44})$$

Step (iii): derivation of the solution for Eq. (A.3)

We assume that the anti-Hermitian operator \hat{T} has the form of $\hat{T} = \hat{P}\hat{T}\hat{R} + \hat{R}\hat{T}\hat{P}$. Then, Eq. (A.3), which is $[\hat{T}, \hat{H}_0] = -\hat{V}_{\text{off}}$, is reduced to the following equation of matrices which represent diagonal or off-diagonal blocks of \hat{V} , \hat{T} , and \hat{H}_0 ,

$$\bar{T}_{\text{PR}}\bar{H}_{0\text{R}} - \bar{H}_{0\text{P}}\bar{T}_{\text{PR}} = -\bar{V}_{\text{PR}}, \quad (\text{A.45})$$

where $\bar{T}_{\text{PR}} \equiv \hat{P}\hat{T}\hat{R}$, $\bar{H}_{0\text{R}} \equiv \hat{R}\hat{H}_0\hat{R}$, $\bar{H}_{0\text{P}} \equiv \hat{P}\hat{H}_0\hat{P}$, and $\bar{V}_{\text{PR}} \equiv \hat{P}\hat{V}\hat{R}$. This is a Sylvester equation. From the assumption (II), we see that $\bar{H}_{0\text{P}}$ and $\bar{H}_{0\text{R}}$ have no common eigenvalues. In this case, for any matrix $-\bar{V}_{\text{PR}}$, it is known that there always exists a unique solution that satisfies the Sylvester equation.

Formally, we can write the solution as follows. Since we are assuming that the subspaces \mathcal{H}_{P} and \mathcal{H}_{R} are separated by a finite energy gap Δ_{PR} , one can find $E_p \in [\min\Lambda_{\text{P}}, \max\Lambda_{\text{P}}]$ and r_p such that the subspace \mathcal{H}_{P} is covered by $[E_p - r_p, E_p + r_p]$ and \mathcal{H}_{R} is covered by $(-\infty, E_p - r_p - \Delta_{\text{PR}}] \cup [E_p + r_p + \Delta_{\text{PR}}, \infty)$. Then, we can obtain

$$\bar{T}_{\text{PR}} = [(\bar{H}_{0\text{P}} - E_p)\bar{T}_{\text{PR}} - \bar{V}_{\text{PR}}]/(\bar{H}_{0\text{R}} - E_p) \quad (\text{A.46})$$

$$= \sum_{n=0}^{\infty} (\bar{H}_{0\text{P}} - E_p)^n \bar{V}_{\text{PR}} (\bar{H}_{0\text{R}} - E_p)^{-(n+1)}. \quad (\text{A.47})$$

Step (iv): derivation of Eq. (A.6)

Evaluating \bar{T}_{PR} can be done straightforwardly by using Eq. (A.47) as follows:

$$\|\bar{T}_{\text{PR}}\| \leq \sum_{n=0}^{\infty} \|(\mathbf{H}_{0\text{P}} - E_p)^n \bar{\mathbf{V}}_{\text{PR}} (\bar{\mathbf{H}}_R - E_p)^{-(n+1)}\| \quad (\text{A.48})$$

$$\leq \sum_{n=0}^{\infty} \|\bar{\mathbf{H}}_{0\text{P}} - E_p\|^n \|\bar{\mathbf{H}}_{0\text{R}} - E_p\|^{-(n+1)} \|\bar{\mathbf{V}}_{\text{PR}}\| \quad (\text{A.49})$$

$$\leq \sum_{n=0}^{\infty} \frac{r_p^n}{(r_p + \Delta_{\text{PR}})^{n+1}} \|\bar{\mathbf{V}}_{\text{PR}}\| \quad (\text{A.50})$$

$$= \frac{\|\bar{\mathbf{V}}_{\text{PR}}\|}{\Delta_{\text{PR}}}. \quad (\text{A.51})$$

Step (v): derivation of Eqs. (A.7) and (A.8)

We derive Eq. (A.8) first. For the solution derived in Step (iii), we have

$$\hat{\mathbf{T}}^\dagger \hat{\mathbf{T}} = (\hat{\mathbf{P}}\hat{\mathbf{T}}\hat{\mathbf{R}} + \hat{\mathbf{R}}\hat{\mathbf{T}}\hat{\mathbf{P}})(-\hat{\mathbf{P}}\hat{\mathbf{T}}\hat{\mathbf{R}} - \hat{\mathbf{R}}\hat{\mathbf{T}}\hat{\mathbf{P}}) \quad (\text{A.52})$$

$$= -(\hat{\mathbf{P}}\hat{\mathbf{T}}\hat{\mathbf{R}})(\hat{\mathbf{R}}\hat{\mathbf{T}}\hat{\mathbf{P}}) - (\hat{\mathbf{R}}\hat{\mathbf{T}}\hat{\mathbf{P}})(\hat{\mathbf{P}}\hat{\mathbf{T}}\hat{\mathbf{R}}). \quad (\text{A.53})$$

The last line (A.53) shows that $\hat{\mathbf{T}}^\dagger \hat{\mathbf{T}}$ is block diagonalized in \mathcal{H}_{P} and \mathcal{H}_{R} , and hence we obtain

$$\|\hat{\mathbf{T}}\|^2 = \max\{\|(\hat{\mathbf{P}}\hat{\mathbf{T}}\hat{\mathbf{R}})(\hat{\mathbf{R}}\hat{\mathbf{T}}\hat{\mathbf{P}})\|, \|(\hat{\mathbf{R}}\hat{\mathbf{T}}\hat{\mathbf{P}})(\hat{\mathbf{P}}\hat{\mathbf{T}}\hat{\mathbf{R}})\|\} \quad (\text{A.54})$$

$$= \max\{\|(\hat{\mathbf{P}}\hat{\mathbf{T}}\hat{\mathbf{R}})(\hat{\mathbf{P}}\hat{\mathbf{T}}\hat{\mathbf{R}})^\dagger\|, \|(\hat{\mathbf{R}}\hat{\mathbf{T}}\hat{\mathbf{P}})(\hat{\mathbf{R}}\hat{\mathbf{T}}\hat{\mathbf{P}})^\dagger\|\} \quad (\text{A.55})$$

$$= \|\hat{\mathbf{P}}\hat{\mathbf{T}}\hat{\mathbf{R}}\|^2 \quad (\text{A.56})$$

$$= \|\bar{T}_{\text{PR}}\|^2, \quad (\text{A.57})$$

where we used the relation $\|\hat{O}\|^2 = \|\hat{O}\hat{O}^\dagger\|$ for the operator norm, and we have $\|\hat{\mathbf{T}}\| = \|\bar{T}_{\text{PR}}\|$.

Finally, Eq. (A.7) follows from below:

$$\|\bar{\mathbf{V}}_{\text{PR}}\|^2 = \|\hat{\mathbf{P}}\hat{\mathbf{V}}\hat{\mathbf{R}}\|^2 = \|\hat{\mathbf{P}}\hat{\mathbf{V}}\hat{\mathbf{R}}\hat{\mathbf{R}}\hat{\mathbf{V}}\hat{\mathbf{P}}\| \leq \|\hat{\mathbf{V}}\hat{\mathbf{R}}\hat{\mathbf{R}}\hat{\mathbf{V}}\| = \|\hat{\mathbf{V}}\hat{\mathbf{R}}\|^2 = \|\hat{\mathbf{R}}\hat{\mathbf{V}}\hat{\mathbf{V}}\hat{\mathbf{R}}\| \leq \|\hat{\mathbf{V}}\|^2. \quad (\text{A.58})$$

Acknowledgement

Firstly and most importantly, I would like to thank my supervisor Naomichi Hatano for his helpful guidance, generous support, and inspiring discussions in these five years. I would next like to thank my adviser in AIST, Yuichiro Matsuzaki, for encouraging me to start the research on quantum metrology and continuously helping me with his great insights in this field. I am grateful to Ryusuke Hamazaki for inspiring me and sharing his ideas and deep knowledge on quantum thermalization. I want to express my gratitude particularly to these three again for giving me many opportunities to meet great people, showing their enthusiasm for research, and always being quick and patient in proofreading my writings. I would also like to thank all of the professors in the thesis committee, Synge Todo, Kensuke Kobayashi, Takashi Oka, Mio Murao, and Masaki Oshikawa. Their critical comments helped me to improve my work and their positive feedback kept me motivated. I appreciate the collaborations and exciting discussions with Mamiko Tatsuta, Hideaki Hakoshima, Takuya Hatomura, and especially Takashi Imoto with whom I enjoyed stimulating discussions on a wide range of topics. I am also grateful to Rahul Nandkishore and Sanjay Moudgalya for their insightful comments and fruitful discussions on the Hilbert space fragmentation and Zongping Gong for helpful comments on the error bound in Chapter 3 of this Thesis. I am indebted to all the members and staffs in Hatano research group in the University of Tokyo and quantum engineering group in AIST. I have deeply enjoyed my time there. I thank Kaoru Yamamoto and Takaaki Aoki for guiding me to join AIST. I also thank Riki Toshio, Junichi Haruna, and Takuya Yoda for stimulating discussions on physics, Kensuke Tamura, Chihiro Kondo and Cheng Shang for making the PhD course more enjoyable and endurable, and Özlem for all. Finally, I deeply thank my family and friends for their warm and continuous support.

I would also like to acknowledge financial supports on my works [74, 75, 76] by JST PRESTO (Grant No. JPMJPR1919, PI: Yuichiro Matsuzaki) Japan.

Bibliography

- [1] I. M. Georgescu, S. Ashhab, and Franco Nori. Quantum simulation. *Rev. Mod. Phys.*, 86:153–185, Mar 2014.
- [2] Mari Carmen Banuls, Rainer Blatt, Jacopo Catani, Alessio Celi, Juan Ignacio Cirac, Marcello Dalmonte, Leonardo Fallani, Karl Jansen, Maciej Lewenstein, Simone Montangero, et al. Simulating lattice gauge theories within quantum technologies. *Eur. Phys. J. D*, 74(8):1–42, 2020.
- [3] Christian W Bauer Zohreh Davoudi, A Baha Balantekin, Tanmoy Bhattacharya, Marcela Carena, Wibe A de Jong, Patrick Draper, Aida El-Khadra, Nate Gemelke, Masanori Hanada, Dmitri Kharzeev, et al. Quantum simulation for high energy physics. *arXiv e-prints*, pages arXiv–2204, 2022.
- [4] Michael A Taylor and Warwick P Bowen. Quantum metrology and its application in biology. *Phys. Rep.*, 615:1–59, 2016.
- [5] Luca Pezzè, Augusto Smerzi, Markus K. Oberthaler, Roman Schmied, and Philipp Treutlein. Quantum metrology with nonclassical states of atomic ensembles. *Rev. Mod. Phys.*, 90:035005, Sep 2018.
- [6] Josh M Deutsch. Quantum statistical mechanics in a closed system. *Phys. Rev. A*, 43(4):2046, 1991.
- [7] Mark Srednicki. Chaos and quantum thermalization. *Phys. Rev. E*, 50(2):888, 1994.
- [8] Marcos Rigol, Vanja Dunjko, and Maxim Olshanii. Thermalization and its mechanism for generic isolated quantum systems. *Nature*, 452(7189):854–858, 2008.
- [9] Hyungwon Kim, Tatsuhiko N Ikeda, and David A Huse. Testing whether all eigenstates obey the eigenstate thermalization hypothesis. *Phys. Rev. E*, 90(5):052105, 2014.
- [10] Abdellah Khodja, Robin Steinigeweg, and Jochen Gemmer. Relevance of the eigenstate thermalization hypothesis for thermal relaxation. *Phys. Rev. E*, 91(1):012120, 2015.
- [11] Luca D’Alessio, Yariv Kafri, Anatoli Polkovnikov, and Marcos Rigol. From quantum chaos and eigenstate thermalization to statistical mechanics and thermodynamics. *Adv. Phys.*, 65(3):239–362, 2016.
- [12] James R Garrison and Tarun Grover. Does a single eigenstate encode the full hamiltonian? *Phys. Rev. X*, 8(2):021026, 2018.
- [13] Toru Yoshizawa, Eiki Iyoda, and Takahiro Sagawa. Numerical large deviation analysis of the eigenstate thermalization hypothesis. *Phys. Rev. Lett.*, 120(20):200604, 2018.
- [14] Shoki Sugimoto, Ryusuke Hamazaki, and Masahito Ueda. Test of the eigenstate thermalization hypothesis based on local random matrix theory. *Phys. Rev. Lett.*, 126(12):120602, 2021.
- [15] Shoki Sugimoto, Ryusuke Hamazaki, and Masahito Ueda. Eigenstate thermalization in long-range interacting systems. *Phys. Rev. Lett.*, 129:030602, Jul 2022.

- [16] Sheldon Goldstein, Joel L Lebowitz, Roderich Tumulka, and Nino Zanghì. Canonical typicality. *Phys. Rev. Lett.*, 96(5):050403, 2006.
- [17] Sandu Popescu, Anthony J Short, and Andreas Winter. Entanglement and the foundations of statistical mechanics. *Nat. Phys.*, 2(11):754–758, 2006.
- [18] Sheldon Goldstein, Joel L Lebowitz, Christian Mastrodonato, Roderich Tumulka, and Nino Zanghi. Approach to thermal equilibrium of macroscopic quantum systems. *Phys. Rev. E*, 81(1):011109, 2010.
- [19] Giulio Biroli, Corinna Kollath, and Andreas M. Läuchli. Effect of rare fluctuations on the thermalization of isolated quantum systems. *Phys. Rev. Lett.*, 105:250401, Dec 2010.
- [20] Takashi Mori. Weak eigenstate thermalization with large deviation bound. *arXiv preprint arXiv:1609.09776*, 2016.
- [21] Eiki Iyoda, Kazuya Kaneko, and Takahiro Sagawa. Fluctuation theorem for many-body pure quantum states. *Phys. Rev. Lett.*, 119:100601, Sep 2017.
- [22] Tomotaka Kuwahara and Keiji Saito. Eigenstate thermalization from the clustering property of correlation. *Phys. Rev. Lett.*, 124:200604, May 2020.
- [23] Anatoli Polkovnikov, Krishnendu Sengupta, Alessandro Silva, and Mukund Vengalattore. Colloquium: Nonequilibrium dynamics of closed interacting quantum systems. *Rev. Mod. Phys.*, 83(3):863, 2011.
- [24] Fabian HL Essler and Maurizio Fagotti. Quench dynamics and relaxation in isolated integrable quantum spin chains. *J. Stat. Mech.*, 2016(6):064002, 2016.
- [25] Rahul Nandkishore and David A Huse. Many-body localization and thermalization in quantum statistical mechanics. *Annu. Rev. Condens. Matter Phys.*, 6(1):15–38, 2015.
- [26] Dmitry A Abanin, Ehud Altman, Immanuel Bloch, and Maksym Serbyn. Colloquium: Many-body localization, thermalization, and entanglement. *Rev. Mod. Phys.*, 91(2):021001, 2019.
- [27] Maksym Serbyn, Dmitry A Abanin, and Zlatko Papić. Quantum many-body scars and weak breaking of ergodicity. *Nat. Phys.*, 17(6):675–685, 2021.
- [28] Sanjay Moudgalya, B Andrei Bernevig, and Nicolas Regnault. Quantum many-body scars and hilbert space fragmentation: a review of exact results. *Rep. Prog. Phys.*, 85(8):086501, jul 2022.
- [29] Hannes Bernien, Sylvain Schwartz, Alexander Keesling, Harry Levine, Ahmed Omran, Hannes Pichler, Soonwon Choi, Alexander S. Zibrov, Manuel Endres, Markus Greiner, Vladan Vuletić, and Mikhail D. Lukin. Probing many-body dynamics on a 51-atom quantum simulator. *Nature*, 551(7682):579–584, 2017.
- [30] Christopher J Turner, Alexios A Michailidis, Dmitry A Abanin, Maksym Serbyn, and Zlatko Papić. Weak ergodicity breaking from quantum many-body scars. *Nat. Phys.*, 14(7):745–749, 2018.
- [31] Sanjay Moudgalya, Nicolas Regnault, and B Andrei Bernevig. Entanglement of exact excited states of affleck-kennedy-lieb-tasaki models: Exact results, many-body scars, and violation of the strong eigenstate thermalization hypothesis. *Phys. Rev. B*, 98(23):235156, 2018.
- [32] Daniel K Mark, Cheng-Ju Lin, and Olexei I Motrunich. Unified structure for exact towers of scar states in the affleck-kennedy-lieb-tasaki and other models. *Phys. Rev. B*, 101(19):195131, 2020.
- [33] Marko Žnidarič. Coexistence of diffusive and ballistic transport in a simple spin ladder.

- Phys. Rev. Lett.*, 110:070602, Feb 2013.
- [34] Sanjay Moudgalya, Abhinav Prem, Rahul Nandkishore, Nicolas Regnault, and B Andrei Bernevig. Thermalization and its absence within krylov subspaces of a constrained hamiltonian. *arXiv preprint arXiv:1910.14048*, 2019.
 - [35] Pablo Sala, Tibor Rakovszky, Ruben Verresen, Michael Knap, and Frank Pollmann. Ergodicity breaking arising from hilbert space fragmentation in dipole-conserving hamiltonians. *Phys. Rev. X*, 10(1):011047, 2020.
 - [36] Vedika Khemani, Michael Hermele, and Rahul Nandkishore. Localization from hilbert space shattering: From theory to physical realizations. *Phys. Rev. B*, 101(17):174204, 2020.
 - [37] Rahul M Nandkishore and Michael Hermele. Fractons. *Annu. Rev. Condens. Matter Phys.*, 10:295–313, 2019.
 - [38] Michael Pretko, Xie Chen, and Yizhi You. Fracton phases of matter. *Int. J. Mod. Phys. A*, 35(06):2030003, 2020.
 - [39] Zlatko Papić. Weak ergodicity breaking through the lens of quantum entanglement. In *Entanglement in Spin Chains*, pages 341–395. Springer, 2022.
 - [40] W. Wasilewski, K. Jensen, H. Krauter, J. J. Renema, M. V. Balabas, and E. S. Polzik. Quantum noise limited and entanglement-assisted magnetometry. *Phys. Rev. Lett.*, 104:133601, Mar 2010.
 - [41] R. J. Sewell, M. Koschorreck, M. Napolitano, B. Dubost, N. Behbood, and M. W. Mitchell. Magnetic sensitivity beyond the projection noise limit by spin squeezing. *Phys. Rev. Lett.*, 109:253605, Dec 2012.
 - [42] D Leibfried, Murray D Barrett, T Schaetz, J Britton, J Chiaverini, Wayne M Itano, John D Jost, Christopher Langer, and David J Wineland. Toward heisenberg-limited spectroscopy with multiparticle entangled states. *Science*, 304(5676):1476–1478, 2004.
 - [43] Christian F Roos, M Chwalla, K Kim, M Riebe, and Rainer Blatt. ‘designer atoms’ for quantum metrology. *Nature*, 443(7109):316–319, 2006.
 - [44] Judith Abadie, Benjamin P Abbott, TD Abbott, MR Abernathy, Matthew Benacquista, Teviet Creighton, H Daveloza, Maria E Diaz, R Grosso, Soumya Mohanty, et al. A gravitational wave observatory operating beyond the quantum shot-noise limit. *Nat. Phys.*, 7(12):962–965, 2011.
 - [45] Junaid Aasi, Joan Abadie, BP Abbott, Richard Abbott, TD Abbott, MR Abernathy, Carl Adams, Thomas Adams, Paolo Addesso, RX Adhikari, et al. Enhanced sensitivity of the ligo gravitational wave detector by using squeezed states of light. *Nature Photonics*, 7(8):613–619, 2013.
 - [46] C. L. Degen, F. Reinhard, and P. Cappellaro. Quantum sensing. *Rev. Mod. Phys.*, 89:035002, Jul 2017.
 - [47] D. J. Wineland, J. J. Bollinger, W. M. Itano, F. L. Moore, and D. J. Heinzen. Spin squeezing and reduced quantum noise in spectroscopy. *Phys. Rev. A*, 46:R6797–R6800, Dec 1992.
 - [48] J. J. Bollinger, Wayne M. Itano, D. J. Wineland, and D. J. Heinzen. Optimal frequency measurements with maximally correlated states. *Phys. Rev. A*, 54:R4649–R4652, Dec 1996.
 - [49] S. F. Huelga, C. Macchiavello, T. Pellizzari, A. K. Ekert, M. B. Plenio, and J. I. Cirac. Improvement of frequency standards with quantum entanglement. *Phys. Rev. Lett.*, 79:3865–

- 3868, Nov 1997.
- [50] Anil Shaji and Carlton M. Caves. Qubit metrology and decoherence. *Phys. Rev. A*, 76:032111, Sep 2007.
 - [51] Yuichiro Matsuzaki, Simon C. Benjamin, and Joseph Fitzsimons. Magnetic field sensing beyond the standard quantum limit under the effect of decoherence. *Phys. Rev. A*, 84:012103, Jul 2011.
 - [52] Alex W. Chin, Susana F. Huelga, and Martin B. Plenio. Quantum metrology in non-markovian environments. *Phys. Rev. Lett.*, 109:233601, Dec 2012.
 - [53] U Dorner. Quantum frequency estimation with trapped ions and atoms. *New J. Phys.*, 14(4):043011, apr 2012.
 - [54] R Chaves, JB Brask, Marcin Markiewicz, J Kołodyński, and A Acín. Noisy metrology beyond the standard quantum limit. *Phys. Rev. Lett.*, 111(12):120401, 2013.
 - [55] Florian Fröwis, Pavel Sekatski, Wolfgang Dür, Nicolas Gisin, and Nicolas Sangouard. Macroscopic quantum states: Measures, fragility, and implementations. *Rev. Mod. Phys.*, 90:025004, May 2018.
 - [56] Mamiko Tatsuta, Yuichiro Matsuzaki, and Akira Shimizu. Quantum metrology with generalized cat states. *Phys. Rev. A*, 100:032318, Sep 2019.
 - [57] Chae-Yeun Park and Hyunseok Jeong. Disappearance of macroscopic superpositions in perfectly isolated systems by thermalization processes. *arXiv preprint arXiv:1606.07213*, 2016.
 - [58] Hengyun Zhou, Joonhee Choi, Soonwon Choi, Renate Landig, Alexander M. Douglas, Junichi Isoya, Fedor Jelezko, Shinobu Onoda, Hitoshi Sumiya, Paola Cappellaro, Helena S. Knowles, Hongkun Park, and Mikhail D. Lukin. Quantum metrology with strongly interacting spin systems. *Phys. Rev. X*, 10:031003, Jul 2020.
 - [59] Elliott Lieb, Theodore Schultz, and Daniel Mattis. Two soluble models of an antiferromagnetic chain. *Ann. Phys.*, 16(3):407–466, 1961.
 - [60] Shigetoshi Katsura. Statistical mechanics of the anisotropic linear heisenberg model. *Phys. Rev.*, 127(5):1508, 1962.
 - [61] Pierre Pfeuty. The one-dimensional ising model with a transverse field. *Ann. Phys.*, 57(1):79–90, 1970.
 - [62] Subir Sachdev. *Quantum phase transitions*. Cambridge university press, 2011.
 - [63] Lars Onsager. Crystal statistics. i. a two-dimensional model with an order-disorder transition. *Phys. Rev.*, 65(3-4):117, 1944.
 - [64] PG De Gennes. Collective motions of hydrogen bonds. *Solid State Commun.*, 1(6):132–137, 1963.
 - [65] RB Stinchcombe. Ising model in a transverse field. i. basic theory. *J. Phys. C*, 6(15):2459, 1973.
 - [66] Amit Dutta, Gabriel Aeppli, Bikas K Chakrabarti, Uma Divakaran, Thomas F Rosenbaum, and Diptiman Sen. *Quantum phase transitions in transverse field spin models: from statistical physics to quantum information*. Cambridge University Press, 2015.
 - [67] Antoine Browaeys and Thierry Lahaye. Many-body physics with individually controlled rydberg atoms. *Nat. Phys.*, 16(2):132–142, 2020.
 - [68] Justin G. Bohnet, Brian C. Sawyer, Joseph W. Britton, Michael L. Wall, Ana Maria Rey, Michael Foss-Feig, and John J. Bollinger. Quantum spin dynamics and entanglement generation with hundreds of trapped ions. *Science*, 352(6291):1297–1301, 2016.

- [69] R. Harris, Y. Sato, A. J. Berkley, M. Reis, F. Altomare, M. H. Amin, K. Boothby, P. Bunyk, C. Deng, C. Enderud, S. Huang, E. Hoskinson, M. W. Johnson, E. Ladizinsky, N. Ladizinsky, T. Lanting, R. Li, T. Medina, R. Molavi, R. Neufeld, T. Oh, I. Pavlov, I. Perminov, G. Poulin-Lamarre, C. Rich, A. Smirnov, L. Swenson, N. Tsai, M. Volkman, J. Whittaker, and J. Yao. Phase transitions in a programmable quantum spin glass simulator. *Science*, 361(6398):162–165, 2018.
- [70] Tadashi Kadowaki and Hidetoshi Nishimori. Quantum annealing in the transverse ising model. *Phys. Rev. E*, 58(5):5355, 1998.
- [71] J Brooke, David Bitko, Rosenbaum, and Gabriel Aeppli. Quantum annealing of a disordered magnet. *Science*, 284(5415):779–781, 1999.
- [72] Arnab Das and Bikas K Chakrabarti. Colloquium: Quantum annealing and analog quantum computation. *Rev. Mod. Phys.*, 80(3):1061, 2008.
- [73] M. W. Johnson, M. H. S. Amin, S. Gildert, T. Lanting, F. Hamze, N. Dickson, R. Harris, A. J. Berkley, J. Johansson, P. Bunyk, E. M. Chapple, C. Enderud, J. P. Hilton, K. Karimi, E. Ladizinsky, N. Ladizinsky, T. Oh, I. Perminov, C. Rich, M. C. Thom, E. Tolkacheva, C. J. S. Truncik, S. Uchaikin, J. Wang, B. Wilson, and G. Rose. Quantum annealing with manufactured spins. *Nature*, 473(7346):194–198, 2011.
- [74] Atsuki Yoshinaga, Hideaki Hakoshima, Takashi Imoto, Yuichiro Matsuzaki, and Ryusuke Hamazaki. Emergence of hilbert space fragmentation in ising models with a weak transverse field. *Phys. Rev. Lett.*, 129:090602, Aug 2022.
- [75] Atsuki Yoshinaga, Yuichiro Matsuzaki, and Ryusuke Hamazaki. Quantum metrology protected by hilbert space fragmentation. *arXiv preprint arXiv:2211.09567*, 2022.
- [76] Atsuki Yoshinaga, Mamiko Tatsuta, and Yuichiro Matsuzaki. Entanglement-enhanced sensing using a chain of qubits with always-on nearest-neighbor interactions. *Phys. Rev. A*, 103:062602, Jun 2021.
- [77] Takashi Mori, Tatsuhiko N Ikeda, Eriko Kaminishi, and Masahito Ueda. Thermalization and prethermalization in isolated quantum systems: a theoretical overview. *J. Phys. B*, 51(11):112001, may 2018.
- [78] Adam M Kaufman, M Eric Tai, Alexander Lukin, Matthew Rispoli, Robert Schittko, Philipp M Preiss, and Markus Greiner. Quantum thermalization through entanglement in an isolated many-body system. *Science*, 353(6301):794–800, 2016.
- [79] Peter Reimann. Foundation of statistical mechanics under experimentally realistic conditions. *Phys. Rev. Lett.*, 101(19):190403, 2008.
- [80] Noah Linden, Sandu Popescu, Anthony J. Short, and Andreas Winter. Quantum mechanical evolution towards thermal equilibrium. *Phys. Rev. E*, 79:061103, Jun 2009.
- [81] Anthony J Short. Equilibration of quantum systems and subsystems. *New J. Phys.*, 13(5):053009, may 2011.
- [82] Anthony J Short and Terence C Farrelly. Quantum equilibration in finite time. *New J. Phys.*, 14(1):013063, jan 2012.
- [83] Peter Reimann and Michael Kastner. Equilibration of isolated macroscopic quantum systems. *New J. Phys.*, 14(4):043020, apr 2012.
- [84] H. Wilming, M. Goihl, I. Roth, and J. Eisert. Entanglement-ergodic quantum systems equilibrate exponentially well. *Phys. Rev. Lett.*, 123:200604, Nov 2019.
- [85] Terry Farrelly, Fernando G. S. L. Brandão, and Marcus Cramer. Thermalization and return to equilibrium on finite quantum lattice systems. *Phys. Rev. Lett.*, 118:140601, Apr

2017.

- [86] M. Gring, M. Kuhnert, T. Langen, T. Kitagawa, B. Rauer, M. Schreitl, I. Mazets, D. Adu Smith, E. Demler, and J. Schmiedmayer. Relaxation and prethermalization in an isolated quantum system. *Science*, 337(6100):1318–1322, 2012.
- [87] Tim Langen, Sebastian Erne, Remi Geiger, Bernhard Rauer, Thomas Schweigler, Maximilian Kuhnert, Wolfgang Rohringer, Igor E. Mazets, Thomas Gasenzer, and Jörg Schmiedmayer. Experimental observation of a generalized gibbs ensemble. *Science*, 348(6231):207–211, 2015.
- [88] J v Neumann. Beweis des ergodensatzes und desh-theorems in der neuen mechanik. *Zeitschrift für Physik*, 57(1):30–70, 1929.
- [89] John von Neumann. Proof of the ergodic theorem and the h-theorem in quantum mechanics. *Eur. Phys. J. H*, 35(2):201–237, 2010.
- [90] R. V. Jensen and R. Shankar. Statistical behavior in deterministic quantum systems with few degrees of freedom. *Phys. Rev. Lett.*, 54(17):1879, 1985.
- [91] Asher Peres. Ergodicity and mixing in quantum theory. i. *Phys. Rev. A*, 30:504–508, Jul 1984.
- [92] Hal Tasaki. From quantum dynamics to the canonical distribution: general picture and a rigorous example. *Phys. Rev. Lett.*, 80(7):1373, 1998.
- [93] Marcos Rigol, Vanja Dunjko, Vladimir Yurovsky, and Maxim Olshanii. Relaxation in a completely integrable many-body quantum system: an ab initio study of the dynamics of the highly excited states of 1d lattice hard-core bosons. *Phys. Rev. Lett.*, 98(5):050405, 2007.
- [94] Toshiya Kinoshita, Trevor Wenger, and David S Weiss. A quantum newton’s cradle. *Nature*, 440(7086):900–903, 2006.
- [95] Jean-Sébastien Caux and Jorn Mossel. Remarks on the notion of quantum integrability. *J. Stat. Mech.*, 2011(02):P02023, feb 2011.
- [96] Pasquale Calabrese, Fabian H L Essler, and Giuseppe Mussardo. Introduction to ‘quantum integrability in out of equilibrium systems’. *J. Stat. Mech.*, 2016(6):064001, jun 2016.
- [97] Christian Gogolin and Jens Eisert. Equilibration, thermalisation, and the emergence of statistical mechanics in closed quantum systems. *Rep. Prog. Phys.*, 79(5):056001, 2016.
- [98] Madan Lal Mehta. *Random matrices*. Elsevier, 2004.
- [99] Y. Y. Atas, E. Bogomolny, O. Giraud, and G. Roux. Distribution of the ratio of consecutive level spacings in random matrix ensembles. *Phys. Rev. Lett.*, 110(8):084101, 2013.
- [100] Rubem Mondaini, Keith R Fratus, Mark Srednicki, and Marcos Rigol. Eigenstate thermalization in the two-dimensional transverse field ising model. *Phys. Rev. E*, 93(3):032104, 2016.
- [101] Aviva Gubin and Lea F. Santos. Quantum chaos: An introduction via chains of interacting spins 1/2. *Am. J. Phys.*, 80(3):246–251, 2012.
- [102] Ryusuke Hamazaki, Tatsuhiko N Ikeda, and Masahito Ueda. Generalized gibbs ensemble in a nonintegrable system with an extensive number of local symmetries. *Phys. Rev. E*, 93(3):032116, 2016.
- [103] D. Poilblanc, T. Ziman, J. Bellissard, F. Mila, and G. Montambaux. Poisson vs. goe statistics in integrable and non-integrable quantum hamiltonians. *Europhys. Lett.*, 22(7):537,

- jun 1993.
- [104] Lea F. Santos and Marcos Rigol. Onset of quantum chaos in one-dimensional bosonic and fermionic systems and its relation to thermalization. *Phys. Rev. E*, 81:036206, Mar 2010.
 - [105] Rubem Mondaini, Krishnanand Mallayya, Lea F Santos, and Marcos Rigol. Comment on “systematic construction of counterexamples to the eigenstate thermalization hypothesis”. *Phys. Rev. Lett.*, 121(3):038901, 2018.
 - [106] Naoto Shiraishi and Takashi Mori. Shiraishi and mori reply. *Phys. Rev. Lett.*, 121:038902, Jul 2018.
 - [107] Giuseppe De Tomasi, Daniel Hetterich, Pablo Sala, and Frank Pollmann. Dynamics of strongly interacting systems: From fock-space fragmentation to many-body localization. *Phys. Rev. B*, 100(21):214313, 2019.
 - [108] Zhi-Cheng Yang, Fangli Liu, Alexey V Gorshkov, and Thomas Iadecola. Hilbert-space fragmentation from strict confinement. *Phys. Rev. Lett.*, 124(20):207602, 2020.
 - [109] Tibor Rakovszky, Pablo Sala, Ruben Verresen, Michael Knap, and Frank Pollmann. Statistical localization: From strong fragmentation to strong edge modes. *Phys. Rev. B*, 101(12):125126, 2020.
 - [110] Hongzheng Zhao, Joseph Vovrosh, Florian Mintert, and Johannes Knolle. Quantum many-body scars in optical lattices. *Phys. Rev. Lett.*, 124(16):160604, 2020.
 - [111] Kyungmin Lee, Arijeet Pal, and Hitesh J Changlani. Frustration-induced emergent hilbert space fragmentation. *Phys. Rev. B*, 103(23):235133, 2021.
 - [112] Alexey Khudorozhkov, Apoorv Tiwari, Claudio Chamon, and Titus Neupert. Hilbert space fragmentation in a 2d quantum spin system with subsystem symmetries. *arXiv preprint arXiv:2107.09690*, 2021.
 - [113] Bhaskar Mukherjee, Debasish Banerjee, K Sengupta, and Arnab Sen. Minimal model for hilbert space fragmentation with local constraints. *Phys. Rev. B*, 104(15):155117, 2021.
 - [114] Berislav Buča. Out-of-time-ordered crystals and fragmentation. *Phys. Rev. Lett.*, 128:100601, Mar 2022.
 - [115] Alvis Bastianello, Umberto Borla, and Sergej Moroz. Fragmentation and emergent integrable transport in the weakly tilted ising chain. *Phys. Rev. Lett.*, 128:196601, May 2022.
 - [116] Sanjay Moudgalya and Olexei I. Motrunich. Hilbert space fragmentation and commutant algebras. *Phys. Rev. X*, 12:011050, Mar 2022.
 - [117] Sanjay Moudgalya, B. Andrei Bernevig, and Nicolas Regnault. Quantum many-body scars in a landau level on a thin torus. *Phys. Rev. B*, 102:195150, Nov 2020.
 - [118] Sebastian Scherg, Thomas Kohlert, Pablo Sala, Frank Pollmann, Bharath Hebbe Madhusudhana, Immanuel Bloch, and Monika Aidelsburger. Observing non-ergodicity due to kinetic constraints in tilted fermi-hubbard chains. *Nat. Commun.*, 12(1):4490, 2021.
 - [119] Thomas Kohlert, Sebastian Scherg, Pablo Sala, Frank Pollmann, Bharath Hebbe Madhusudhana, Immanuel Bloch, and Monika Aidelsburger. Experimental realization of fragmented models in tilted fermi-hubbard chains. *arXiv preprint arXiv:2106.15586*, 2021.
 - [120] Brendon L Higgins, Dominic W Berry, Stephen D Bartlett, Howard M Wiseman, and Geoff J Pryde. Entanglement-free heisenberg-limited phase estimation. *Nature*, 450(7168):393–396, 2007.
 - [121] D. W. Berry, B. L. Higgins, S. D. Bartlett, M. W. Mitchell, G. J. Pryde, and H. M. Wise-

- man. How to perform the most accurate possible phase measurements. *Phys. Rev. A*, 80:052114, Nov 2009.
- [122] R. S. Said, D. W. Berry, and J. Twamley. Nanoscale magnetometry using a single-spin system in diamond. *Phys. Rev. B*, 83:125410, Mar 2011.
- [123] N. M. Nusran and M. V. Gurudev Dutt. Optimizing phase-estimation algorithms for diamond spin magnetometry. *Phys. Rev. B*, 90:024422, Jul 2014.
- [124] W. M. Itano, J. C. Bergquist, J. J. Bollinger, J. M. Gilligan, D. J. Heinzen, F. L. Moore, M. G. Raizen, and D. J. Wineland. Quantum projection noise: Population fluctuations in two-level systems. *Phys. Rev. A*, 47:3554–3570, May 1993.
- [125] Daniel M Greenberger, Michael A Horne, Abner Shimony, and Anton Zeilinger. Bell’s theorem without inequalities. *Am. J. Phys.*, 58(12):1131–1143, 1990.
- [126] Thomas Monz, Philipp Schindler, Julio T. Barreiro, Michael Chwalla, Daniel Nigg, William A. Coish, Maximilian Harlander, Wolfgang Hänsel, Markus Hennrich, and Rainer Blatt. 14-qubit entanglement: Creation and coherence. *Phys. Rev. Lett.*, 106:130506, Mar 2011.
- [127] Chao Song, Kai Xu, Hekang Li, Yu-Ran Zhang, Xu Zhang, Wuxin Liu, Qiujiang Guo, Zhen Wang, Wenhui Ren, Jie Hao, et al. Generation of multicomponent atomic schrödinger cat states of up to 20 qubits. *Science*, 365(6453):574–577, 2019.
- [128] Rami Barends, Julian Kelly, Anthony Megrant, Andrzej Veitia, Daniel Sank, Evan Jeffrey, Ted C White, Josh Mutus, Austin G Fowler, Brooks Campbell, et al. Superconducting quantum circuits at the surface code threshold for fault tolerance. *Nature*, 508(7497):500–503, 2014.
- [129] Ken X. Wei, Isaac Lauer, Srikanth Srinivasan, Neereja Sundaresan, Douglas T. McClure, David Toyli, David C. McKay, Jay M. Gambetta, and Sarah Sheldon. Verifying multipartite entangled greenberger-horne-zeilinger states via multiple quantum coherences. *Phys. Rev. A*, 101:032343, Mar 2020.
- [130] Soonwon Choi, Norman Y Yao, and Mikhail D Lukin. Quantum metrology based on strongly correlated matter. *arXiv:1801.00042*, 2017.
- [131] Jiahao Huang, Min Zhuang, and Chaohong Lee. Non-gaussian precision metrology via driving through quantum phase transitions. *Phys. Rev. A*, 97(3):032116, 2018.
- [132] Takuya Hatomura, Atsuki Yoshinaga, Yuichiro Matsuzaki, and Mamiko Tatsuta. Quantum metrology based on symmetry-protected adiabatic transformation: imperfection, finite time duration, and dephasing. *New J. Phys.*, 24(3):033005, 2022.
- [133] Jan Jeske, Jared H Cole, and Susana F Huelga. Quantum metrology subject to spatially correlated markovian noise: restoring the heisenberg limit. *New J. Phys.*, 16(7):073039, jul 2014.
- [134] Katarzyna Macieszczak. Zeno limit in frequency estimation with non-markovian environments. *Phys. Rev. A*, 92:010102, Jul 2015.
- [135] Xinyue Long, Wan-Ting He, Na-Na Zhang, Kai Tang, Zidong Lin, Hongfeng Liu, Xinfang Nie, Guanru Feng, Jun Li, Tao Xin, Qing Ai, and Dawei Lu. Entanglement-enhanced quantum metrology in colored noise by quantum zeno effect. *Phys. Rev. Lett.*, 129:070502, Aug 2022.
- [136] P. Jordan and E. Wigner. Über das paulische äquivalenzverbot. *Zeitschrift für Physik*, 47(9):631–651, 1928.
- [137] Jae-Seung Lee and A. K. Khitrin. Stimulated wave of polarization in a one-dimensional

- ising chain. *Phys. Rev. A*, 71:062338, Jun 2005.
- [138] G. B. Furman, S. D. Goren, J.-S. Lee, A. K. Khitrin, V. M. Meerovich, and V. L. Sokolovsky. Stimulated wave of polarization in spin chains. *Phys. Rev. B*, 74:054404, Aug 2006.
- [139] Vinita Balachandran and Jiangbin Gong. Controlled measurement processes: Simple spin-chain model of controlled quantum-state amplification. *Phys. Rev. A*, 79:012317, Jan 2009.
- [140] Tom Close, Femi Fadugba, Simon C. Benjamin, Joseph Fitzsimons, and Brendon W. Lovett. Rapid and robust spin state amplification. *Phys. Rev. Lett.*, 106:167204, Apr 2011.
- [141] Jae-Seung Lee, Travis Adams, and A K Khitrin. Experimental demonstration of a stimulated polarization wave in a chain of nuclear spins. *New J. Phys.*, 9(4):83–83, apr 2007.
- [142] Maike Ostmann, Matteo Marcuzzi, Juan P Garrahan, and Igor Lesanovsky. Localization in spin chains with facilitation constraints and disordered interactions. *Phys. Rev. A*, 99(6):060101, 2019.
- [143] Keith R Fratus and Mark Srednicki. Eigenstate thermalization in systems with spontaneously broken symmetry. *Phys. Rev. E*, 92(4):040103, 2015.
- [144] Benjamin Blaß and Heiko Rieger. Test of quantum thermalization in the two-dimensional transverse-field ising model. *Sci. Rep.*, 6(1):1–17, 2016.
- [145] Bart van Voorden, Jiří Minář, and Kareljan Schoutens. Quantum many-body scars in transverse field ising ladders and beyond. *Phys. Rev. B*, 101(22):220305, 2020.
- [146] Elmer Guardado-Sanchez, Peter T Brown, Debayan Mitra, Trithep Devakul, David A Huse, Peter Schauß, and Waseem S Bakr. Probing the quench dynamics of antiferromagnetic correlations in a 2d quantum ising spin system. *Phys. Rev. X*, 8(2):021069, 2018.
- [147] Markus Schmitt and Markus Heyl. Quantum many-body dynamics in two dimensions with artificial neural networks. *Phys. Rev. Lett.*, 125(10):100503, 2020.
- [148] Jonas Richter, Tjark Heitmann, and Robin Steinigeweg. Quantum quench dynamics in the transverse-field ising model: A numerical expansion in linked rectangular clusters. *SciPost Phys.*, 9(3):031, 2020.
- [149] Michael Schreiber, Sean S Hodgman, Pranjal Bordia, Henrik P Lüschen, Mark H Fischer, Ronen Vosk, Ehud Altman, Ulrich Schneider, and Immanuel Bloch. Observation of many-body localization of interacting fermions in a quasirandom optical lattice. *Science*, 349(6250):842–845, 2015.
- [150] Jacob Smith, Aaron Lee, Philip Richerme, Brian Neyenhuis, Paul W Hess, Philipp Hauke, Markus Heyl, David A Huse, and Christopher Monroe. Many-body localization in a quantum simulator with programmable random disorder. *Nat. Phys.*, 12(10):907–911, 2016.
- [151] Henning Labuhn, Daniel Barredo, Sylvain Ravets, Sylvain De Léséleuc, Tommaso Macrì, Thierry Lahaye, and Antoine Browaeys. Tunable two-dimensional arrays of single rydberg atoms for realizing quantum ising models. *Nature*, 534(7609):667–670, 2016.
- [152] G. Kucsko, S. Choi, J. Choi, P. C. Maurer, H. Zhou, R. Landig, H. Sumiya, S. Onoda, J. Isoya, F. Jelezko, E. Demler, N. Y. Yao, and M. D. Lukin. Critical thermalization of a disordered dipolar spin system in diamond. *Phys. Rev. Lett.*, 121(2):023601, 2018.
- [153] Robin Steinigeweg, Jacek Herbrych, and Peter Prelovšek. Eigenstate thermalization within isolated spin-chain systems. *Phys. Rev. E*, 87(1):012118, 2013.

- [154] Lev Vidmar and Marcos Rigol. Generalized gibbs ensemble in integrable lattice models. *J. Stat. Mech.*, 2016(6):064007, 2016.
- [155] Arijeet Pal and David A Huse. Many-body localization phase transition. *Phys. Rev. B*, 82(17):174411, 2010.
- [156] Maksym Serbyn, Zlatko Papić, and Dmitry A Abanin. Local conservation laws and the structure of the many-body localized states. *Phys. Rev. Lett.*, 111(12):127201, 2013.
- [157] David A Huse, Rahul Nandkishore, and Vadim Oganesyan. Phenomenology of fully many-body-localized systems. *Phys. Rev. B*, 90(17):174202, 2014.
- [158] Dmitry Abanin, Wojciech De Roeck, Wen Wei Ho, and François Huveneers. A rigorous theory of many-body prethermalization for periodically driven and closed quantum systems. *Commun. Math. Phys.*, 354(3):809–827, 2017.
- [159] Tom Close, Femi Fadugba, Simon C Benjamin, Joseph Fitzsimons, and Brendon W Lovett. Rapid and robust spin state amplification. *Phys. Rev. Lett.*, 106(16):167204, 2011.
- [160] Zongping Gong, Nobuyuki Yoshioka, Naoyuki Shibata, and Ryusuke Hamazaki. Error bounds for constrained dynamics in gapped quantum systems: Rigorous results and generalizations. *Phys. Rev. A*, 101(5):052122, 2020.
- [161] Zongping Gong, Nobuyuki Yoshioka, Naoyuki Shibata, and Ryusuke Hamazaki. Universal error bound for constrained quantum dynamics. *Phys. Rev. Lett.*, 124(21):210606, 2020.
- [162] J. R. Schrieffer and P. A. Wolff. Relation between the anderson and kondo hamiltonians. *Phys. Rev.*, 149:491–492, Sep 1966.
- [163] Sergey Bravyi, David P DiVincenzo, and Daniel Loss. Schrieffer–wolff transformation for quantum many-body systems. *Ann. Phys.*, 326(10):2793–2826, 2011.
- [164] Alexios A. Michailidis, Marko Žnidarič, Mariya Medvedyeva, Dmitry A. Abanin, Tomaž Prosen, and Z. Papić. Slow dynamics in translation-invariant quantum lattice models. *Phys. Rev. B*, 97:104307, Mar 2018.
- [165] Oliver Hart and Rahul Nandkishore. Hilbert space shattering and dynamical freezing in the quantum ising model. *Phys. Rev. B*, 106:214426, Dec 2022.
- [166] Federico Balducci, Andrea Gambassi, Alessio Lerose, Antonello Scardicchio, and Carlo Vanoni. Localization and melting of interfaces in the two-dimensional quantum ising model. *Phys. Rev. Lett.*, 129:120601, Sep 2022.
- [167] Alan Morningstar, Vedika Khemani, and David A Huse. Kinetically constrained freezing transition in a dipole-conserving system. *Phys. Rev. B*, 101(21):214205, 2020.
- [168] Jean-Yves Desaulles, Ana Hudomal, Christopher J Turner, and Zlatko Papić. Proposal for realizing quantum scars in the tilted 1d fermi-hubbard model. *Phys. Rev. Lett.*, 126(21):210601, 2021.
- [169] Federica Maria Surace, Marcello Dalmonte, and Alessandro Silva. Quantum local random networks and the statistical robustness of quantum scars. *arXiv:2107.00884*, 2021.
- [170] C. J. Turner, A. A. Michailidis, D. A. Abanin, M. Serbyn, and Z. Papić. Quantum scarred eigenstates in a rydberg atom chain: Entanglement, breakdown of thermalization, and stability to perturbations. *Phys. Rev. B*, 98(15):155134, 2018.
- [171] Cheng-Ju Lin and Olexei I Motrunich. Exact quantum many-body scar states in the rydberg-blockaded atom chain. *Phys. Rev. Lett.*, 122(17):173401, 2019.
- [172] Thomas Iadecola, Michael Schecter, and Shenglong Xu. Quantum many-body scars from

- magnon condensation. *Phys. Rev. B*, 100(18):184312, 2019.
- [173] Jae-Seung Lee and A. K. Khitrin. Stimulated wave of polarization in a one-dimensional ising chain. *Phys. Rev. A*, 71(6):062338, 2005.
- [174] Aishwarya Kumar, Tsung-Yao Wu, Felipe Giraldo, and David S Weiss. Sorting ultracold atoms in a three-dimensional optical lattice in a realization of maxwell’s demon. *Nature*, 561(7721):83–87, 2018.
- [175] Yunheung Song, Minhyuk Kim, Hansub Hwang, Woojun Lee, and Jaewook Ahn. Quantum simulation of cayley-tree ising hamiltonians with three-dimensional rydberg atoms. *Phys. Rev. Research*, 3(1):013286, 2021.
- [176] Sepehr Ebadi, Tout T. Wang, Harry Levine, Alexander Keesling, Giulia Semeghini, Ahmed Omran, Dolev Bluvstein, Rhine Samajdar, Hannes Pichler, Wen Wei Ho, Soonwon Choi, Subir Sachdev, Markus Greiner, Vladan Vuletić, and Mikhail D. Lukin. Quantum phases of matter on a 256-atom programmable quantum simulator. *Nature*, 595(7866):227–232, 2021.
- [177] Pascal Scholl, Michael Schuler, Hannah J. Williams, Alexander A. Eberharter, Daniel Barredo, Kai-Niklas Schymik, Vincent Lienhard, Louis-Paul Henry, Thomas C. Lang, Thierry Lahaye, Andreas M. Läuchli, and Antoine Browaeys. Quantum simulation of 2d antiferromagnets with hundreds of rydberg atoms. *Nature*, 595(7866):233–238, 2021.
- [178] Andrey Gromov, Andrew Lucas, and Rahul M Nandkishore. Fracton hydrodynamics. *Phys. Rev. Research*, 2(3):033124, 2020.
- [179] Jason Iaconis, Sagar Vijay, and Rahul Nandkishore. Anomalous subdiffusion from subsystem symmetries. *Phys. Rev. B*, 100:214301, Dec 2019.
- [180] Federico Balducci, Andrea Gambassi, Alessio Lerose, Antonello Scardicchio, and Carlo Vanoni. Interface dynamics in the two-dimensional quantum ising model. *arXiv preprint arXiv:2209.08992*, 2022.
- [181] Shane Dooley. Robust quantum sensing in strongly interacting systems with many-body scars. *PRX Quantum*, 2:020330, May 2021.
- [182] Michael Schecter and Thomas Iadecola. Many-body spectral reflection symmetry and protected infinite-temperature degeneracy. *Phys. Rev. B*, 98(3):035139, 2018.
- [183] Scott Kirkpatrick and Thomas P Eggarter. Localized states of a binary alloy. *Phys. Rev. B*, 6(10):3598, 1972.
- [184] Bill Sutherland. Localization of electronic wave functions due to local topology. *Phys. Rev. B*, 34(8):5208, 1986.
- [185] Ruben Bueno and Naomichi Hatano. Null-eigenvalue localization of quantum walks on complex networks. *Phys. Rev. Research*, 2(3):033185, 2020.
- [186] Cheng-Ju Lin, Vladimir Calvera, and Timothy H Hsieh. Quantum many-body scar states in two-dimensional rydberg atom arrays. *Phys. Rev. B*, 101(22):220304, 2020.
- [187] Hongzheng Zhao, Adam Smith, Florian Mintert, and Johannes Knolle. Orthogonal quantum many-body scars. *Phys. Rev. Lett.*, 127(15):150601, 2021.
- [188] Vittorio Giovannetti, Seth Lloyd, and Lorenzo Maccone. Quantum-enhanced measurements: Beating the standard quantum limit. *Science*, 306(5700):1330–1336, 2004.
- [189] Géza Tóth and Iagoba Apellaniz. Quantum metrology from a quantum information science perspective. *J. Phys. A*, 47(42):424006, oct 2014.
- [190] Bernard Yurke, Samuel L. McCall, and John R. Klauder. $Su(2)$ and $su(1,1)$ interferometers. *Phys. Rev. A*, 33:4033–4054, Jun 1986.

- [191] D. J. Wineland, J. J. Bollinger, W. M. Itano, F. L. Moore, and D. J. Heinzen. Spin squeezing and reduced quantum noise in spectroscopy. *Phys. Rev. A*, 46:R6797–R6800, Dec 1992.
- [192] D. J. Wineland, J. J. Bollinger, W. M. Itano, and D. J. Heinzen. Squeezed atomic states and projection noise in spectroscopy. *Phys. Rev. A*, 50:67–88, Jul 1994.
- [193] Hwang Lee, Pieter Kok, and Jonathan P. Dowling. A quantum rosetta stone for interferometry. *J. Mod. Opt.*, 49(14-15):2325–2338, 2002.
- [194] Vittorio Giovannetti, Seth Lloyd, and Lorenzo Maccone. Quantum metrology. *Phys. Rev. Lett.*, 96:010401, Jan 2006.
- [195] Jonathan A. Jones, Steven D. Karlen, Joseph Fitzsimons, Arzhang Ardavan, Simon C. Benjamin, G. Andrew D. Briggs, and John J. L. Morton. Magnetic field sensing beyond the standard quantum limit using 10-spin noon states. *Science*, 324(5931):1166–1168, 2009.
- [196] B. Lücke, M. Scherer, J. Kruse, L. Pezzé, F. Deuretzbacher, P. Hyllus, O. Topic, J. Peise, W. Ertmer, J. Arlt, L. Santos, A. Smerzi, and C. Klempt. Twin matter waves for interferometry beyond the classical limit. *Science*, 334(6057):773–776, 2011.
- [197] W. Muessel, H. Strobel, D. Linnemann, D. B. Hume, and M. K. Oberthaler. Scalable spin squeezing for quantum-enhanced magnetometry with bose-einstein condensates. *Phys. Rev. Lett.*, 113:103004, Sep 2014.
- [198] Tohru Tanaka, Paul Knott, Yuichiro Matsuzaki, Shane Dooley, Hiroshi Yamaguchi, William J. Munro, and Shiro Saito. Proposed robust entanglement-based magnetic field sensor beyond the standard quantum limit. *Phys. Rev. Lett.*, 115:170801, Oct 2015.
- [199] Onur Hosten, Nils J Engelsen, Rajiv Krishnakumar, and Mark A Kasevich. Measurement noise 100 times lower than the quantum-projection limit using entangled atoms. *Nature*, 529(7587):505–508, 2016.
- [200] J. S. Waugh, L. M. Huber, and U. Haeberlen. Approach to high-resolution nmr in solids. *Phys. Rev. Lett.*, 20:180–182, Jan 1968.
- [201] U. Haeberlen and J. S. Waugh. Coherent averaging effects in magnetic resonance. *Phys. Rev.*, 175:453–467, Nov 1968.
- [202] Marcus Stollsteimer and Günter Mahler. Suppression of arbitrary internal coupling in a quantum register. *Phys. Rev. A*, 64:052301, Oct 2001.
- [203] Pawel Wocjan, Martin Rötteler, Dominik Janzing, and Thomas Beth. Simulating hamiltonians in quantum networks: Efficient schemes and complexity bounds. *Phys. Rev. A*, 65:042309, Mar 2002.
- [204] Jean-Yves Desaulles, Francesca Pietracaprina, Zlatko Papić, John Goold, and Silvia Pappalardi. Extensive multipartite entanglement from $su(2)$ quantum many-body scars. *Phys. Rev. Lett.*, 129:020601, Jul 2022.
- [205] Shane Dooley, Silvia Pappalardi, and John Goold. Entanglement enhanced metrology with quantum many-body scars. *arXiv:2207.13521*, 2022.
- [206] N. David Mermin. Extreme quantum entanglement in a superposition of macroscopically distinct states. *Phys. Rev. Lett.*, 65:1838–1840, Oct 1990.
- [207] Yuichiro Matsuzaki, Simon C. Benjamin, and Joseph Fitzsimons. Magnetic field sensing beyond the standard quantum limit under the effect of decoherence. *Phys. Rev. A*, 84:012103, Jul 2011.
- [208] Alex W. Chin, Susana F. Huelga, and Martin B. Plenio. Quantum metrology in non-

- markovian environments. *Phys. Rev. Lett.*, 109:233601, Dec 2012.
- [209] Zongping Gong and Ryusuke Hamazaki. Bounds in nonequilibrium quantum dynamics. *Int. J. Mod. Phys. B*, 0(0):2230007, 0.
- [210] Yuichiro Matsuzaki, Takashi Imoto, and Yuki Susa. Generation of multipartite entanglement between spin-1 particles with bifurcation-based quantum annealing. *arXiv:2202.07210*, 2022.
- [211] Takanori Sugiyama. Precision-guaranteed quantum metrology. *Phys. Rev. A*, 91:042126, Apr 2015.
- [212] Yuki Takeuchi, Yuichiro Matsuzaki, Koichiro Miyanishi, Takanori Sugiyama, and William J. Munro. Quantum remote sensing with asymmetric information gain. *Phys. Rev. A*, 99:022325, Feb 2019.
- [213] Rajendra Bhatia. *Matrix analysis*, volume 169. Springer Science & Business Media, 2013.
- [214] David Le Sage, Koji Arai, David R Glenn, Stephen J DeVience, Linh M Pham, Lilah Rahn-Lee, Mikhail D Lukin, Amir Yacoby, Arash Komeili, and Ronald L Walsworth. Optical magnetic imaging of living cells. *Nature*, 496(7446):486–489, 2013.
- [215] Takayuki Iwasaki, Wataru Naruki, Kosuke Tahara, Toshiharu Makino, Hiromitsu Kato, Masahiko Ogura, Daisuke Takeuchi, Satoshi Yamasaki, and Mutsuko Hatano. Direct nanoscale sensing of the internal electric field in operating semiconductor devices using single electron spins. *ACS nano*, 11(2):1238–1245, 2017.
- [216] Francesco Casola, Toeno van der Sar, and Amir Yacoby. Probing condensed matter physics with magnetometry based on nitrogen-vacancy centres in diamond. *Nature Reviews Materials*, 3(1):1–13, 2018.
- [217] Carlton M. Caves. Quantum-mechanical noise in an interferometer. *Phys. Rev. D*, 23:1693–1708, Apr 1981.
- [218] J. J. Bollinger, Wayne M. Itano, D. J. Wineland, and D. J. Heinzen. Optimal frequency measurements with maximally correlated states. *Phys. Rev. A*, 54:R4649–R4652, Dec 1996.
- [219] P Neumann, N Mizuochi, F Rempp, Philip Hemmer, H Watanabe, S Yamasaki, V Jacques, Torsten Gaebel, F Jelezko, and J Wrachtrup. Multipartite entanglement among single spins in diamond. *science*, 320(5881):1326–1329, 2008.
- [220] Leonardo DiCarlo, Matthew D Reed, Luyan Sun, Blake R Johnson, Jerry M Chow, Jay M Gambetta, Luigi Frunzio, Steven M Girvin, Michel H Devoret, and Robert J Schoelkopf. Preparation and measurement of three-qubit entanglement in a superconducting circuit. *Nature*, 467(7315):574–578, 2010.
- [221] Matthew Neeley, Radoslaw C Bialczak, M Lenander, Erik Lucero, Matteo Mariantoni, AD O’connell, D Sank, H Wang, M Weides, J Wenner, et al. Generation of three-qubit entangled states using superconducting phase qubits. *Nature*, 467(7315):570–573, 2010.
- [222] T. Shimo-Oka, H. Kato, S. Yamasaki, F. Jelezko, S. Miwa, Y. Suzuki, and N. Mizuochi. Control of coherence among the spins of a single electron and the three nearest neighbor ^{13}C nuclei of a nitrogen-vacancy center in diamond. *Appl. Phys. Lett.*, 106(15):153103, 2015.
- [223] Elliott Lieb, Theodore Schultz, and Daniel Mattis. Two soluble models of an antiferromagnetic chain. *Ann. Phys.*, 16(3):407 – 466, 1961.
- [224] Pierre Pfeuty. The one-dimensional ising model with a transverse field. *Ann. Phys.*,

57(1):79 – 90, 1970.

- [225] A Yu Kitaev. Unpaired majorana fermions in quantum wires. *Physics-Uspekhi*, 44(10S):131, 2001.
- [226] R. Amsüss, Ch. Koller, T. Nöbauer, S. Putz, S. Rotter, K. Sandner, S. Schneider, M. Schramböck, G. Steinhauser, H. Ritsch, J. Schmiedmayer, and J. Majer. Cavity qed with magnetically coupled collective spin states. *Phys. Rev. Lett.*, 107:060502, Aug 2011.
- [227] Jonas Bylander, Simon Gustavsson, Fei Yan, Fumiki Yoshihara, Khalil Harrabi, George Fitch, David G Cory, Yasunobu Nakamura, Jaw-Shen Tsai, and William D Oliver. Noise spectroscopy through dynamical decoupling with a superconducting flux qubit. *Nat. Phys.*, 7(7):565–570, 2011.
- [228] S. Probst, H. Rotzinger, S. Wünsch, P. Jung, M. Jerger, M. Siegel, A. V. Ustinov, and P. A. Bushev. Anisotropic rare-earth spin ensemble strongly coupled to a superconducting resonator. *Phys. Rev. Lett.*, 110:157001, Apr 2013.
- [229] Fei Yan, Simon Gustavsson, Archana Kamal, Jeffrey Birenbaum, Adam P Sears, David Hover, Ted J Gudmundsen, Danna Rosenberg, Gabriel Samach, Steven Weber, et al. The flux qubit revisited to enhance coherence and reproducibility. *Nat. Commun.*, 7(1):1–9, 2016.
- [230] Andreas Angerer, Stefan Putz, Dmitry O. Krimer, Thomas Astner, Matthias Zens, Ralph Glattauer, Kirill Streltsov, William J. Munro, Kae Nemoto, Stefan Rotter, Jörg Schmiedmayer, and Johannes Majer. Ultralong relaxation times in bistable hybrid quantum systems. *Science Advances*, 3(12), 2017.
- [231] Rangga P. Budoyo, Kosuke Kakuyanagi, Hiraku Toida, Yuichiro Matsuzaki, William J. Munro, Hiroshi Yamaguchi, and Shiro Saito. Phonon-bottlenecked spin relaxation of $\text{er}^{3+}:\text{y}2\text{sio}5$ at sub-kelvin temperatures. *Applied Physics Express*, 11(4):043002, mar 2018.
- [232] Leonid V Abdurakhimov, Imran Mahboob, Hiraku Toida, Kousuke Kakuyanagi, and Shiro Saito. A long-lived capacitively shunted flux qubit embedded in a 3d cavity. *Appl. Phys. Lett.*, 115(26):262601, 2019.
- [233] ED Herbschleb, H Kato, Y Maruyama, T Danjo, T Makino, S Yamasaki, I Ohki, K Hayashi, H Morishita, M Fujiwara, et al. Ultra-long coherence times amongst room-temperature solid-state spins. *Nat. Commun.*, 10(1):1–6, 2019.
- [234] Matthew D Reed, Blake R Johnson, Andrew A Houck, Leonardo DiCarlo, Jerry M Chow, David I Schuster, Luigi Frunzio, and Robert J Schoelkopf. Fast reset and suppressing spontaneous emission of a superconducting qubit. *Appl. Phys. Lett.*, 96(20):203110, 2010.
- [235] Audrey Bienfait, JJ Pla, Yuimaru Kubo, Xin Zhou, Michael Stern, CC Lo, CD Weis, Thomas Schenkel, Denis Vion, Daniel Esteve, et al. Controlling spin relaxation with a cavity. *Nature*, 531(7592):74–77, 2016.
- [236] P. Magnard, P. Kurpiers, B. Royer, T. Walter, J.-C. Besse, S. Gasparinetti, M. Pechal, J. Heinsoo, S. Storz, A. Blais, and A. Wallraff. Fast and unconditional all-microwave reset of a superconducting qubit. *Phys. Rev. Lett.*, 121:060502, Aug 2018.
- [237] Hao Hsu, Matti Silveri, András Gunyhó, Jan Goetz, Gianluigi Catelani, and Mikko Möttönen. Tunable refrigerator for nonlinear quantum electric circuits. *Phys. Rev. B*, 101:235422, Jun 2020.
- [238] A. De Pasquale, D. Rossini, P. Facchi, and V. Giovannetti. Quantum parameter estimation affected by unitary disturbance. *Phys. Rev. A*, 88:052117, Nov 2013.
- [239] Michael Skotiniotis, Pavel Sekatski, and Wolfgang Dür. Quantum metrology for the ising

- hamiltonian with transverse magnetic field. *New J. Phys.*, 17(7):073032, jul 2015.
- [240] Yuichiro Matsuzaki, Simon Benjamin, Shojun Nakayama, Shiro Saito, and William J. Munro. Quantum metrology beyond the classical limit under the effect of dephasing. *Phys. Rev. Lett.*, 120:140501, Apr 2018.
- [241] Agnieszka Górecka, Felix A Pollock, Pietro Liuzzo-Scorpo, Rosanna Nichols, Gerardo Adesso, and Kavan Modi. Noisy frequency estimation with noisy probes. *New J. Phys.*, 20(8):083008, aug 2018.
- [242] Le Bin Ho, Hideaki Hakoshima, Yuichiro Matsuzaki, Masayuki Matsuzaki, and Yasushi Kondo. Multiparameter quantum estimation under dephasing noise. *Phys. Rev. A*, 102:022602, Aug 2020.
- [243] F. Yoshihara, K. Harrabi, A. O. Niskanen, Y. Nakamura, and J. S. Tsai. Decoherence of flux qubits due to $1/f$ flux noise. *Phys. Rev. Lett.*, 97:167001, Oct 2006.
- [244] K. Kakuyanagi, T. Meno, S. Saito, H. Nakano, K. Semba, H. Takayanagi, F. Deppe, and A. Shnirman. Dephasing of a superconducting flux qubit. *Phys. Rev. Lett.*, 98:047004, Jan 2007.
- [245] Erika Kawakami, Pasquale Scarlino, Daniel R Ward, FR Braakman, DE Savage, MG Lagally, Mark Friesen, Susan N Coppersmith, Mark A Eriksson, and LMK Vandersypen. Electrical control of a long-lived spin qubit in a si/sige quantum dot. *Nature nanotechnology*, 9(9):666–670, 2014.
- [246] Erika Kawakami, Thibaut Jullien, Pasquale Scarlino, Daniel R Ward, Donald E Savage, Max G Lagally, Viatcheslav V Dobrovitski, Mark Friesen, Susan N Coppersmith, Mark A Eriksson, et al. Gate fidelity and coherence of an electron spin in an si/sige quantum dot with micromagnet. *Proceedings of the National Academy of Sciences*, 113(42):11738–11743, 2016.
- [247] J. R. Maze, J. M. Taylor, and M. D. Lukin. Electron spin decoherence of single nitrogen-vacancy defects in diamond. *Phys. Rev. B*, 78:094303, Sep 2008.
- [248] P. L. Stanwix, L. M. Pham, J. R. Maze, D. Le Sage, T. K. Yeung, P. Cappellaro, P. R. Hemmer, A. Yacoby, M. D. Lukin, and R. L. Walsworth. Coherence of nitrogen-vacancy electronic spin ensembles in diamond. *Phys. Rev. B*, 82:201201, Nov 2010.
- [249] E. Paladino, L. Faoro, G. Falci, and Rosario Fazio. Decoherence and $1/f$ noise in josephson qubits. *Phys. Rev. Lett.*, 88:228304, May 2002.
- [250] G De Lange, ZH Wang, D Riste, VV Dobrovitski, and R Hanson. Universal dynamical decoupling of a single solid-state spin from a spin bath. *Science*, 330(6000):60–63, 2010.
- [251] Y. Matsuzaki, S. Saito, K. Kakuyanagi, and K. Semba. Quantum zeno effect with a superconducting qubit. *Phys. Rev. B*, 82:180518, Nov 2010.
- [252] E. Paladino, Y. M. Galperin, G. Falci, and B. L. Altshuler. $1/f$ noise: Implications for solid-state quantum information. *Rev. Mod. Phys.*, 86:361–418, Apr 2014.
- [253] Shane Dooley, William J. Munro, and Kae Nemoto. Quantum metrology including state preparation and readout times. *Phys. Rev. A*, 94:052320, Nov 2016.
- [254] Junghyun Lee, Mamiko Tatsuta, Andrew Xu, Erik Bauch, Mark JH Ku, Ronald Walsworth, et al. Dressed-state control of effective dipolar interaction between strongly-coupled solid-state spins. *arXiv preprint arXiv:2203.07610*, 2022.